Ingar Stian Nerbø

Real-time Study of the Formation of GaSb Nanopillars by Spectroscopic Mueller Matrix Ellipsometry

Thesis for the degree of Philosophiae Doctor

Trondheim, August 2011

Norwegian University of Science and Technology
Faculty of Natural Sciences and Technology
Department of Physics

NTNU – Trondheim
Norwegian University of
Science and Technology

NTNU
Norwegian University of Science and Technology

Thesis for the degree of Philosophiae Doctor

Faculty of Natural Sciences and Technology
Department of Physics

ISBN 978-82-471-2970-8 (printed ver.)
ISBN 978-82-471-2972-2 (electronic ver.)
ISSN 1503-8181

Doctoral theses at NTNU, 2011:208

Printed by NTNU-trykk

Abstract

The formation of GaSb nanopillars have been studied in real-time by spectroscopic Mueller matrix ellipsometry. Low energy ion sputtering of GaSb leads to the formation of densely packed nanopillars on the surface. A graded anisotropic effective medium model was developed to characterize the structures from ellipsometry measurements; based on *ex situ* ellipsometry, atomic force microscopy, scanning electron microscopy and transmission electron microscopy. This model was applied to derive the height of the nanopillars from real-time ellipsometry measurements during sputtering. The real-time observations revealed an interesting and surprising evolution of the GaSb nanostructures. The formation could be divided into three regimes; first an initial stage with removal of oxide and some delay, followed by a second regime with a rapid and steady increase of the pillar height, and finally the formation changes to a third regime with a slow and linear increase of the pillar height. The dependence of the formation on experimental conditions, such as the temperature and the flux and energy of the ion beam, was studied. It was found that the ion flux determines the timescale of the formation, while the pillar height scale and late stage formation rate was controlled by the energy and the temperature.

The real-time observations of GaSb during sputtering provide new insight into why the GaSb nanopillars are formed. Traditionally the formation of patterns on GaSb during sputtering was explained by the Bradley–Harper model, where the structures are formed by a competition between curvature dependent sputtering yield and diffusion. However, this model can not explain the observation of the three different formation regimes. Instead, the real-time observations of the nanopillar formation supports the self sustained etch masking mechanism [S. Le Roy *et al. Journal of Applied Physics* **106** 094308 (2009)]. In this explanation, the pillars are formed due to segregation of Ga and the difference in sputtering yield between Ga and Sb.

GaSb nanopillars with a height of less than 100 nm were found to have uniaxial optical properties, with the optical axis parallel to the pillar axis. For larger structures, the uniaxial effective medium model was not able to represent the optical properties of the pillars. For sputtering with an ion energy of 500 eV, nanopillars with a height up to 300 nm can be formed. By real-time Mueller matrix measurements of the formation of such pillars, it was observed that the pillars had biaxially optical properties as the height surpassed 100 nm. Fourier analysis of a scanning electron microscope image of the final nanopillars showed that the lateral anisotropy can be attributed to a direction dependent nearest neighbor distance. Each individual pillar has uniaxial symmetry; the biaxial symmetry comes from the anisotropic organization of the pillars.

A commercial Mueller matrix ellipsometer was applied for the real-time mea-

surements, based on ferroelectric liquid crystals as polarization modulating elements. Improvements of such a system were proposed by optimizing the design with a genetic algorithm. The new design promise to reduce the measurement noise significantly compared to previous designs, in addition to extending the spectral range into the infrared.

Preface

This is a doctoral thesis submitted as part of the requirements for the degree of Philosophiae Doctor (Ph.D) at the Norwegian University of Science and Technology (NTNU). The work on this thesis started in the fall 2007 and was finished in the summer 2011 It was supervised by Professor Morten Kildemo at the department of physics. The main experimental work presented was performed during a six months long research stay at CNRS/Saint–Gobain in 2008, under the local supervision of Elin Søndergård.

I would like to thank my supervisor Morten Kildemo for giving me an excellent project, encouraging me to start a Ph.D, planning research, discussing results and help and comments on manuscript writing. I also would like to thank Mikael Lindgren and Ingve Simonsen for comments and discussions.

I am thankful to Elin Søndergård and Sebastien Le Roy at Saint–Gobain for a very fruitful collaboration, for preparing new and interesting samples and for inviting me to Paris. Your enthusiasm and interest made my stay rewarding, and kept my motivation up for the rest of my Ph.D.

I would like to thank my colleagues at the optics group; Lars Martin, Paul Anton, Jerome, Pål Gunnar, Daniel and Tor, for many interesting discussions, comments on manuscripts and the thesis, help in the lab, and for making the optics group an fun place to work. I also thank Magnus and Erlend at the electronics department.

I would like to thank Michel Stchakovsky, Denis Cattelan and other staff at *Horiba Jobin Yvon* for access to ellipsometric instruments and help and discussions on mounting the ellipsometer for *in situ* measurements. I am also grateful to Antonello De Martino and Martin Foldyna at Ecole Polytechnique, for performing angle resolved Mueller matrix measurement and for interesting discussions.

I would like to thank earlier Ph.D students Frantz Stabo-Eeg and Eirik Glimsdal for welcoming me to the group and for good discussions and advice on taking a Ph.D. I also thank earlier master student Susanne Hagen for her work on AFM and SEM imaging of GaSb nanopillars.

I would like to thank my girlfriend Guro for all understanding, countless discussions, for reading all my manuscripts and the thesis, and for all the good times.

I would like to acknowledge the travel grants received from the Aurora mobility program, and from Norges tekniske høgskoles fond.

List of papers

Paper I. "Characterisation of nanostructured GaSb : Comparison between large-area optical and local direct microscopic techniques" **Ingar Stian Nerbø**, Morten Kildemo, Sebastien Le Roy, Ingve Simonsen, Elin Søndergård, Livu Holt, and John C. Walmsley, *Applied Optics*, **47**, 5130 (2008)

Paper II. "Real-time in situ spectroscopic ellipsometry of GaSb nanostructures during sputtering" **Ingar Stian Nerbø**, Sebastien Le Roy, Morten Kildemo, and Elin Søndergård. *Applied Physics Letters*,**94**, 213105 (2009)

Paper III. "Characterization of inclined GaSb nanopillars by Mueller matrix ellipsometry" **Ingar Stian Nerbø**, Sebastien Le Roy, Martin Foldyna, Elin Søndergård, and Morten Kildemo. *Journal of Applied Physics*, **108**, 014307 (2010)

Paper IV. "In-situ and real time study of the formation of nanopatterns on GaSb by ion abrasion" Sebastien Le Roy, Elin Søndergård, **Ingar Stian Nerbø**, and Morten Kildemo, Submitted to *Physical Review B*

Paper V. "Real-time *in situ* Mueller matrix ellipsometry of GaSb nanopillars: Observation of anisotropic local alignment" **Ingar Stian Nerbø**, Sebastien Le Roy, Martin Foldyna, Elin Søndergård, and Morten Kildemo, *Optics Express*, **19**, 12511–12561 (2011)

Paper VI. "Fast and optimal broad-band Stokes/Mueller polarimeter design by the use of a genetic algorithm" Paul Anton Letnes, **Ingar Stian Nerbø**, Lars Martin Sandvik Aas, Pål Gunnar Ellingsen, and Morten Kildemo. *Optics Express*, **18**, 23095 (2010)

Related Papers

1. "Diffuse-interface model for nanopatterning induced by self-sustained ion-etch masking" Sebastien Le Roy, Elin Søndergård, **Ingar Stian Nerbø**, Morten Kildemo, and Mathis Plapp. *Physical Review B* ,**81**, 161401 (2010)

2. "Spectroscopic ellipsometry of nanostructured GaSb surfaces consisting of densely packed 80-230 nm long cones." Morten Kildemo, **Ingar Stian Nerbø**, Susanne Hagen, Sebastien Le Roy, and Elin Søndergård.*Materials Science & Engineering: B. Solid-state Materials for Advanced Technology* Volum 165.(3) s. 217-220 (2009)

3. "Optical response of nanostructured GaSb". Morten Kildemo, **Ingar Stian Nerbø**, Elin Søndergård, Livu Holt, Ingve Simonsen, and Michel Stchakovsky, *Physica Status Solidi. C, Current topics in solid state physics* Volum 5.(5) s. 1382-1385 (2008)

4. "Spectroscopic Ellipsometry for Real-time in situ Characterization of Nanostructures." **Ingar Stian Nerbø** *Nanocharm Newsletter*(3) s. 8-9 (2009)

5. "Well-conditioned multiple laser Mueller matrix ellipsometer." Frantz Stabo-Eeg Morten Kildemo, **Ingar Stian Nerbø**, and Mikeal Lindgren. *Optical Engineering: The Journal of SPIE* Volum 47.(7) s. 073604 (2008)

6. "Characterisation of liquid crystals for broadband optimal design of Mueller matrix ellipsometers", Jarle Ladstein, Morten Kildemo, Guro Kristin Svendsen, **Ingar Stian Nerbø**, and Frantz Stabo-Eeg. *Proceedings of SPIE - The International Society for Optical Engineering* 6587, art. no. 65870D (2007)

7. "Mueller matrix imaging of plasmonic polarizers on nanopatterned surface ", Lars Martin S. Aas, **Ingar Stian Nerbø**, Morten Kildemo, Daniele Chiappe, Christian Martella and Francesco Buatier de Mongeot. *SPIE - Optical Measurement Systems for Industrial Inspection VII* **8082**, art. no. 80822W. (2011)

8. "Genetic Invention of Fast and Optimal Broad-band Stokes/Mueller Polarimeter Designs", Paul Anton Letnes, **Ingar Stian Nerbø**, Lars Martin Sandvik Aas, Pål Gunnar Ellingsen, and Morten Kildemo. *Conference proceedings - Gecco 2011*

Contents

Chapter 1

Introduction

Nanoscience and nanotechnology have received a lot of attention over the recent years, promising to create materials with new properties. Examples of such new materials could be semiconductors with modified or intermediate bandgaps [1], which can have important technological applications in more efficient solar cells [2], light emitting diodes or sensors. Nanostructured surfaces can have applications as anti-reflective coatings [3, 4], optical filters, or for high density magnetic recording [5]. Good characterization tools for the nanoscale are necessary in order to understand the formation of such structures, and thereby be able to design nanostructures with desirable properties. Due to the diffraction limit of light, nanometer resolution can not be achieved with optical microscopes. Instead well established methods such as atomic force microscopy (AFM) and electron microscopy are used to characterize nanostructures. These methods are, however, relatively time-consuming and not well suited for *in situ* use or in-line production monitoring. To understand and control complex formation processes of nanostructures, real-time observations would be preferable. In this thesis I have applied ellipsometry to monitor the formation of nanostructures in real-time, and derive how the average height of the nanostructures evolve during formation.

Ellipsometry is an optical technique exploiting the vectorial nature of light, by measuring the change of polarization state of reflected light. As an optical method it is non-invasive and non-destructive, and it can easily access a process in a vacuum chamber through optical windows. It is a much used technique for accurately measuring the dielectric function of materials and the thickness of thin layers, see *e.g.* [6, 7], and plays an important role in the semiconductor industry. Ellipsometry has been widely applied for real-time monitoring of thin film growth (see *e.g.* [8, 9, 10]), allowing real-time measurements of changes in film thickness and composition. Ellipsometry is not only useful for measurements on materials with homogeneous plane parallel layers, it may also be highly sensitive to changes in heterogeneous or nanostructured materials, making it natural to extend the

use of ellipsometry also to real-time characterization of nanostructures. Several real-time studies have been performed on rough surfaces [11, 12, 13], providing information on the thickness of the rough layer. Other examples are real-time studies of the evolution of plasmon resonances of silver nanoparticles [14, 15, 16], and the evolution of the surface plasmon resonance of Ga nanoparticles [17].

The term nanostructure is used for objects that are larger than atoms, but smaller than microstructures, typically on the scale of 1 nm to 100 nm. Even though the term "nanoscience" is quite new, research on what is now called nanostructures has been performed for a long time, *e.g.* on metal nanoparticles in glass by Maxwell-Garnett in 1904. A large number of different names are used on what can be defined as nanostructured materials; such as inhomogeneous, granular, heterogeneous, ceramic, composite and porous materials, clusters, island films, discontinuous films, sculpted films, rough surfaces, and so on. Over the recent years there has been an accelerating interest in nanoscience [18] caused by improved technology for preparation and characterization of nanomaterials. A cost-efficient production is important in order for it to be viable to use such nanomaterials in technology. So called self-assembled nanostructures are promising in that sense, opening for low-cost production of nanostructures over large surface areas. Low energy ion sputtering is an example of such a process, where ripples, dots or pillars can be formed on the surface of various materials simply by exposure to a broad ion beam. In this case the structures are eroded into the material exposed to the ion beam, *i.e.* it is not deposition.

The discovery of the formation of nanodots during sputtering of compound semiconductors was first made by Facsko *et. al* in 1999 [19], who produced hexagonally ordered nanodots by normal incidence ion sputtering of gallium antimonide (GaSb). This process was proposed to be a low-cost, bottom-up approach to produce semiconductor quantum dots, and has since received much interest. Similar dot formation has also been observed on other compounds, such as InP [20], InSb, InAs [21] and GaAs [22]. Such patterns have been extensively studied *ex situ* by AFM, scanning electron microscopy (SEM) and transmission electron microscopy (TEM), to find the temporal evolution [23, 24], energy dependence [25, 22], and temperature dependence [21]. *In situ* grazing-incidence small-angle x-ray scattering (GISAXS) has been applied to study the time evolution of the lateral size and ordering of GaSb nanodots[26, 27], by sequential sputtering and measurements. However, no reports exist on real-time studies of such structures during sputtering.

The formation of dots during sputtering is in the above references explained on the basis of what is known as the Bradley–Harper model, where the structures are formed by a competition between curvature dependent sputtering yield and diffusion. However, for certain experimental conditions, sputtering of GaSb is

reported to lead to tall pillar-like structures with high aspect ratio, and sputtering with oblique ion incidence was found to give inclined nanopillars [28]. These observations can not be explained by a formation mechanism based on the Bradley–Harper model.

To obtain a deeper understanding on why these nanopillars are formed, real-time ellipsometry will in this thesis be used to study the formation of nanopillars during low energy ion sputtering of GaSb. Earlier *ex situ* studies of the temporal evolution of GaSb structures relied on very few observation points, due to the great time demand of producing a large sequence of samples with different exposure times. In addition the microscopy characterization techniques are time demanding in themselves. The production of a series of samples also introduces the possibility of uncertainties in the experimental conditions within the sample series, making temporal studies based on *ex situ* characterization challenging. *In situ* spectroscopic ellipsometry measurements can be performed every few seconds during the sputtering, without disturbing the process, allowing to observe the full dynamics of the nanostructures' formation process. By such dynamic studies, one may learn more about how and when the formation starts, at what rate structures form, and possible saturation and different regimes of the formation. One can study how the formation dynamics depend on experimental conditions, such as ion energy, ion flux and temperature. With *ex situ* methods it is only feasible to study how the final structure depends on the experimental conditions. A good understanding of how the experimental conditions influence the formation may make it easier to produce structures with desirable shape and size.

As nanostructures are small compared to the wavelength of light, they can in many cases be approximated as an effective media with an effective dielectric function. If the structures have an anisotropic shape, the effective dielectric function representing the structure will also be anisotropic, even though the material constituting the structures are optically isotropic [29, 30]. This is often referred to as shape anisotropy. To correctly treat anisotropic materials, it is in general necessary to perform generalized ellipsometry or Mueller matrix ellipsometry [7]. Therefore, a Mueller matrix ellipsometer was applied for this real-time study of sputtering of GaSb, to account for any possible anisotropic optical properties of the nanostructures.

The theoretical background of generalized ellipsometry and Mueller matrix ellipsometry is introduced in chapter 2. Chapter 3 gives a short introduction to sputtering, and a description of the structures that form on a GaSb surface during sputtering. Two competing explanations for the formation are presented. In chapter 4 an anisotropic graded effective medium model used to represent the nanopillars is introduced. The details of the experimental setup used for the real-time observations of sputtering of GaSb are discussed in chapter 5. Chapter 6

gives a summary of the results of the ellipsometry studies of the GaSb nanopillars, followed by six published papers.

Chapter 2

Theoretical background

In this chapter I will give a short introduction to polarized light and ellipsometry. Different ways to represent polarized light and linear interactions of polarized light with materials will be treated, and connected to what can be measured with an ellipsometer.

2.1 Polarized light and ellipsometry

The electric field of a monochromatic electromagnetic wave propagating along the z-axis, can be expressed as a superposition of two orthogonal field components,

$$\mathbf{E}(z,t) = \mathrm{Re}\left\{E_{x0}\cdot \mathrm{e}^{\mathrm{i}(\omega t - 2\pi z/\lambda + \delta_x)}\right\}\hat{\boldsymbol{x}} + \mathrm{Re}\left\{E_{y0}\cdot \mathrm{e}^{\mathrm{i}(\omega t - 2\pi z/\lambda + \delta_y)}\right\}\hat{\boldsymbol{y}}. \tag{2.1}$$

The $\mathrm{e}^{\mathrm{i}\omega t}$ time dependence have been chosen according to the 1968 Nebraska ellipsometry convention [31], resulting in negative imaginary parts of dielectric functions. The polarization of such a wave will be given by the field amplitudes of the two components (E_{x0} and E_{y0}), and the relative phase difference ($\delta = \delta_y - \delta_x$) between them. These can conveniently be gathered into a complex vector, denoted a Jones vector, that describes the polarization state of light.

$$\mathbf{E} = \mathrm{Re}\left\{\begin{bmatrix} E_{0x}\mathrm{e}^{\mathrm{i}\delta_x} \\ E_{0y}\mathrm{e}^{\mathrm{i}\delta_y} \end{bmatrix}\cdot \mathrm{e}^{\mathrm{i}(\omega t - 2\pi z/\lambda)}\right\} \tag{2.2}$$

The change of a polarization state after an interaction (*e.g.* an reflection from a surface) can be described by a 2×2 complex matrix, denoted a Jones matrix

$$\begin{bmatrix} E_x \\ E_y \end{bmatrix}^{\mathrm{out}} = \begin{bmatrix} a & b \\ c & d \end{bmatrix}\begin{bmatrix} E_x \\ E_y \end{bmatrix}^{\mathrm{inc}}, \tag{2.3}$$

where E_x and E_y are the complex elements of the Jones vectors, and the complex elements a, b, c and d are transmission or reflection coefficients. The Jones formalism can only treat coherent light and linear interactions.

To deal with quasi-monochromatic light that can be partially polarized, one can use the Mueller–Stokes formalism. Any polarization state of light can be completely described by four real parameters denoted the Stokes parameters [32], which often are arranged into a column matrix and denoted a Stokes vector,

$$\boldsymbol{S} = \begin{bmatrix} I \\ Q \\ U \\ V \end{bmatrix} = \begin{bmatrix} \langle E_{x0}(t)^2 \rangle + \langle E_{y0}(t)^2 \rangle \\ \langle E_{x0}(t)^2 \rangle - \langle E_{y0}(t)^2 \rangle \\ 2\langle E_{x0}(t) E_{y0}(t) \cos\delta(t) \rangle \\ 2\langle E_{x0}(t) E_{y0}(t) \sin\delta(t) \rangle \end{bmatrix}.$$

For quasi-monochromatic light the field amplitudes and phase difference will be time dependent, and $\langle \cdot \rangle$ denotes time-averages. The first element of the Stokes vector (I) is a measure of the total light intensity and the three other elements are intensity differences for different polarization components. Q is the difference between the linearly polarized light intensity along the x and y direction, U is the difference between $\pm 45°$ linearly polarized light, and V is the difference between left and right circular polarized light. The degree of polarization (DOP) of a Stokes vector can be defined as

$$\text{DOP} = \frac{\sqrt{Q^2 + U^2 + V^2}}{I}, \tag{2.4}$$

taking the value 0 for unpolarized light and the value 1 for totally polarized light.

The change of a polarization state, represented by a Stokes vector, can be described by a 4×4 real-valued transformation matrix called a Mueller matrix, $\mathbf{M}$, connecting an incoming Stokes vector, $\mathbf{S}_{\text{in}}$, to an outgoing Stokes vector, $\mathbf{S}_{\text{out}}$,

$$\mathbf{S}_{\text{out}} = \mathbf{M}\mathbf{S}_{\text{in}}. \tag{2.5}$$

The Mueller matrix can describe the effect of any linear interaction of light with a sample or an optical element. Polarization effects contained in a Mueller matrix could be diattenuation (different amplitude transmittance or reflectance for different polarization modes), retardance (changing δ), and depolarization (which increases the random component of the electric field).

A Mueller matrix that does not reduce the degree of polarization of a Stokes vector, referred to as a Mueller–Jones matrix, can be represented by a corresponding Jones matrix. The Mueller matrix, $\mathbf{M}$, representing a Jones matrix, $\mathbf{J}$, is given as [6]

$$\mathbf{M} = \mathbf{A}(\mathbf{J} \otimes \mathbf{J}^*)\mathbf{A}^{-1}, \tag{2.6}$$

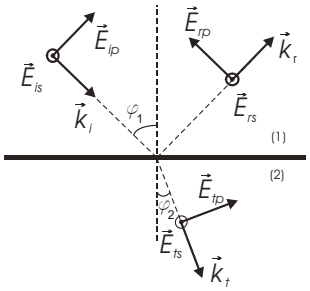

Figure 2.1: Field components for light reflected and transmitted at a smooth surface between two materials.

where $\otimes$ denotes the Kronecker product, * the complex conjugate and $\mathbf{A}$ is a conversion matrix,

$$\mathbf{A} = \begin{bmatrix} 1 & 0 & 0 & 1 \\ 1 & 0 & 0 & -1 \\ 0 & 1 & 1 & 0 \\ 0 & \mathrm{i} & -\mathrm{i} & 0 \end{bmatrix}.$$

2.1.1 Ellipsometric parameters

I will here introduce the most used ellipsometric parameters (standard, generalized and Mueller).

2.1.2 *Standard* ellipsometry of isotropic materials

Measurements of the polarization of light is usually referred to as polarimetry. Ellipsometry is a type of polarimetric measurement where one measures the relative change of phase and amplitude between two orthogonal electric field components after a reflection. From the boundary conditions of Maxwell's equations, the field component parallel to the plane of incidence (E_p) will be changed differently by a reflection than the component orthogonal to the plane of incidence (E_s). A sketch of the incoming and reflected field components can be seen in figure 2.1. In this case the Jones matrix in the $p-s$ basis will read

$$\begin{bmatrix} E_p \\ E_s \end{bmatrix}^{\text{refl.}} = \begin{bmatrix} r_{pp} & r_{ps} \\ r_{sp} & r_{ss} \end{bmatrix} \begin{bmatrix} E_p \\ E_s \end{bmatrix}^{\text{inc}}. \tag{2.7}$$

For light reflected at a plane interface between two isotropic materials there will be no coupling between orthogonal field components ($r_{ps} = r_{sp} = 0$), and r_{pp} and

r_{ss} are given by Fresnel's equations [6],

$$r_{pp} = \frac{\tilde{n}_2 \cos\phi_1 - \tilde{n}_1 \cos\phi_2}{\tilde{n}_2 \cos\phi_1 + \tilde{n}_1 \cos\phi_2}, \quad r_{ss} = \frac{\tilde{n}_1 \cos\phi_1 - \tilde{n}_2 \cos\phi_2}{\tilde{n}_1 \cos\phi_1 + \tilde{n}_2 \cos\phi_2}, \tag{2.8}$$

where $\tilde{n}_1$ and $\tilde{n}_2$ are the complex index of refractions of the two materials, and ϕ_1 and ϕ_2 are the incident and refracted angle. The resulting change of polarization from such a reflection can be described by the complex ratio

$$\rho = \frac{r_{pp}}{r_{ss}} = \tan\psi e^{\mathrm{i}\Delta}, \tag{2.9}$$

which often is expressed by the two ellipsometric angles ψ and Δ. ψ describes the relative change of amplitude ($|r_{pp}/r_{ss}| = \tan\psi$) and Δ describes the relative phase change between the two orthogonal field components. A *standard* ellipsometer measures these two parameters in some way, typically from Fourier components of a reflected signal modulated by *e.g.* a rotating analyzer or compensator, or a photoelastic phase modulator. In spectroscopic ellipsometry ψ and Δ are measured over a range of wavelengths.

2.1.3 Generalized/Mueller matrix ellipsometry of anisotropic materials

For reflections from an anisotropic material, there will in general be coupling between orthogonal field components ($r_{ps} \neq 0$ and $r_{sp} \neq 0$). This can also be the case for nanostructures of isotropic materials, but with an anisotropic shape. *Standard* ellipsometry is not sufficient to fully characterize the polarization altering properties of such samples, generalized ellipsometry or Mueller matrix ellipsometry is necessary. A generalized ellipsometer is capable of measuring the normalized Jones matrix of reflections from a sample. This can be done by extending the standard ellipsometry techniques by performing several measurements of the Fourier components of a *standard* ellipsometer at different configurations [33]. The normalized Jones matrix contains three complex ratios:

$$\rho_{pp} = \frac{r_{pp}}{r_{ss}} = \tan\psi_{pp} e^{\mathrm{i}\Delta_{pp}}, \quad \rho_{ps} = \frac{r_{ps}}{r_{ss}} = \tan\psi_{ps} e^{\mathrm{i}\Delta_{ps}}, \quad \text{and } \rho_{sp} = \frac{r_{sp}}{r_{ss}} = \tan\psi_{sp} e^{\mathrm{i}\Delta_{sp}}. \tag{2.10}$$

Note that ρ_{pp} is defined the same way as ρ for an isotropic material. ρ_{pp} for an anisotropic material can not, however, be measured by a *standard* ellipsometry measurement, because of the possibility of mode coupling. One should beware that different definitions of the generalized ellipsometry parameters exists in the literature. Schubert applied a different convention in the *Handbook of Ellipsometry* [33], defining $R_{ps} = r_{ps}/r_{pp}$ and $R_{sp} = r_{sp}/r_{ss}$, and having r_{ps} denote the

coefficient for a p polarized incident wave and s polarized outgoing wave. This is the opposite of the notation applied in this work, adopted from Azzam and Bashara [6].

In Mueller ellipsometry one measures all the 16 elements of the Mueller matrix. In generalized ellipsometry one does not necessarily perform enough measurements to derive the full Mueller matrix. Only a subset of the matrix may be measured which, in the absence of depolarization, is sufficient to derive the normalized Jones matrix. To measure depolarizing samples, full Mueller matrix ellipsometry is necessary. In this case a corresponding Jones matrix does not exist. For samples with small depolarization effects, various methods can be used to find the closest corresponding Jones matrix from a Mueller matrix [34, 35, 36].

In the case of a reflection from an isotropic and non-depolarizing smooth material, the Mueller matrix can be expressed as

$$\mathbf{M}_{\text{iso}} = \frac{|r_{pp}|^2 + |r_{ss}|^2}{2} \begin{bmatrix} 1 & -\cos 2\Psi & 0 & 0 \\ -\cos 2\Psi & 1 & 0 & 0 \\ 0 & 0 & \sin 2\Psi \cos\Delta & \sin 2\Psi \sin\Delta \\ 0 & 0 & -\sin 2\Psi \sin\Delta & \sin 2\Psi \cos\Delta \end{bmatrix}, \tag{2.11}$$

with Ψ and Δ defined in equation 2.9. This matrix is said to be block-diagonal; the corresponding Jones matrix is diagonal. This matrix can also represent the reflection from multiple plane parallel isotropic layers. For a reflection from an anisotropic and non-depolarizing material, the Mueller matrix can be expressed by the reflection coefficients through equation (2.6),

$$\mathbf{M}_{\text{aniso}} = \tag{2.12}$$

$$\begin{bmatrix} \frac{1}{2}(|r_{pp}|^2 + |r_{sp}|^2 + |r_{ps}|^2 + |r_{ss}|^2) & \frac{1}{2}(|r_{pp}|^2 + |r_{sp}|^2 - |r_{ps}|^2 - |r_{ss}|^2) & \mathrm{Re}(r_{pp}r_{ps}^* + r_{sp}r_{ss}^*) & \mathrm{Im}(r_{pp}r_{ps}^* + r_{sp}r_{ss}^*) \\ \frac{1}{2}(|r_{pp}|^2 - |r_{sp}|^2 + |r_{ps}|^2 - |r_{ss}|^2) & \frac{1}{2}(|r_{pp}|^2 - |r_{sp}|^2 - |r_{ps}|^2 + |r_{ss}|^2) & \mathrm{Re}(r_{pp}r_{ps}^* - r_{sp}r_{ss}^*) & \mathrm{Im}(r_{pp}r_{ps}^* - r_{sp}r_{ss}^*) \\ \mathrm{Re}(r_{pp}r_{sp}^* + r_{ps}r_{ss}^*) & \mathrm{Re}(r_{pp}r_{sp}^* - r_{sp}r_{ss}^*) & \mathrm{Re}(r_{pp}r_{ss}^* + r_{ps}r_{sp}^*) & \mathrm{Im}(r_{pp}r_{ss}^* - r_{ps}r_{sp}^*) \\ -\mathrm{Im}(r_{pp}r_{sp}^* + r_{ps}r_{ss}^*) & -\mathrm{Im}(r_{pp}r_{sp}^* - r_{ps}r_{ss}^*) & -\mathrm{Im}(r_{pp}r_{ss}^* + r_{ps}r_{sp}^*) & \mathrm{Re}(r_{pp}r_{ss}^* - r_{ps}r_{sp}^*) \end{bmatrix}.$$

2.2 Reflections from anisotropic layers

The Fresnel equations (2.8) give the reflection coefficients for an isotropic plane boundary. This allows deriving the complex refractive index of a material from the two parameters Ψ and Δ measured by *standard* ellipsometry. For light reflected from a sample with a layered structure, the reflected wave will be a superposition of waves reflected from the different boundaries, including multiple reflections. For layers that are thin compared to the coherence length of the light, the waves reflected from the different boundaries will interfere. By modeling the resulting

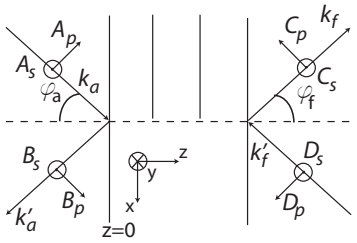

Figure 2.2: Incident, reflected, and transmitted modes of a layered anisotropic material.

reflection coefficients for a layered sample, spectroscopic ellipsometry is highly sensitive to layer thickness and refractive index.

The reflection coefficients for a plane wave reflected from a stack of anisotropic layers with plane parallel boundaries can be calculated by a 4×4 matrix algorithm developed by Berreman and others [37, 38, 39, 40]. This algorithm is described in detail in the *Handbook of ellipsometry* [33], and is implemented in software included with several commercial ellipsometers. Therefore, only a brief description of the method is given here. For a stack of isotropic materials the simpler Abelès 2×2 matrix method [6] can be applied.

The reflection coefficients from a layered structure can be found by solving Maxwells equations with the appropriate boundary conditions (the tangential components of the electric and magnetic fields are continuous over the boundaries). A transfer matrix $\mathbf{T}$ is defined to connect the complex amplitudes of the incident (A_s, A_p), reflected (B_s, B_p) and transmitted (C_s, C_p) waves for the s and p modes

$$\begin{bmatrix} A_s \\ B_s \\ A_p \\ B_p \end{bmatrix} = \mathbf{T} \cdot \begin{bmatrix} C_s \\ D_s \\ C_p \\ D_p \end{bmatrix} = \begin{bmatrix} T_{11} & T_{12} & T_{13} & T_{14} \\ T_{21} & T_{22} & T_{23} & T_{24} \\ T_{31} & T_{32} & T_{33} & T_{34} \\ T_{41} & T_{42} & T_{43} & T_{44} \end{bmatrix} \cdot \begin{bmatrix} C_s \\ D_s \\ C_p \\ D_p \end{bmatrix}, \tag{2.13}$$

If the layered structure rests on an infinite substrate, and is illuminated from the ambient side only, there will be no back traveling modes ($D_p = D_s = 0$). In that case the elements of the Jones matrix for reflection is given from the transfer matrix as,

$$r_{pp} = \left(\frac{B_p}{A_p}\right)_{A_s=0} = \frac{T_{11}T_{43} - T_{41}T_{13}}{T_{11}T_{33} - T_{13}T_{31}}, \quad r_{ps} = \left(\frac{B_p}{A_s}\right)_{A_p=0} = \frac{T_{41}T_{33} - T_{43}T_{31}}{T_{11}T_{33} - T_{13}T_{31}}$$
$$r_{sp} = \left(\frac{B_s}{A_p}\right)_{A_s=0} = \frac{T_{11}T_{23} - T_{21}T_{13}}{T_{11}T_{33} - T_{13}T_{31}}, \quad r_{ss} = \left(\frac{B_s}{A_s}\right)_{A_p=0} = \frac{T_{21}T_{33} - T_{23}T_{31}}{T_{11}T_{33} - T_{13}T_{31}}.$$

For each layer in the structure a partial transfer matrix, $\mathbf{T}_p$, can be defined that connects the in-plane wave components at the front and back side of the layer. Due to the boundary conditions the tangential components of the fields at the back side of one layer must be equal to the fields at the front side of the next layer. The fields at the first and last interface of a stack of layers can then simply be connected by the product of the partial transfer matrices of each layer, in the given order. The matrix $\mathbf{T}$ for structure consisting of N layers, with layer i having the partial matrix $\mathbf{T}_i(d_i)$ and thickness d_i, can be expressed as

$$\mathbf{T} = \mathbf{L}_a^{-1} \prod_{i=1}^{N} [\mathbf{T}_{ip}(d_i)]^{-1} \mathbf{L}_f = \mathbf{L}_a^{-1} \prod_{i=1}^{N} [\mathbf{T}_{ip}(-d_i)] \mathbf{L}_f, \tag{2.14}$$

where $\mathbf{L}_a$ is a matrix projecting the incident and reflected fields into the tangential plane, and $\mathbf{L}_f$ projects the transmitted fields from tangential plane in the substrate to a plane normal to propagation direction of the transmitted wave. $\mathbf{L}_a^{-1}$ for an isotropic ambient can be found from geometrical considerations to be

$$\mathbf{L}_a^{-1} = \begin{bmatrix} 0 & 1 & -1/\tilde{n}_a \cos\phi_a & 0 \\ 0 & 1 & 1/\tilde{n}_a \cos\phi_a & 0 \\ 1/\cos\phi_a & 0 & 0 & 1/\tilde{n}_a \\ -1/\cos\phi_a & 0 & 0 & 1/\tilde{n}_a \end{bmatrix}, \tag{2.15}$$

where $\tilde{n}_a$ is the complex index of refraction of the ambient medium and ϕ_a is the angle of incidence. $\mathbf{L}_f$ for an isotropic substrate is

$$\mathbf{L}_f = \begin{bmatrix} 0 & 0 & \cos\phi_f & 0 \\ 1 & 0 & 0 & 0 \\ -\tilde{n}_f \cos\phi_f & 0 & 0 & \\ 0 & 0 & \tilde{n}_f & 0 \end{bmatrix}, \tag{2.16}$$

where $\tilde{n}_f$ is the complex index of refraction of the substrate, and ϕ_f is the angle of refraction found by Snell's law.

2.2.1 Partial transfer matrix

The partial transfer matrix of a layer is found by solving four differential equations derived by Berreman [37] from first-order Maxwell equations. The in-plane

components of the electric and magnetic fields in Gaussian units and Cartesian coordinates were shown to follow

$$\partial_z \vec{\Psi}(z) = -\mathrm{i}k_0 \mathbf{\Delta}(z)\vec{\Psi}(z),$$
$$\vec{\Psi}(z) = (E_x, E_y, H_x, H_y)^{\mathrm{T}}(z), \quad k_0 \equiv \frac{\omega}{c}, \tag{2.17}$$

where ω is the angular frequency of the field, c the vacuum speed of light, $\mathbf{\Delta}$ is a 4×4 matrix, and $(\cdot)^{\mathrm{T}}$ denotes the transpose. The media is assumed non-magnetic ($\mu = \mathbf{I}$, where $\mathbf{I}$ denotes the unity matrix) and non-gyrotropic. In this case the dielectric tensor $\boldsymbol{\varepsilon}$ can be reduced to only three non-zero elements on the tensors diagonal, one for each of the anisotropic material's principal axes. An arbitrary oriented medium can be described by an Euler rotation of the dielectric tensor in the principal system

$$\boldsymbol{\varepsilon} = \mathbf{E}_r(\phi, \theta, \psi) \begin{bmatrix} \varepsilon_{x'} & 0 & 0 \\ 0 & \varepsilon_{y'} & 0 \\ 0 & 0 & \varepsilon_{z'} \end{bmatrix} \mathbf{E}_r(-\phi, -\theta, -\psi),$$

where ϕ, θ, ψ are the Euler angles, $\mathbf{E}_r$ is the Euler rotation matrix, and $\varepsilon_{x'}, \varepsilon_{y'}, \varepsilon_{z'}$ are the dielectric functions along the respective principal axes of the anisotropic medium. The rotation matrix is given as [41],

$$\mathbf{E}(\phi, \theta, \psi) = \begin{bmatrix} \cos\psi & \sin\psi & 0 \\ -\sin\psi & \cos\psi & 0 \\ 0 & 0 & 1 \end{bmatrix} \begin{bmatrix} 1 & 0 & 0 \\ 0 & \cos\theta & \sin\theta \\ 0 & -\sin\theta & \cos\theta \end{bmatrix} \begin{bmatrix} \cos\phi & \sin\phi & 0 \\ -\sin\phi & \cos\phi & 0 \\ 0 & 0 & 1 \end{bmatrix}.$$

The matrix $\mathbf{\Delta}$ is given by the dielectric tensor ε of the layer, and the x-component k_x of the incident wave-vector $\vec{k}_a$,

$$\mathbf{\Delta} = \begin{bmatrix} -k_x \frac{\varepsilon_{31}}{\varepsilon_{33}} & -k_x \frac{\varepsilon_{32}}{\varepsilon_{33}} & 0 & 1 - \frac{k_x^2}{\varepsilon_{33}} \\ 0 & 0 & 0 & 0 \\ \varepsilon_{23}\frac{\varepsilon_{31}}{\varepsilon_{33}} - \varepsilon_{21} & k_x^2 - \varepsilon_{22} + \varepsilon_{23}\frac{\varepsilon_{32}}{\varepsilon_{33}} & 0 & k_x \frac{\varepsilon_{23}}{\varepsilon_{33}} \\ \varepsilon_{11} - \varepsilon_{13}\frac{\varepsilon_{31}}{\varepsilon_{33}} & \varepsilon_{12} - \varepsilon_{13}\frac{\varepsilon_{32}}{\varepsilon_{33}} & 0 & -k_x \frac{\varepsilon_{13}}{\varepsilon_{33}} \end{bmatrix},$$

with $k_x = \tilde{n}_a \sin\Phi_a$. For a homogeneous medium this matrix is independent of z. The differential equations in 2.17 have exponential solutions, and can be expressed by the partial transfer matrix $\mathbf{T}_p$ as

$$\begin{aligned} \vec{\Psi}(z+d) &= \mathrm{e}^{-\mathrm{i}\frac{\omega}{c}\mathbf{\Delta}d}\vec{\Psi}(z) = \mathbf{T}_p(d)\vec{\Psi}(z), \\ \mathbf{T}_p(d) &= \mathrm{e}^{-\mathrm{i}\frac{\omega}{c}\mathbf{\Delta}d}. \end{aligned} \tag{2.18}$$

$\mathbf{T}_p(d)$ describe how the field components at the front and back of the layer are connected, and includes the effect of all multiple reflections. For thin layers, it can be found by expanding the exponential function in a common series in the spectrally varying factor $(\frac{\omega}{c}d)$. A numerically faster method can be found by applying Cayley–Hamilton's theorem [38]. This theorem states that the matrix function $\boldsymbol{T}_p(d)$ can be expressed as a finite series up to the power of $n-1$, where $n \times n$ are the dimensions of the matrix. This implies that $\mathbf{T}_p$ can be expressed as

$$\mathbf{T}_p \equiv \mathrm{e}^{-\mathrm{i}\frac{\omega}{c}\boldsymbol{\Delta}d} = \beta_0\mathbf{I} + \beta_1\boldsymbol{\Delta} + \beta_2\boldsymbol{\Delta}^2 + \beta_3\boldsymbol{\Delta}^3, \tag{2.19}$$

where $\mathbf{I}$ is the identity matrix and the scalars β_i must obey the equations,

$$\mathrm{e}^{-\mathrm{i}\frac{\omega}{c}\lambda_k d} = \sum_{j=0}^{3} \beta_j \lambda_k^j, \quad k = 1, ..., 4,$$

where λ_k are the eigenvalues of $\boldsymbol{\Delta}$. Equation 2.19 is also valid for thick layers. Wohler *et al.*[38] have found that the solutions for β_i can be written on the following form,

$$\begin{aligned}
\beta_0 &= -\sum_{i=1}^{4} \lambda_j\lambda_k\lambda_l \frac{f_i}{\lambda_{ij}\lambda_{ik}\lambda_{il}}, \quad \beta_1 = \sum_{i=1}^{4} (\lambda_j\lambda_k + \lambda_j\lambda_l + \lambda_k\lambda_l)\frac{f_i}{\lambda_{ij}\lambda_{ik}\lambda_{il}}, \\
\beta_2 &= -\sum_{i=1}^{4} (\lambda_j + \lambda_k + \lambda_l)\frac{f_i}{\lambda_{ij}\lambda_{ik}\lambda_{il}}, \quad \beta_3 = \sum_{i=1}^{4} \frac{f_i}{\lambda_{ij}\lambda_{ik}\lambda_{il}},
\end{aligned}$$

where $\lambda_{ij} = \lambda_i - \lambda_j$ and $f_i = \mathrm{e}^{-\mathrm{i}k_o\lambda_i h}$, with $i, j, k, l = 1, ..., 4$.

The values of the indices i, j, k and l are all different from each other. Note that all the eigenvalues appear in an equal manner, making the equations independent on the order of the eigenvalues. Each of these eigenvalues is associated with one of the four plane waves existing in the homogeneous layer. The two solutions that have a negative real part constitute forward traveling waves, while those associated with the eigenvalues with a positive real part are backward traveling. Note that this is the opposite of reference [42], since a different sign is used for the time dependence of the electric field.

In the special case of a layer of isotropic material the transfer matrix is given as

$$\mathbf{T}_p = \begin{bmatrix} \cos(k_0 d\lambda) & 0 & 0 & -\mathrm{i}\frac{\lambda}{\varepsilon}\sin(k_0 d\lambda) \\ 0 & \cos(k_0 d\lambda) & \frac{\mathrm{i}}{\lambda}\sin(k_0 d\lambda) & 0 \\ 0 & \mathrm{i}\lambda\sin k_0 d\lambda & \cos k_0 d\lambda & 0 \\ -\mathrm{i}\frac{\varepsilon}{\lambda}\sin(k_0 d\lambda) & 0 & 0 & \cos(k_0 d\lambda) \end{bmatrix},$$

where $\pm\lambda$ are the degenerate eigenvalues of the $\boldsymbol{\Delta}$ matrix,

$$\lambda_1 = \lambda_2 = -\lambda_3 = -\lambda_4 \equiv \lambda = \sqrt{\varepsilon - k_x^2} = \sqrt{\tilde{n}^2 - \tilde{n}_a^2 \sin^2\Phi_a},$$

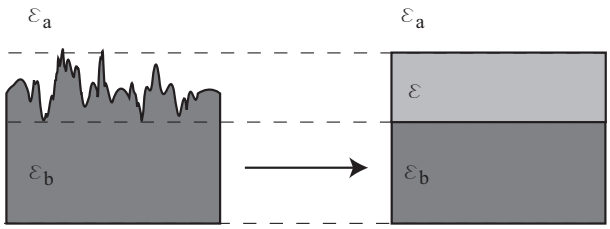

Figure 2.3: Sketch of an effective medium representaion of a rough surface.

and ε is the isotropic dielectric function of the layer.

2.3 Effective medium models

To be able to characterize nanostructures from ellipsometric measurements, one needs to model their optical properties in some way. A heterogeneous material with inhomogeneities of sizes sufficiently smaller than the wavelength of a light wave will appear like a homogeneous material for the wave. This means that there will be no scattering from the material, and the material's optical properties can be described by an effective dielectric function. The reflection coefficients for plane waves reflected from such a material can then be calculated by the approach outlined in section 2.2. Using ellipsometry it is then possible to measure the dielectric function and layer thickness of an effective homogeneous material representing a nanostructured surface, as sketched in figure 2.3. Different mixing formulas or effective medium theories can be used to find the volume filling factors of the mixed materials or inclusion shapes [30]. In this section I will briefly discuss the basic concepts of effective medium theories and present some of the most used formulas.

2.3.1 Claussius-Mossotti's equation

Many of the effective medium equations are based on the principles of the Claussius-Mossotti's equation [43], that relates the microscopic polariziability of a large number of molecules, represented by point dipoles, to the collective macroscopic polarizability of all the molecules. If a dielectric medium is placed in an external electric field $\boldsymbol{E}$, an electric polarization $\boldsymbol{P}$ (dipole moment per unit volume) will be induced in the medium, given by (in Gaussian units)

$$\boldsymbol{P} = \chi_e \boldsymbol{E},$$

where χ_e is the macroscopic electric susceptibility of the medium. Each point dipole contributes to the total polarization with its microscopic polarizability α times the electric field at the point. If the molecules are closely packed, the neighboring point dipoles will contribute to the electric field, giving rise to an internal field $\boldsymbol{E}_i$ in addition to the macroscopic external field $\boldsymbol{E}$. The total field at a point will then be $\boldsymbol{E} + \boldsymbol{E}_i$. The internal field can be expressed as the difference between two terms, $\boldsymbol{E}_i = \boldsymbol{E}_{\text{near}} - \boldsymbol{E}_P$, where $\boldsymbol{E}_{\text{near}}$ represent the contribution from the nearest neighbors and $\boldsymbol{E}_P$ is the contribution from the average continuum approximation described by the macroscopic polarization $\boldsymbol{P}$. By integrating over a sphere containing many molecules, the average electric field inside the sphere can be found to be [43],

$$\boldsymbol{E}_P = -\frac{4\pi}{3}\boldsymbol{P}.$$

$\boldsymbol{E}_{\text{near}}$ can be shown to be zero for molecules in a simple cubic lattice, and it is expected to be zero also for the case of a completely random organization.

If $\langle \boldsymbol{p}_{\text{mol}} \rangle$ is the average dipole moments of the molecules, the total polarization vector will be,

$$\boldsymbol{P} = N\langle \boldsymbol{p}_{\text{mol}} \rangle,$$

where N is the average number of molecules per unit volume, and

$$\langle \boldsymbol{p}_{\text{mol}} \rangle = \alpha(\boldsymbol{E} + \boldsymbol{E}_i)$$

This gives (with $\boldsymbol{E}_{\text{near}} = 0$)

$$\boldsymbol{P} = N\alpha(\boldsymbol{E} + \frac{4\pi}{3}\boldsymbol{P}),$$

which solved for $\boldsymbol{P}$ gives the macroscopic electric susceptibility,

$$\chi_e = \frac{\boldsymbol{P}}{\boldsymbol{E}} = \frac{N\alpha}{1 - \frac{4\pi}{3}N\alpha}.$$

Using $\varepsilon = 1 + 4\pi\chi_e$ (Gaussian units) we get Claussius-Mossotti's equation

$$\frac{\varepsilon - 1}{\varepsilon + 2} = \frac{4\pi}{3}N\alpha, \tag{2.20}$$

where ε is the macroscopic dielectric function of the collection of molecules, depending on the microscopic polarizability, α, and the number density, N.

2.3.2 Effective medium equations; Lorentz-Lorenz, Maxwell-Garnett and Bruggeman

Claussius-Mossotti's equation (equation (2.20)) relates microscopic polarizabilities to a macroscopic dielectric function. Based on this equation one can develop relations for the dielectric function of a heterogeneous material consisting of microscopic regions with different dielectric functions. Such relations are called effective medium equations or electromagnetic mixing formulas.

Claussius-Mossotti's equation can be generalized to a random mixture of points with two different polarizabilities, α_a and α_b, with volume densities N_a and N_b:

$$\frac{\varepsilon - 1}{\varepsilon + 2} = \frac{4\pi}{3}(N_a\alpha_a + N_b\alpha_b). \tag{2.21}$$

Using equation (2.20) again on the two terms on the right, one gets the Lorentz-Lorenz effective medium expression [44],

$$\frac{\varepsilon - 1}{\varepsilon + 2} = f_a\frac{\varepsilon_a - 1}{\varepsilon_a + 2} + f_b\frac{\varepsilon_b - 1}{\varepsilon_b + 2}, \tag{2.22}$$

where f_i represent the volume fraction of the ith phase:

$$f_i = \frac{N_i}{\sum_j N_j}, \ \sum_i f_i = 1.$$

To find the properties for a system made up by more than two different materials, one can simply add more terms to equation (2.22).

Another equation can be derived from Claussius-Mossotti's equation (2.20) by considering the heterogeneous material to consist of inclusions of a material a embedded in a host material b. The simplest case is to consider spherical inclusions. The polarizability α_a of a sphere with radius r_a and dielectric function ε_a embedded in a media with dielectric function ε_b can be shown to be (from Laplace's equation with proper boundary conditions) [43]

$$\alpha_a = r_a^3\frac{\varepsilon_a - \varepsilon_b}{\varepsilon_a + 2\varepsilon_b}.$$

For spheres that are sufficiently small compared to the wavelength of light, the principles of Claussius-Mossotti's equation can be extended to spheres with ε_a embedded in a media with dielectric function ε_b,

$$\frac{\varepsilon - \varepsilon_b}{\varepsilon + 2\varepsilon_b} = f_a\frac{\varepsilon_a - \varepsilon_b}{\varepsilon_a + 2\varepsilon_b}, \tag{2.23}$$

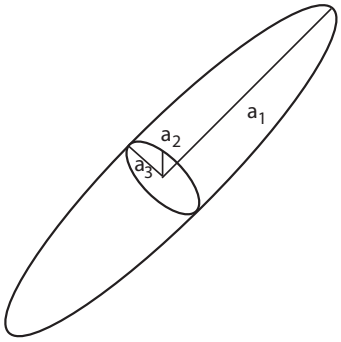

Figure 2.4: The three semi-axes of an ellipsoid.

where f_a is the volume fraction of the spheres,

$$f_a = \frac{4\pi}{3}\frac{r_a^3}{V}.$$

V is the total volume divided by the number of spheres. Equation (2.23) is the much used Maxwell-Garnett equation, introduced by Maxwell-Garnett in 1904 to explain the colors in metal glasses [30]. The strong spectrally dependent absorption of metal particles in glass is caused by a plasmon resonance for wavelengths where $\mathrm{Re}\{\epsilon_a\} = -2\mathrm{Re}\{\epsilon_b\}$.

Maxwell-Garnett treats the two mixed components on an unequal footing, in the way that interchanging ε_a and ε_b and f_a and f_b gives a different effective ε. Some authors [44, 29] argue that such an interchange is more appropriate if $f_a > f_b$, *i.e.* the media with the lowest filling factor should be an inclusion in the media with the highest filling factor. Bruggeman resolved this issue by proposing that the inclusions should be embedded in the effective medium itself, leading to what is known as the Bruggeman effective medium expression, or just the effective-medium approximation [30, 44],

$$0 = f_a\frac{\varepsilon_a - \varepsilon}{\varepsilon_a + 2\varepsilon} + f_b\frac{\varepsilon_b - \varepsilon}{\varepsilon_b + 2\varepsilon}, \tag{2.24}$$

where f_a is the volume fraction of material a and $f_b = 1 - f_a$ is the volume fraction of material b. The Bruggeman equation represents an aggregate mixture, where the two materials are mixed on a random basis.

2.3.3 Anisotropic effective medium models

If the inclusions in the heterogeneous material have an ellipsoidal shape instead of a spherical, the broken symmetry means the the induced polarization of the

ellipsoid will depend on the direction of the electric field. The polarizability α_i of an ellipsoid along one of the semi-axes a_i $(i = 1, 2, 3)$ is given as

$$\alpha_i = \frac{a_1 a_2 a_3}{3} \frac{\varepsilon_a - \varepsilon_b}{\varepsilon_b + L_i(\varepsilon_a - \varepsilon_b)}.$$

L_i is the depolarization factor for the direction along a_i, given as [30]

$$L_1 = \frac{a_1 a_2 a_3}{2} \int_0^\infty \frac{ds}{(s + a_1^2)\sqrt{(s + a_1^2)(s + a_2^2)(s + a_3^2)}}$$

for L_1. To find L_2 (L_3), interchange a_2 and a_1 (a_3 and a_1). The depolarization factors can have values between 0 and 1, and must satisfy $L_1 + L_2 + L_3 = 1$. For a sphere all three factors are equal to $1/3$. A disk will have the factors $(1, 0, 0)$, and a needle will have $(0, 1/2, 1/2)$.

The Maxwell-Garnett equation can be generalized to inclusions of oriented ellipsoids,

$$\frac{\varepsilon_i - \varepsilon_b}{\varepsilon_i + 2\varepsilon_b} = \frac{f_a}{3} \frac{\varepsilon_a - \varepsilon_b}{\varepsilon_b + L_i(\varepsilon_a - \varepsilon_b)}, \tag{2.25}$$

where ε_i is the effective dielectric function in a direction i, along semi-axis a_i of the ellipsoid (see figure 2.4). The geometrical shape of the microscopic inclusions makes the effective medium anisotropic. Equation (2.25) provides the diagonal elements of the effective dielectric tensor in the principal coordinate system corresponding with the orientation of the semi axes of the ellipsoid. Equation (2.25) is sometimes referred to as the Bragg-Pippard equation [29].

Analogous to the generalization of the Maxwell-Garnett equation, the Bruggeman effective medium equation (2.24) can also be generalized for ellipsoidal inclusion to [45]:

$$0 = f_a \frac{\varepsilon_a - \varepsilon_i}{\varepsilon_i + L_i(\varepsilon_a - \varepsilon_i)} + f_b \frac{\varepsilon_b - \varepsilon_i}{\varepsilon_i + L_i(\varepsilon_b - \varepsilon_i)}. \tag{2.26}$$

The common factor $1/3$ from the polarizability of an ellipsoid has been omitted. In the special case of $L_i = 0$ or $L_i = 1$ equation (2.26) reduces to what is known as the Wiener bounds [44]. $L_i = 0$ corresponds to no screening between the inclusions, which is the case when the electric field is parallel to the boundaries between the mixed materials. Equation (2.26) then reduces to the weighted average,

$$\varepsilon_i = f_a \varepsilon_a + f_b \varepsilon_b. \tag{2.27}$$

In the opposite extreme maximum screening occurs when the field is normal to the boundaries and $L_i = 1$,

$$\varepsilon_i = \left(f_a/\varepsilon_a + f_b/\varepsilon_b\right)^{-1}.$$

2.3.4 Assumptions and limitations

The effective medium equations discussed above are based on several assumptions, limiting their validity.

- **The quasi-static approximation.** The electric field is assumed to be constant over an inclusion in the mixed material. This means the phase of a wave is approximately the same over the size of an inclusion. This approximation is only valid for inclusions that are small compared to the wavelength. If this is not the case, models including retardation effects must be applied.

- **Size independent dielectric function.** The dielectric functions of the mixed materials was assumed to be independent of the size of the inclusions, making the effective medium equations independent on absolute scale. This assumption is problematic for small inclusions, by a reduction of the mean-free path of free electrons and from quantization effects. Especially important for metals when the size of the structure is smaller than the mean-free path of the electrons. May be solved by using a size dependent dielectric function. [46, 47]

- **Negligible contributions from the near-fields** ($\boldsymbol{E}_{\text{near}} = 0$). Interactions between the inclusions are only included by the average fields. $\boldsymbol{E}_{\text{near}}$ might be important for low symmetry organizations [47, 48].

- **"Infinite" 3-dimensional material is assumed** For a 2-dimensional case, like particles on a flat substrate, boundary effects might become important. Interactions between particles and the substrate can give effective anisotropic (uniaxial) optical properties for particles with isotropic shape, like spheres. Such extensions of the Maxwell-Garnett equation have been made by Yamaguchi *et al.* [48]. Granqvist and Hunderi introduced effective depolarization factors to account for substrate and near-field interactions [47].

Chapter 3

Formation of GaSb nanostructures by ion sputtering

3.1 Pattern formation by ion sputtering

Sputtering is the bombardement of a surface with an ion beam, leading to ejection of atoms from the surface material. As an example of nanostructuration, we have studied low energy ion sputtering of gallium antimonide (GaSb), leading to the formation of high aspect ratio pillars on the surface. As opposed to a randomly rough surface, which has random height fluctuations with some correlation length and probability distribution for the height, sputtering of GaSb leads to nanopillars with about the same size and shape. The nanopillars can be randomly distributed on the surface, or in some special cases exhibit hexagonal ordering.

During sputtering of a surface, collisions between the bombarding ions and the atoms in the surface will tear out atoms. These atoms can be deposited on a different surface to create coatings and thin films [49]. This technique is referred to as sputter deposition. Sputtering is also used to clean surfaces of contaminations [50], remove oxide layers and reduce roughness [51]. However, in some cases sputtering may increase the surface roughness due to a surface instability. This was first observed by Navez *et al.* [52] in 1962, who found that low energy Argon ion sputtering of glass at oblique incidence leads to the formation of regular ripples with an amplitude of about 1 nm and a wavelength of less than 100 nm. Ripples formed by ion sputtering have later been observed on several different metals and semiconductors (see *e.g.* Ref. [53, 54]). Possible applications of such ripple patterns are as magnetic thin films [55], and templates for microelectronics and aligned nanoparticles [56]. On compound semiconductors dense dot patterns have been formed on GaSb [19] and InP [20] by ion sputtering at normal ion incidence. These dot patterns can, depending on formation conditions, exhibit

hexagonal ordering, which is promising for quantum dot applications, or have a shape with high aspect ratio [28], which is promising for *e.g.* anti-reflective coating applications.

The formation of nanostructures by ion sputtering has the advantage of being a so-called "bottom-up" or self-assembled process, which allows structuring of large surfaces relatively fast in a one step process. Structures with a wide range of sizes can be made by adjusting the sputtering conditions. For sputtering of GaSb, variations in size of over an order of magnitude can be achieved, from small dots with a height of 10-20 nm, to high aspect ratio pillars more than 300 nm tall. Figure 3.1 presents some examples of AFM images of GaSb surfaces sputtered with different ion energy, all with normal ion beam incidence. The nanopillars point in the direction towards the incoming ions. Sputtering with an oblique ion incidence leads to inclined nanopillars. The inclination angle can be accurately controlled by controlling the angle of ion incidence. Figure 3.2 shows SEM images of GaSb nanopillars sputtered with various angles of ion incidence. A good understanding of the connection between the nanostructures' shape and size and the sputtering conditions; such as ion energy, flux and temperature, can allow tailoring of the properties of the nanostructures.

The formation of dots and pillars on compound semiconductors has been given different explanations in the literature. In the initial reports, the formation of GaSb nanostructures by sputtering was attributed to the same mechanisms as for the formation of ripples [19]. Ripple formation is explained by the Bradley–Harper model, in which the structures are formed by a competition between curvature dependent sputtering yield and diffusion [57]. However, this model can not explain the observation of high aspect ratio pillars, or the formation of inclined nanopillars for sputtering with oblique ion incidence. From the observation of Ga enrichment in the top of the nanopillars, a new explanation has been proposed, where the formation has been ascribed to a masking effect of Ga and surface segregation [28].

Real-time observations of the formation of GaSb nanopillars can help provide a deeper understanding of why such structures are formed. The mechanisms responsible for the formation of GaSb nanopillars are also expected to be valid for the formation of nanostructures by sputtering on other compound semiconductors. By understanding the formation on compound semiconductors, predictions may be made of new materials that will form nanostructures during ion bombardment [58].

3.1.1 Sputtering theory

During ion bombardment of a surface, the incoming ions will lose their energy in collisions with the atoms in the surface. The incoming ions cause a cascade of collisions, which sometimes lead to a recoiling atom leaving the surface. In addition to the ejected atoms, the ion beam also leads to material defects and

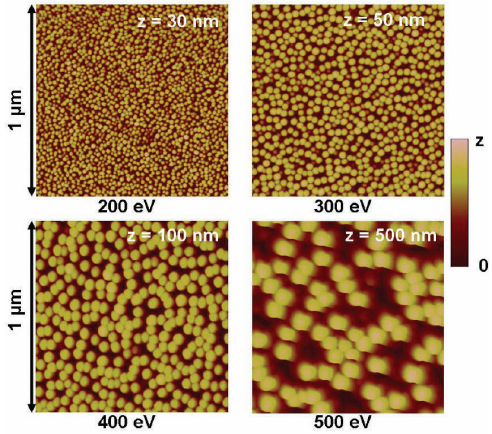

Figure 3.1: AFM images of GaSb nanopillars prepared by sputtering with different ion energy. Figure taken from [58]

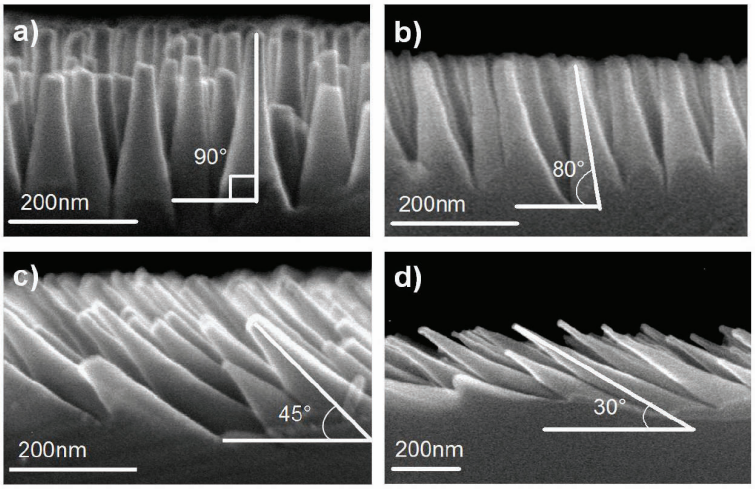

Figure 3.2: SEM crossection images of GaSb nanopillars sputtered with various angles of ion incidence. Figure taken from [58].

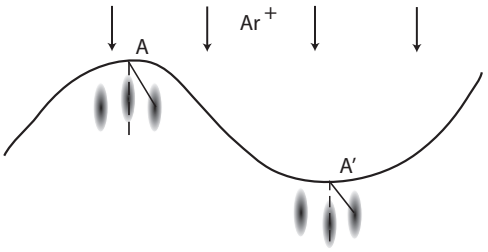

Figure 3.3: Illustration of how Sigmund's sputtering theory leads to a curvature dependent sputtering yield, which is the formation mechanism in the Bradley–Harper model. The energy received at a ridge (A) is smaller than at the bottom (A').

heating of the material. As a consequence, sputtering of crystalline GaSb quickly leads to the formation of an amorphous overlayer.

The average number of atoms leaving the surface per incoming ion is called the sputtering yield. The sputtering yield can have local variations over a surface, caused by varying topography, composition, crystal structure, and defects [53]. The variations in yield can cause a surface instability, leading to formation of surface structures. In the Bradley–Harper model, the instability is caused by a curvature dependent sputtering yield. This is explained by applying Sigmund's sputtering theory [59] to approximate how the energy of of an incoming ion on average is imparted to the sputtered material. The interaction between the ions and the bombarded material is a stochastic process. On average it is approximated that the energy deposited from the ions has a maximum at some point below the surface, and that deposited energy decay as a Gaussian function away from this point. This Gaussian is characterized by three parameters, the depth of the energy center where the most energy is deposited, and two parameters defining the width of the Gaussian function, parallel and orthogonal to the incident direction. The width of the Gaussian is wider along the incident direction. For a curved surface, this theory leads to more energy being deposited close to the surface on areas with positive curvature (bottom of a ripple) than at areas with negative curvature (top of a ripple), see figure 3.3. This gives a surface instability, that will amplify any initial deviations from a flat surface during ion bombardment. The instability is opposed by diffusion, which leads to smoothing of the surface. In the Bradley-Harper model the surface is described by a continuous height function h. The time evolution of h during sputtering follows a linear differential equation,

$$\frac{\partial h}{\partial t} = -\upsilon_0 + \gamma \frac{\partial h}{\partial x} + \upsilon_x \frac{\partial^2 h}{\partial x^2} + \upsilon_y \frac{\partial^2 h}{\partial y^2} - B\left(\frac{\partial^4 h}{\partial x^4} + \frac{\partial^4 h}{\partial y^4}\right). \tag{3.1}$$

υ_0 is the rate of erosion for an unperturbed planar surface, υ_x and υ_y are the effective surface tensions generated by the sputtering, γ is the lateral ripple motion, and B is the surface diffusion coefficient.

Extensions of the Bradley-Harper model have been made to explain the formation of dot patterns for sputtering at normal incidence and for oblique incidence with sample rotation. Non-linear extensions can explain observed features such as amplitude saturation and hexagonal ordering [60, 61]. Shenoy *et al.*[62] extended the Bradley–Harper model to include composition variations for ripple formation on alloys, and recently Bradley and Shipman [63] extended this theory to describe the formation of dots with short range hexagonal ordering on compound materials. This model can explain the dot patterns observed by Facsko *et al.* [19] and others, but it can not explain the nanopillars formed with the experimental conditions described in this work. Models based on a curvature dependent sputtering yield can not explain the formation of inclined pillars by sputtering at oblique ion incidence, or the formation of high aspect ratio pillars. Based on examinations of the composition of GaSb nanopillars, Le Roy *et al.* [28] proposed the formation to be caused by phase segregation and preferential sputtering, and named the process self-sustained etch masking.

3.1.2 Self-sustained etch masking

During sputtering of GaSb, there will be an enrichment of Ga in the surface, as Sb has a slightly higher sputtering yield than Ga [64]. Due to the specific phase diagram of GaSb, the excess Ga will segregate into Ga droplets. As the Ga is more resistant to ion erosion, the droplets will partially shield the surface, initiating the formation of GaSb nanopillars. This process is similar to how patterns are normally transferred trough standard lithography and etching. The Ga in the droplets is sputtered away more slowly than the GaSb in the surrounding area. As Sb is preferentially sputtered away, the areas between the Ga droplets will be enriched in Ga. This Ga will diffuse toward the droplets and continuously resupply them with Ga, thereby the name self-sustained etch masking. This resupply explains why high aspect ratio pillars can be formed. Ga shielding can also explain the formation of inclined nanopillars for sputtering with oblique ion incidence.

To simulate the formation of GaSb nanopillars based on self-sustained etch masking, Le Roy *et al.* formulated a diffuse-interface model based on only a small number of ingredients, namely, (i) a difference in sputtering yield between the two species, (ii) phase segregation of Ga, consistent with the equilibrium phase diagram, and (iii) diffusion of matter in the amorphous layer created by the ion impact (see **Related paper 1**). In a diffuse-interface model, surfaces are represented as smooth profiles of a scalar quantity, in this case density, with a small but finite width. Such a model can describe inclined pillars, which have overhangs

that can not be described by a height function h as used in the Bradley–Harper model. The results of such simulations are compared to real-time ellipsometry observations in **Related paper 1**.

Chapter 4

Optical modeling

A large number of different approaches exist for modeling the optical properties of heterogeneous materials, and the necessary complexity depends on the mixed materials dimension and type. GaSb nanopillars prepared by sputtering can have a wide range of sizes. The smaller pillars fall well within the range of effective medium models, while the larger are too large for effective medium models, but still too small to give any significant scattering or diffraction effects. Diffraction may be suppressed by the random distribution of pillars, scattering can be hard to observe due to light trapping effects from the graded pillar shape. From the early mixing rules such as Maxwell-Garnett, Lorentz-Lorenz and Bruggeman, more advanced models have been developed, as described in section 2.3.4 and 4.1.3. However, these more advanced models often have a high number of parameters, which makes them suitable for forward calculations of the optical properties of some well known structure, but less useful for the characterization of unknown structures.

The purpose of this work was to learn more about the formation of nanostructures on compound semiconductors by real-time ellipsometry measurements. Therefore, the study was mainly focused on experimental conditions resulting in structures small enough to be treated by a relatively simple effective medium model. From extensive *ex-situ* spectroscopic ellipsometry and Mueller matrix ellipsometry of GaSb nanopillars, in combination with complementary studies by AFM, SEM and TEM, an effective medium model depending on only a few parameters could be developed (**Paper I**). The parameters of this model can then be fitted to real-time ellipsometry measurements of the pillars during sputtering (**Paper II**). Real-time Mueller matrix measurements of pillars formed at experimental conditions leading to larger nanopillars are presented in **Paper V**.

4.1 Effective medium modeling in ellipsometry

Effective medium models have been much used to model ellipsometry measurements of heterogeneous and rough materials. Before the development of spectroscopic ellipsometry, the Lorentz-Lorenz equation (equation (2.22)) was widely used to model single wavelength ellipsometry measurements of rough surfaces [65]. With the advent of fast, automatic, spectroscopic ellipsometers, the validity of effective medium representations of rough surfaces could be better assessed, and Aspnes *et al.* found the Bruggeman equation (equation (2.24)) to best represent a rough amorphous Si surface [65]. Several studies also report real-time ellipsometry measurements on rough surfaces in combination with effective medium modeling. Examples of single wavelength studies are presented by Theeten and Hottier who studied surfaces during vapour phase growth [11], Pal *et al.* reported studies of surface roughness development on photoresist materials during plasma processing [13], and Akazawa studied the evolution of nanometer-scale Ge islands and pits in Ge homoepitaxy [66]. Multichannel spectroscopic real-time studies have also been performed on *e.g.* rough amorphous Si [12].

Other examples of heterogeneous materials that have been characterized by spectroscopic ellipsometry in conjunction with effective medium modeling are *e.g.* the study of Au clusters deposited on silica surfaces [67], and porous silicon [68]. Post-deposition nano-structural changes in silver island films have been determined from real-time spectroscopic ellipsometry by use of a Maxwell-Garnett effective medium model [15].

Columnar nanostructures can exhibit shape induced anisotropies. Hodgkinson and Wu [29] described such structures by Bragg-Pippards [69] anisotropic effective medium equation. Uniaxially anisotropic effective medium models have been applied to model column like heterogeneous materials, like ultraporous silicon prepared by vacuume evaporation [70], porous aluminum oxide [71, 72]. In these reports the columns were aligned normal to the substrate, resulting in an effective dielectric function with the optic axis normal to the substrate. In this case there is no polarization coupling, and the samples can be characterized by *standard* ellipsometry. The anisotropic Bruggeman effective medium equation (equation (2.26)) was applied with the the depolarization factors $L_{x,y} = 1/2$ and $L_z = 0$.

The anisotropic Bruggeman model has also been applied to model inclined columnar materials by Euler rotations of the effective dielectric tensor in the principal coordinate system. In that case *generalized* ellipsometry at several azimuth sample orientations are necessary to characterize the optical properties. By such studies the inclination angle of oblique silicon nanocolumns have been found [73], and oblique MgF_2 columnar thin films was characterized [74]. Cobalt nanoparticles with ellipsoidal shapes buried in silica have been characterized by generalized ellipsometry and modeled by an anisotropic Maxwell-Garnett formula [75], re-

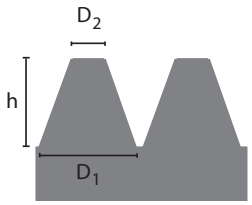

Figure 4.1: Sketch of the model representing the Gasb pillars prepared by normal incidence sputtering. D_1 and D_2 are the effective diameters of the bottom and top cylinder, and h is the pillar height.

sulting in information on layer thickness, volume fraction, orientation, and shape factor of the nanoparticles. A different approach, not relying on effective medium equations, was applied by Schmidt *et al.*, who used *generalized* ellipsometry to characterize the optical properties of inclined metal (Cr,Co and Ti) columnar thin films [76, 77, 78]. The pillar orientation, inclination and height were determined by modeling the structure as an anisotropic (monoclinic) homogeneous layer with a dielectric tensor obtained via a point-by-point fit. Similarly an effective dielectric tensor representing horizontal silver nanowire arrays was found from generalized ellipsometry [79] by fitting dispersion relations to the dielectric functions along the three principal directions.

4.1.1 GaSb nanopillar model

GaSb nanopillars prepared by low energy ion sputtering have a uniaxial symmetry, similar to the columnar nanostructures studied by Hodgkinson and Wu ,and others mentioned above. The conical shape of the pillars, as seen in figure 3.2, introduce a gradient in the refractive index, which for tall pillars lead to a strong anti-reflective effect. In analogy with earlier work on columnar nanostructures, the GaSb pillars are modelled as an anisotropic effective medium. Parallel to the pillar axis there will be no polarization screening, meaning that the depolarization factor $L_{||} = 0$. Normal to the pillar axis the depolarization factor for the two principal directions are equal to $L_{\perp} = 1/2$. In a two-dimensional effective medium model this corresponds to cylindrical inclusions distributed on a surface. To model the conical shape, the pillars are represented by a stack of cylinders with decreasing diameter. A sketch of the effective medium model representing pillars prepared by normal ion incidence is presented in figure 4.1. Each cylinder in the stack defines a uniaxal layer with the optic axis along the cylinder axis, with an effective dielectric tensor found from the generalized Bruggeman effective medium equation (equation

(2.26)). In the direction of the optic axis the effective dielectric function $\varepsilon_{||}$ can be found as the volume average of the dielectric functions of GaSb and void (one of the Wiener bounds, equation (2.27))

$$\varepsilon_{||} = f_{\mathrm{GaSb}}\varepsilon_{\mathrm{GaSb}} + f_{\mathrm{v}}\varepsilon_{\mathrm{v}}. \tag{4.1}$$

Here f and ε denote the filling factors and complex dielectric functions, respectively. The subscript GaSb refer to the crystalline core, and v to the surrounding void. The dielectric function of GaSb was taken from reference [80], data from reference [81] was used for measurements at high temperatures. Normal to the optic axis the effective dielectric function $\varepsilon_{\perp}$ is given by equation (2.26) with $L_{\perp} = 1/2$,

$$f_{\mathrm{GaSb}}\frac{\varepsilon_{\mathrm{GaSb}} - \varepsilon_{\perp}}{\varepsilon_{\perp} + \varepsilon_{\mathrm{GaSb}}} + f_{\mathrm{v}}\frac{\varepsilon_{\mathrm{v}} - \varepsilon_{\perp}}{\varepsilon_{\perp} + \varepsilon_{\mathrm{v}}} = 0. \tag{4.2}$$

A stack of $N = 50$ layers is used to model the gradient. The diameter, $d(n)$, of the cylinders in layer n is set to vary linearly from the bottom diameter D_1 to the top diameter D_2,

$$d(n) = D_1 - (n-1)\frac{D_1 - D_2}{N-1}, \quad n = 1..N. \tag{4.3}$$

On average the GaSb pillars have 6 nearest neighbors [**Paper I**], hence the filling factors have been calculated for a hexagonal lattice,

$$f_{GaSb}(n) = \frac{\pi}{\sqrt{12}}\, d^2(n). \tag{4.4}$$

The bottom and top diameters D_1 and D_2 are normalized to the center to center nearest neighbor distance, since only the volume filling factors influence the effective medium. This means that D_1 and D_2 will have values between 0 and 1, where 1 correspond to a close packed hexagonal lattice. Consequently the lateral size of the pillars can not be found from ellipsometry measurements when the effective medium approximation is valid. The lateral size have therefore been found by *ex situ* AFM or SEM imaging of the final structures only.

Inclined pillars

Pillars formed by sputtering with oblique ion incidence will point toward the incoming ions. The optic axis will therefore be inclined by an angle θ from the substrate normal equal to the angle of ion incidence. This is included in the model by an Euler rotation of the principal effective dielectric tensor by an angle θ from the substrate normal, and an azimuth rotation ϕ depending on the sample orientation during the measurement.

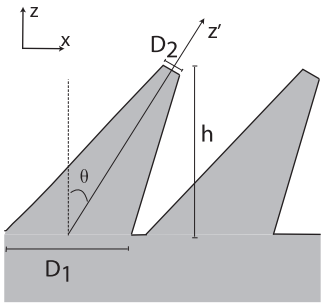

Figure 4.2: Sketch of optical model of the inclined GaSb nanopillars, pointing along the direction z' at an angle θ relative to the substrate normal.

The reflection coefficients for a stack of anisotropic layers can be calculated by using Berreman's 4×4 differential matrices (section 2.2). The effective parameters can then be found from the ellipsometry measurement by minimizing a figure of merit function χ^2, given as

$$\chi^2 = \frac{1}{N \cdot J - P + 1} \sum_{i=1}^{N} \sum_{j=1}^{J} \left(\frac{m_j^{\mathrm{mod}}(i) - m_j^{\mathrm{exp}}(i)}{\sigma_j(i)} \right)^2, \tag{4.5}$$

where N is the number of points in the spectrum, J is the number of Mueller elements used in the fit, P is the number of free parameters in the model, m_j^{mod} and m_j^{exp} are the simulated and measured Mueller elements normalized with the total reflectivity (M_{11}), and σ_j is the standard deviation of the measurement.

4.1.2 Limitations

The anisotropic graded effective medium model described above allows characterizing GaSb nanopillars by spectroscopic ellipsometry and Muller matrix ellipsometry. By fitting the model to measurements one can derive the mean pillar height, volume filling factors and gradient (D_1 and D_2) [**Paper I**], and for inclined pillars one can in addition find the inclination angle and pillar orientation [**Paper III**]. A limitation of this method is that one can not find the lateral size of the structures, like nearest neighbor distance and absolute pillar diameter. This is inherent from the validity of the effective medium model. The effective medium equations does not depend on the absolute scale.

The effective medium model is only valid for structures that are sufficiently smaller than than the wavelength of light. Especially the lateral scale should be much smaller than the wavelength of light. The model can be considered as

two dimensional, giving an effective dielectric function of an effective layer that is independent of the thickness of the layer . Retardation effects due to the layer thickness are included through the transfer matrix method to calculate reflections from anisotropic layers. The conical shape of the pillars is included by a gradient in the volume filling fraction of the effective medium along the direction of the substrate normal. This should mean that it is the lateral size of the pillars that limits the validity of the effective medium model. For inclined pillars this might not be the case. For GaSb nanopillars the lateral size usually is larger for higher pillars. This means that one can observe a failure of the optical model for a certain pillar height, which could be caused by an increased lateral size that can not be observed directly from the optical measurements.

4.1.3 Different optical models

This section gives a short summary of some other approaches to model the optical properties of nanostructures.

Thin island film

Bedeaux and Vlieger [82] developed the so called thin island film theory, where a thin discontinuous film or a rough surface is represented by a infinitesimally thin polarizable dipole layer. The model takes into account both interactions with image charges and lateral neighbor interactions. Like the effective medium theories it is based on the quasi-static approximation, an is only valid for layers that are thin compared to the wavelength of light. This theory has been applied to model ellipsometry measurements on Au nanocolloids to determine the surface coverage [83, 84].

Diffraction based methods

For structures with a size comparable to the wavelength of light, retardation effects becomes important, and the quasi-static approximation no longer holds. Such structures may lead to scattering and diffraction of light. Rigorous coupled wave analysis (RCWA) is a much used technique for calculations on diffraction gratings. It is a rigorous method to calculate the optical properties of periodic structures [85], but it is very computationally demanding for three-dimensional non-periodic structures. A more computationally efficient finite-element Green's function approach was developed by Chang *et al.* [86]. Both the finite-element Green's function and RCWA has been applied to model Si nanorods with diameters ranging $30 - 45$ nm and heights between $200 - 315$ nm by Hsu *et al.* [87].

For low amplitude scattering surfaces, the Rayleigh–Rice perturbation approach can be applied. Such an approach was *e.g.* used to model the optical properties of low amplitude Ag ripples prepared by grazing incidence sputtering [88]. However, the Rayleigh–Rice theory should not be applicable to model the large GaSb nanopillars, due to their high aspect ratio.

Other homogenization approaches

In section 2.3 the most widely applied effective medium equations were introduced, and their generalizations for anisotropic inclusions were described. It was also mentioned that more advanced models have been developed by Yamaguchi *et al.* [48] and Granqvist and Hunderi [47] to include interactions with the substrate and neighboring inclusions. Bergman formulated an approach to calculate the effective dielectric function of a general composite material of any geometrical shape [89]. Numerous other examples exist in the literature, to *e.g.* model materials consisting of a mix of inclusions with different shape or materials with coated inclusions *etc.*.

A different approach, not relying on mixing rules, is to find an effective dielectric function representing the structure by a point-by-point fit, or by fitting a dispersion relation, to ellipsometry measurements of the nanostructures. This should be valid for all materials with negligible scattering and diffraction effects. Examples of this approach to model the optical properties of anisotropic nanostructures are reported in references [76, 79]. Compared to the effective medium equation, this approach gives no information on volume filling factors, but the thickness of the effective layer and the orientation of its principal axes have been reported.

Chapter 5

Experimental setup

In this section I will briefly explain the principles of the the different ellipsometers used to study the GaSb nanopillars, both *in situ* and *ex situ*. A description will also be given of the sputtering chamber and ion gun that was used to prepare the samples. This has not been treated in detail in the published papers. Direct nanoscale imaging tools used for *ex situ* characterization will also be described, such as atomic force microscopy and scanning electron microscopy.

5.1 Ellipsometry

Ellipsometers based on several different technologies are commercially available or described in the literature. All apply some kind of polarization modulating components either before, after, or at both sides of the sample. The polarization modulation can be achieved by *e.g.* rotating polarizers or compensators, electro-optic crystals, photoelastic modulators and liquid crystals.

5.1.1 Mueller ellipsometry based on ferroelectric liquid crystals

The *in situ* measurements were performed with a ferroelectric liquid crystal (FLC) based Mueller matrix ellipsometer (MM16, *Horiba Jobin Yvon*), applying a multichannel spectrograph based on a charged coupled device (CCD) array detector. The instrument is capable of measuring the Mueller matrix in the spectral range of $430-850$ nm ($1.44-2.88$ eV), with a measurement time down to 3 s. To measure the Mueller matrix, 4 different polarization states are generated by a polarization state genetrator (PSG). The resulting polarization state of the light after a reflection from a sample is then measured by a polarization state analyzer (PSA). The PSA measures the Stokes vector of the reflected light by performing 4 measure-

ments for each generated state, meaning at least 16 intensity measurements must be made to measure the Mueller matrix. The 4 states generated by the PSG are designed to be as orthogonal as possible over the full spectral range, which means that their Stokes vectors span out all polarization states as good as possible. The same is the case for the 4 projection states of the PSA.

The polarization modulation in the PSA and PSG is achieved by two FLCs. The first Mueller matrix polarimeter based on FLCs was reported by Garcia-Caurel *et al.* [90]. Previously FLCs had been reported used in a Stokes polarimeter by Gandorfer [91]. A Stokes polarimeter can measure the Stokes vector of light, and consists only of a PSA. A FLC works as a phase retarder that can be electronically switched between two states. The difference between the states corresponds to a rotation of the fast axis by 45°. By using a linear polarizer and two FLCs as a PSG (PSA), one can generate $2^2 = 4$ different polarization (projection) states. The instrument derives the Mueller matrix from 16 discrete intensity measurements, which can be gathered into a matrix, **B**. This matrix is connected to a measured Mueller matrix, **M**, as

$$\mathbf{B} = \mathbf{AMW}. \tag{5.1}$$

A and **W** are 4×4 system matrices of the PSA and PSG, respectively. The matrix **W** contains the generated Stokes vectors as its columns. These can be found as the first columns of the Mueller matrices of the PSG in the respective state. In a similar fashion, the matrix **A** contains the projection states at its rows, found from the first rows of the Mueller matrices of the PSA for the given states. These system matrices are found by applying the eigenvalue calibration method [92], which allows measuring the actual produced states by the PSA and PSG (**A** and **W**), without relying on exact knowledge or modeling of the optical components. **M** can then be found by inversion as

$$\mathbf{M} = \mathbf{A}^{-1}\mathbf{B}\mathbf{W}^{-1}. \tag{5.2}$$

The noise amplification from **B** to **M** is proportional to the condition numbers of the matrices **A** and **W** [93].

As the retardance of the FLCs is wavelength dependent, the PSG and PSA can only produce the optimal states for a single wavelength. To have a broadband instrument, trade offs must be done to have as good as possible performance over a broad wavelength range. The spectral width of such an instrument will be limited by the PSG and PSA not being able to create orthogonal enough states, leading to an ill-conditioned equation system for deriving the Mueller matrix. Improvements of a FLC based polarimeter are discussed in **Paper VI**.

The measurement scheme of the FLC based ellipsometer is different from other ellipsometer technologies, which are usually based on continuous polarization modulation (*e.g.* by a rotating polarizer/compensator or a photoelastic modulator).

The ellipsometric parameters and Mueller elements are then derived from Fourier coefficients of the continuously varying intensity. A Mueller matrix ellipsometer based on two rotating compensators has been described by Collins *et al.* [94], based on achromatic compensators and multichannel detection over a broad spectral range ($1.5 - 6.5$ eV). In comparison, liquid crystal based ellipsometers are limited to the visible and infrared spectral range as the crystals degrade in ultraviolet (UV) light. A dual rotating compensator ellipsometer has now also become commercially available (RC2, *J.A. Wollam Co., Inc.*), but it is more expensive than the MM16, and was not available at the start of this project.

The absolute uncertainty in the normalized Mueller matrix elements measured by MM16 is less than 0.01. For measurements of air the accuracy of the ellipsometric parameters are reported to be $\Psi = 45^\circ \pm 0.05^\circ, \Delta = 0^\circ \pm 0.2^\circ$ [95]. The uncertainty in Ψ and Δ measured on an isotropic sample is slightly larger for the MM16 than what can be achieved with standard monochromator based spectroscopic ellipsometers (based on rotating elements or photoelastic modulators). The increased uncertainty could be caused by the discrete measurements being more prone to noise, and from noise amplification in the inversion to find $\mathbf{M}$ (equation (5.2)). The CCD based spectrograph also gives less spectral resolution, but has the advantage of high speed allowing real-time spectroscopic measurements. As the full Mueller matrix is measured, real-time spectroscopic measurements can be performed on anisotropic and depolarizing samples.

5.1.2 Phase modulated ellipsometry

A phase modulated spectroscopic ellipsometer (UVISEL, *Horiba Jobin Yvon*) was used for *ex situ* measurements (**Paper I**) over a broad photon energy range ($1.5 - 6.5$ eV) of GaSb nanopillars prepared by normal ion incidence sputtering. The instrument uses a photoelastic modulator (on the input side) to continuously modulate the polarization at a high frequency (50 kHz), without mechanical movement. A photoelastic modulator consists of a bar of an optically transparent crystal (*e.g.* fused Silica for the UV-visible range) exposed to periodical stress from a piezoelectric transducer [96]. The stress induces an anisotropy in the crystal, by altering the dielectric function in the direction parallel to the stress. For light propagating through the crystals, this leads to a phase shift between modes with orthogonal field components (retardance).

For the UVISEL ellipsometer, the light passes through a polarizer and the photoelastic modulator on the input side. After reflection from a sample, the light pass through another polarizer, often denoted the analyzer, before entering the detector. Measurements can be performed with different configurations of the optical components. These are denoted by the orientation of the modulator, M, and the orientation of the polarizer, P, relative to the plane of incidence. In stan-

dard configuration (M=0°, P=45°) for isotropic samples the measured intensities are [96],

$$\begin{aligned} I_S &= \sin 2\Psi \sin \Delta \\ I_C &= \sin 2\Psi \cos \Delta. \end{aligned}$$

In the configuration M= 45°, P=45° one can measure,

$$I_{C'} = \cos 2\Psi.$$

In case the sample is anisotropic and leads to polarization coupling, these intensities will depend on several of the Mueller elements. One can then do generalized ellipsometry with the phase modulated ellipsometer by performing measurements at several combinations of different modulator and polarizer orientations, see *e.g.* reference [97].

5.1.3 Angle resolved Mueller polarimeter

Ex situ measurements of samples sputtered with oblique ion incidence and samples with very large nanopillars were performed with an angle resolved Mueller polarimeter (*custom built at Ecole Polytechnique*). These measurements are reported in **Paper III** and **Paper V**. The instrument applied a high numerical aperture (NA=0.95) microscope objective in a double pass configuration with its back focal plane imaged on a CCD camera, allowing simultaneous measurements of reflected light at all azimuth angles and all angles of incidence below 62° [98, 99, 100]. The light source was a lamp with various filters (532 nm and 633 nm). The PSA and PSG of the polarimeter both consisted of a pair of variable retardance nematic liquid crystals, and the polarimeter is based on a similar measurement scheme as the FLC based Mueller ellipsometer described in section 5.1.1.

5.2 Sputtering chamber

The GaSb nanopillars were produced by sputtering GaSb wafers with Argon ions in a dedicated ultra high vacuum (UHV) chamber, located at CNRS/Saint Gobain, Aubervilliers, France. A sketch of the chamber is presented in figure 5.1. The UHV chamber has an airlock with independent vacuum pumping systems, allowing to introduce samples without breaking vacuum in the main chamber. Samples are transfered from the airlock to the sample holder in the main chamber by a transfer manipulator. The sample holder is fixed to a manipulator in the main chamber that can translate the sample in and out, and rotate around the manipulator axis. This rotation is used to control the angle of incidence of the ions impinging on

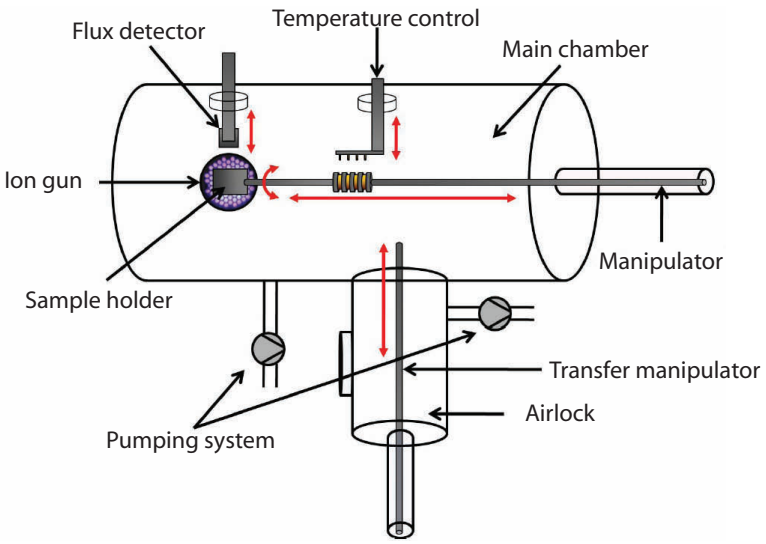

Figure 5.1: Sketch of vacuum chamber used for sputtering of GaSb. Figure adapted from [58].

the the surface from the ion gun. A retractable flux detector can be moved into the ion beam to measure the ion flux, but not simultaneous to the sputtering of a sample. A temperature control unit can heat the sample up to a temperature of 450° C, and measure the temperature at the backside of the sample through a thermocouple in the sample holder. The sample is not cooled during sputtering, and the temperature at the back of the sample can increase from room temperature and reach up to 80° C at the end of the experiment.

The pumping system maintains a base pressure in the main chamber of about $5 \cdot 10^{-9}$ mbar. During sputtering a continuous flow of Argon gas is introduced into the chamber through the ion gun, increasing the pressure to between $1 - 6 \cdot 10^{-4}$ mbar.

5.2.1 Ion gun

The ion gun used in the experiments to create the ion beam was a *Tectra Gen2 Plasma Source* [101], based on a microwave electron cyclotron resonance. Argon gas is introduced into an aluminum plasma cup, where it is ionized by a microwave oscillating with a frequency of 2.45 GHz. A voltage difference between a metal grid (at ground) at the opening of the cup and the cup itself (at positive bias) separates the electrons from the ions. The accelerated electrons collide with atoms in the

gas, ionizing it further. The ionization is increased by a static quadruple magnetic field, forcing the electrons to move in elliptical orbits and increasing their path length in the plasma. The magnets are designed such that a moving electron will have an electron cyclotron resonance at the applied microwave frequency [102]. Argon ions are extracted from the plasma by a system of two grids with a voltage difference accelerating the ions. This voltage difference gives the energy of the ions in the ion beam. Voltages between 200 and 500 V was used in this work, leading to ion energies ranging from 200 to 500 eV. The flux of the ion beam, defined as the number of incident ions per second per unit area, depends on the density of the plasma. This density depends on the Argon pressure and the intensity of the microwave source, which is generated by a current between 10 and 25 mA in our experiments. This results in an ion flux in the range 0.12 to 0.3 mA/cm^2. The flux is not only given by the current to the microwave source, it is also coupled to the acceleration voltage. This coupling means that not all combinations of flux and energy can be achieved with a stable ion beam.

Flux measurements

The flux of the ion beam, defined as the number of ions passing through a unit area per unit time, is measured by a custom built detector. It is based on a 1 cm^2 metal plate connected to ground. The metal plate is fixed on a ceramic support at the end of a rod that can translate the metal plate in and out of the ion beam. When the metal plate is placed in the ion beam it will accumulate charge, leading to a current. The flux can simply be measured by measuring this current, expressed in mA/cm^2.

Substrates

The samples sputtered were commercially available undoped crystalline (100) GaSb wafers [103]. The samples were polished, with an initial roughness of less than 0.5 nm [58], and had a thickness of 0.45 mm. The wafers were cut into pieces off approximately 1×1 cm, and mounted on a molybdenum sample holder and fixed by platinum springs.

In situ mounting of the ellipsometer

The MM16 Mueller matrix ellipsometer was mounted on the sputtering chamber by two strain free optical windows (*Horiba Jobin Yvon*), allowing real-time *in situ* measurements of the GaSb samples during sputtering. A sketch of the *in situ* set up is presented in figure 5.2. The viewports of the UHV chamber allowed optical access to the sample with an angle of incidence of 45° for sputtering with normal ion incidence (see left part of figure 5.2). By rotating the sample 22.5° and moving

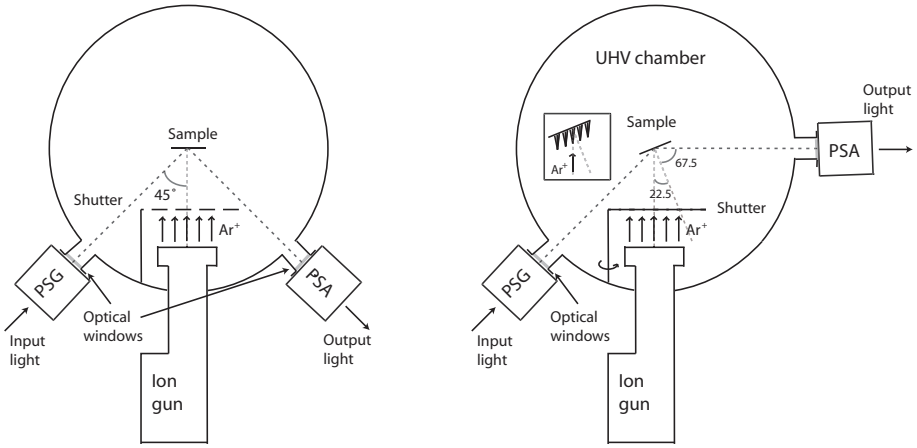

Figure 5.2: Sketch of the experimental setup used for the *in situ* ellipsometry measurements of GaSb during low energy ion sputtering. The input head (PSG) and output head (PSA) of the ellipsometer are mounted on the vacuum chamber by two strain free optical windows. Two different configurations were used. The left figure shows sputtering at normal ion incidence, with an optical angle of incidence of 45° for the ellipsometry. The formation of oblique pillars can be observed by rotating the sample holder by 22.5°, and moving the output head to a different viewport (right figure).

the output head (PSA) of the ellipsometer to a different viewport, sputtering with oblique ion incidence could also be observed, with an angle of incidence of 67.5° (see right part of figure 5.2). For the oblique sputtering, the incoming ion beam will be parallel to the optical plane of incidence. As the GaSb nanopillars will point toward the incoming ion beam, they will lie in the plane of incidence, pointing towards the incoming light. As earlier discussed, if the nanopillars can be modeled as a uniaxial material with the optic axis parallel to the pillars axis, there will be no polarization coupling for either of these configurations. In that case, it is not necessary to measure the Mueller matrix, *standard* ellipsometry would be sufficient. However, performing Mueller matrix measurements of such samples allows verifying that this actually is the case. The real-time results presented in **Paper II**, **Paper IV**, and **Related paper 1** are of small pillars exhibiting no polarization coupling. **Paper V** presents measurements of larger nanopillars, where measurements of the Mueller matrix is necessary for correct optical characterization.

The shortest measurement time possible with the applied ellipsometer was around 3 s. This limits the pillar formation rates that can be studied. For sputter-

ing with high ion energy and flux, the nanopillars can increase significantly in size during the measurement, leading to measurement errors. High nanopillars gives a reduced signal, due to their anti-reflective optical properties.

5.3 *Ex situ* microscopy characterization tools

A number of microscopy methods have been used for *ex situ* characterization of the GaSb nanopillars. This was necessary in order to develop an optical model and to control the results from the optical measurements.

5.3.1 Atomic force microscopy

Atomic force microscopy is based on scanning a very small tip (probe) across a surface and measuring its deflections [104]. It is one of the most widely used tools for imaging, measurements and manipulation on the nanoscale. The tip is fixed to a cantilever, which is deflected by atomic forces between the surface and the tip. These deflections are accurately measured by having a laser spot being reflected from the cantilever onto an array of photodetectors. The position of the tip can be moved very accurately and precisely by pizoelectric elements. The principles of AFM is very similar to those of a scanning tunneling microscope (STM), which scans a probe over a biased sample and creates an image of the surface from the tunneling current. As AFM applies atomic forces to form the image, it can be used on non-conducting samples and in ambient atmosphere.

An AFM can be operated in two different modes [105], contact (static) and tapping (dynamic) mode. In contact mode the tip is dragged across the surface and an image is created by measuring the deflection of the cantilever. This mode can lead to sample damage for soft samples, and tip damage. In this work tapping mode was used to image the GaSb nanopillars. In tapping mode the tip oscillates up and down near the cantilevers resonance frequency (around 300 kHz). As the tip moves closer to the surface the amplitude of the oscillation changes. By adjusting the average distance between the tip and the sample so that the oscillation amplitude is constant, a topographic image of the surface can be formed.

The disadvantage of AFM is a very slow scanning speed (several minutes), and the imaged area is very small. The tip that is scanned across the surface is very fragile, and for high aspect ratio structures it easily breaks, leading to a false image of the surface. Inclined pillars can not be properly imaged by AFM due to the overhanging structure.

Image analysis

Many studies have compared surface roughness measured by AFM and ellipsometry combined with effective medium modeling (see *e.g.* [106, 107]). When characterizing randomly rough surfaces a root mean square (RMS) amplitude is often used as a statistical measure of the thickness of the rough layer.

$$\mathrm{RMS} = \sqrt{\frac{1}{N}\sum_{1}^{N}(h(x,y)-\bar{h})^2}, \tag{5.3}$$

where N is the number of points, $h(x,y)$ is the surface height at a point with the coordinates (x,y) and $\bar{h}$ is the average of $h(x,y)$. How the RMS of a rough surface relate to the thickness of an effective medium layer found by spectroscopic ellipsometry is not so clear, and will vary from different types of rough surfaces. Fujiwara *et al.* found the height of a rough layer from spectroscopic ellipsometry (h_{SE}) to be related to the RMS found by AFM as $h_{SE} = 1.5 \cdot \mathrm{RMS} + 4\text{Å}$, for rough a-Si:H films [106]. Petrik *et al.* found different correlations between samples with different kinds of roughness on polysilicon [107].

In the case of the GaSb nanopillars, pillars with approximately the same shape are randomly distributed on the surface. The RMS value was not used to compare the AFM measurements to the height found from ellipsometry, instead the average height of all the pillars was calculated from the image. The height of a pillar was defined as the height of the top relative to a minimum within a certain distance (d) from the top. The mean height calculated this way increase strongly with d for distances shorter than the mean bottom pillar radius. Then it saturates, and the mean height found is then a good approximation to the real mean pillar height. This saturation distance corresponds well to half the mean nearest neighbor separation as estimated by AFM. Choosing a local minimum as a reference for the pillar height compensates for tip effects. As the tip has a finite size (around 10 nm) and angle, it will not always reach the bottom between two closely packed pillars. The local minimum will most likely be in a direction with longer neighbor distance.

The average nearest neighbor size of the nanopillars was found by Voronoi diagrams [93]. A Voronoi diagram is made by dividing the surface into polygons containing one pillar. All the points in a polygon is closer to the given pillar than to any of other pillars. The number of neighbors a pillar has can then be found by counting the number of sides of its polygon, and the average distance between the neighboring pillars can be found.

AFM measurements were performed using the tapping mode of a Nanoscope IIIA instrument from Veeco. The Si cantilevers used for the observations had a radius of curvature less than 10 nm and a spring constant of 40 N/m (supplied

by *NanoAndMore*). Typical scan lengths were 1 to 4 μm with a resolution of 512 points per line.

5.3.2 Scanning electron microscopy

A scanning electron microscope (Zeiss Ultra 55) was used to characterize samples with large pillars , and samples with inclined pillars that could not be characterized by AFM. A SEM works by scanning a very narrow electron beam across the sample. Morphological or chemical information about the surface can then be found by various detectors. In this work only information from the secondary electrons was applied. The secondary electrons are ejected from the k-orbitals of the sample by inelastic scattering of the scanning electron beam. The amount of secondary electrons released from the surface depends on the angle of incidence of the incoming electron beam, which makes it possible to create an image of the sample with down to a few nanometers of resolution (see *e.g. [108]*).

To find the height of inclined pillars, the samples were cleaved along a crystallographic direction, and the cross-section was imaged. Normal view images were also acquired of samples with large pillars, to get information about the lateral size and possible ordering. Ordering can easily be observed from the power spectral density (PSD) of a an image, which is found by taking the absolute value of a 2D Fourier transform of the image.

5.4 Alternative methods

Other methods than those mentioned above that have been used to study the morphology evolution of nanostructures. *In situ* studies of sputtering of GaSb have been performed with grazing-incidence small-angle x-ray scattering (GISAXS) [109]. GISAXS allowed deriving the lateral size and the degree of ordering (correlation length) of the structure, but the heights were not reported [26, 27]. This makes the method complementary to *in situ* ellipsometry, which allows deriving the height but not the lateral size. The reported GISAXS study was not performed in real-time. Due to a long acquisition time the samples were sputtered and measured sequentially. The technique requires an intense and well-collimated x-ray beam, typically provided by a synchrotron.

Absolute reflectivity measurements can be applied for real-time measurements. Compared to ellipsometry, no polarizing optics is necessary, and shorter acquisition times may be achieved. The disadvantage is that only one parameter is measured, compared to two or more in ellipsometry. Measuring the absolute reflectivity can be preferable in some cases, such as measuring the thickness of thick films and for measurements of geometrically rough surfaces (which are rough on a scale

larger than the wavelength of light) [110]. The absolute reflectance is recorded by a Muller matrix ellipsometer (M_{11}), but usually not with same accuracy as the normalized Mueller elements due to *e.g.* source fluctuations. For sputtering of GaSb, deposition on the windows is an issue for absolute measurements.

Reflectance-difference(anisotropy) spectroscopy (RDS/RAS) have been widely applied for real-time studies of surface anisotropies of semiconductors [111] and nanostructured surfaces [112, 113, 114]. RAS is highly sensitive, but can only measure the anisotropic part of the optical properties. In comparison, Mueller matrix ellipsometry can measure the absolute dielectric function of an anisotropic material, not only the relative difference along the principal axes. RDS measurements of GaSb pillars are not useful for deriving the pillar height, but may provide information on anisotropic lateral ordering (see **Paper V**). RDS is performed at normal angle of incidence. This requires only one optical window, but is not compatible with sputtering at normal ion incidence.

Chapter 6

Summary and conclusions

The formation of GaSb nanopillars by low energy ion sputtering has been studied in real-time with spectroscopic ellipsometry and spectroscopic Mueller matrix ellipsometry. In **Paper I** an effective medium model was developed to represent the pillars, based on *ex situ* spectroscopic ellipsometry measurements, AFM, SEM, and TEM studies. Small pillars were found to be well modeled by a uniaxially anisotropic graded effective medium model, where the pillars are treated as a stack of cylinders with decreasing diameter. This model enabled deriving the pillar height from spectroscopic ellipsometry measurements, and this height was found to correspond well with the height found from the direct microscopic methods.

In **Paper III**, the effective medium model was extended to represent inclined GaSb nanopillars prepared by sputtering with oblique ion incidence, based on spectroscopic Mueller matrix measurements at several azimuth sample orientations. The pillar height, inclination, and orientation found from the optical measurements agreed well with the results from cross-section SEM images. For samples with nanopillars inclined by 45° or less, the height could be determined from spectroscopic Mueller matrix measurement at a single azimuth orientation, opening for real-time *in situ* observation of the formation. The nanopillars were also studied using a single wavelength angle resolved Mueller polarimeter, which could be used to determine height and inclination of the pillars, in addition to validating the optical model over a wide range of incident and azimuth angles.

In **Paper II**, it is demonstrated that real-time *in situ* spectroscopic ellipsometry can be used to measure the height evolution of nanostructures during low energy ion sputtering of GaSb. A series of of GaSb samples were exposed to an ion beam for various exposure times under the same experimental conditions, and the endpoints of the height evolutions were compared to *ex situ* AFM measurements of the final structure. The real-time observations revealed an interesting and surprising evolution of the GaSb nanostructures during sputtering. The formation could be divided into three regimes; first an initial stage with removal of oxide and

some delay, followed by a second regime with a rapid and steady increase of the pillar height, and finally the formation changes to a third regime with a slow and linear increase of the pillar height. The last regime was found to continue for up to an ion exposure time of 30 minutes without signs of saturation. The transition from the initial regime to the rapid regime was found to fit well to an exponential time dependence.

The three observed formation regimes of the GaSb nanopillars can not be explained by the Bradley–Harper model, which initially was proposed to explain the formation of GaSb nanostructures by ion sputtering. Instead Le Roy *et al.* formulated a phenomenological diffuse interface model to explain the formation, based on a process named self-sustained etch masking [28]. This model included three basic components; difference in sputtering yield between the two species, phase segregation of Ga, and diffusion of matter in the amorphous layer created by the ion impact. The formation rate simulated by such a model was compared to the height evolution found by real-time ellipsometry in **Related paper 1**, and it was able to reproduce the three formation regimes observed in **Paper II**. This result is in strong support of the self-sustained etch masking mechanism proposed to explain the formation of the pillars by Le Roy *et al.* in reference [28], rather than the Bradley–Harper mechanism.

The optical model developed in **Paper I** and **Paper III**, and verified *in situ* in **Paper II**, allows to study how the height evolution of GaSb nanopillars depends on experimental conditions, such as ion flux, energy, and temperature. This is done in an extensive and systematic real-time ellipsometry investigation presented in **Paper IV**, in combination with *ex situ* AFM and SEM studies. Both sputtering at normal ion incidence and 22.5° inclined ion incidence was studied. It was found that the ion flux determines the timescale of the formation, while the pillar length scale and late stage formation rate was controlled by the energy and the temperature. The lateral length scale of the patterns are mainly determined during the second of the three regimes observed in **Paper II**. These observations are discussed and explained on basis of the self-sustained etch masking mechanism and the earlier mentioned phenomenological diffuse interface model. The combined AFM and *in situ* ellipsometry study evidences that it is possible to select a lateral scale using an adequate energy or temperature in the first formation regime. Afterward, the height can be adjusted by tuning of the flux and the exposure time. This observation opens for enhanced control over the patterns obtained on GaSb.

In **Paper II** and **Paper IV**, only nanopillars with a height of less than 100 nm was studied. For larger structures, the uniaxial effective medium model was not able to represent the optical properties of the pillars. In **Paper V**, sputtering of GaSb with an ion energy leading to large nanopillars was monitored in real-time by Mueller matrix ellipsometry. For the first 3 minutes the optical properties

of the nanopillars were modeled by a graded uniaxial effective medium model. After 3 minutes, as the height of the pillars surpassed 100 nm, coupling between orthogonal polarization modes was observed from the measurements. From *ex situ* angle resolved Mueller matrix polarimetry of the final structure, this coupling was attributed to the pillars having effective biaxial optical properties, with one intrinsic axis normal to the substrate. Fourier analysis of a scanning electron microscope image of the final nanopillars showed that the lateral anisotropy can be attributed to a direction dependent nearest neighbor distance. Each individual pillar has a uniaxial symmetry, the biaxial symmetry comes from the anisotropic organization of the pillars.

All the *in situ* ellipsometry measurements were performed with a commercial Mueller matrix ellipsometer (MM16, *Horiba Jobin Yvon*), based on four ferroelectric liquid crystals as polarization modulating elements, two in the polarization state generator and two in the polarization state analyzer. The quality of the measurements of such a system depends on its ability to generate as orthogonal polarization and analyzation states as possible, to span out all possible states. Due to the dispersive properties of the optical elements, this is only achieved over a relatively narrow spectral range with the MM16, from $430-850$ nm. In **Paper VI** improved designs of such a system based on four or six ferroelectric liquid crystals are found by the use of a genetic algorithm. The results promise to reduce the measurement noise significantly compared to previous designs, up to a factor of 4.5 for a Mueller polarimeter, in addition to extending the spectral range to $430-2000$ nm.

Bibliography

[1] A. P. Alivisatos, "Semiconductor clusters, nanocrystals, and quantum dots," *Science* **271** (1996) no. 5251, pp. 933–937.

[2] A. Marti and N. Lopez and E. Antolin and E. Canovas and C. Stanley and C. Farmer and L. Cuadra and A. Luque, "Novel semiconductor solar cell structures: The quantum dot intermediate band solar cell," *Thin Solid Films* **511-512** (2006) 638 – 644.

[3] S. J. Wilson and M. C. Hutly *J. Mod. Opt.* **29** (1982) 993.

[4] Z. P. Yang, L. Ci, J. A. Bur, S. Y. Lin, and P. M. Ajayan, "Experimental observation of an extremely dark material made by a low-density nanotube array," *Nano Lett.* **8** (2008) no. 2, 446–451.

[5] S. A. M. Tofail, I. Z. Rahman, and M. A. Rahman, "Patterned nanostructured arrays for high-density magnetic recording," *Applied Organometallic Chemistry* **15** (2001) no. 5, 373–382.

[6] R. M. A. Azzam and N. M. Bashara, *Ellipsometry and Polarized Light.* NORTH-HOLLAND, 1987.

[7] H. G. Tompkins and E. A. Irene, *Handbook of Ellipsometry.* 2005.

[8] W. M. Duncan and S. A. Henck, "Insitu spectral ellipsometry for real-time measurement and control," *Appl. Surf. Sci.* **63** (1993) no. 1-4, 9 – 16.

[9] R. W. Collins, I. An, H. Fujiwara, J. Lee, Y. Lu, J. Koh, and P. I. Rovira, "Advances in multichannel spectroscopic ellipsometry," *Thin Solid Films* **313-314** (1998) 18 – 32.

[10] M. Kildemo, R. Brenot, and B. Drévillon, "Spectroellipsometric method for process monitoring semiconductor thin films and interfaces," *Appl. Opt.* **37** (1998) no. 22, 5145–5149.

[11] F. Hottier and J. B. Theeten, "Surface analysis during vapour phase growth," *Journal of Crystal Growth* **48** (1980) no. 4, 644 – 654.

[12] H. Fujiwara, J. Koh, P. I. Rovira, and R. W. Collins, "Assessment of effective-medium theories in the analysis of nucleation and microscopic surface roughness evolution for semiconductor thin films," *Phys. Rev. B* **61** (2000) no. 16, 10832–10844.

[13] A. R. Pal, R. L. Bruce, F. Weilnboeck, S. Engelmann, T. Lin, M.-S. Kuo, R. Phaneuf, and G. S. Oehrlein, "Real-time studies of surface roughness development and reticulation mechanism of advanced photoresist materials during plasma processing," *Journal of Applied Physics* **105** (2009) no. 1, 013311.

[14] T. W. H. Oates and A. Mucklich, "Evolution of plasmon resonances during plasma deposition of silver nanoparticles," *Nanotechnology* **16** (2005) no. 11, 2606–2611.

[15] T. W. H. Oates, L. Ryves, and M. M. M. Bilek, "Dynamic spectroscopic ellipsometry determination of nanostructural changes in plasmonic silver films.," *Optics express* **15** (2007) no. 24, 15987–98.

[16] S. A. Little, R. W. Collins, and S. Marsillac, "Analysis of interband, intraband, and plasmon polariton transitions in silver nanoparticle films via in situ real-time spectroscopic ellipsometry," *Applied Physics Letters* **98** (2011) no. 10, 101910.

[17] P. Wu, T. Kim, A. Brown, M. Losurdo, and G. Bruno, "Real-time plasmon resonance tuning of liquid Ga nanoparticles by in situ spectroscopic ellipsometry," *Appl. Phys.* (2007) 2007–2009.

[18] M. Losurdo, "Applications of ellipsometry in nanoscale science: Needs, status, achievements and future challenges," *Thin Solid Films* **519** (2011) no. 9, 2575–2583.

[19] S. Facsko, T. Dekorsy, C. Koerdt, C. Trappe, H. Kurz, A. Vogt, and H. L. Hartnagel, "Formation of Ordered Nanoscale Semiconductor Dots by Ion Sputtering," *Science* **285** (sept, 1999) 1551–1553.

[20] S. H. Y. Yuba and K. Gamo, "Nanostructure fabrication of InP by low energy ion beams," *Nucl. Instrum. Meth. B* **206** (2003) 648–652.

[21] F. Frost, B. Ziberi, T. Hoche, and B. Rauschenbach, "The shape and ordering of self-organized nanostructures by ion sputtering," *Nuclear*

Instruments and Methods in Physics Research Section B: Beam Interactions with Materials and Atoms **216** (2004) 9–19.

[22] Y. Wang, S. F. Yoon, C. Y. Ngo, and J. Ahn, "Surface Morphology Evolution of GaAs by Low Energy Ion Sputtering," *Nanoscale Research Letters* **2** (2007) no. 10, 504–508.

[23] T. Bobek, S. Facsko, H. Kurz, T. Dekorsy, M. Xu, and C. Teichert, "Temporal evolution of dot patterns during ion sputtering," *Physical Review B* **68** (2003) no. 8, 1–6.

[24] M. Xu, "Size distribution and dot shape of self-assembled quantum dots induced by ion sputtering," *Physica E: Low-dimensional Systems and Nanostructures* **25** (2005) no. 4, 425–430.

[25] S. Facsko, H. Kurz, and T. Dekorsy, "Energy dependence of quantum dot formation by ion sputtering," *Physical Review B* **63** (2001) no. 16, 1–5.

[26] O. Plantevin, R. Gago, L. Vázquez, A. Biermanns, and T. H. Metzger, "In situ x-ray scattering study of self-organized nanodot pattern formation on GaSb(001) by ion beam sputtering," *Appl. Phys. Lett.* **91** (2007) no. 11, 113105.

[27] a. Keller, a. Biermanns, G. Carbone, J. Grenzer, S. Facsko, O. Plantevin, R. Gago, and T. H. Metzger, "Transition from smoothing to roughening of ion-eroded GaSb surfaces," *Applied Physics Letters* **94** (2009) no. 19, 193103.

[28] S. Le Roy, E. Barthel, N. Brun, A. Lelarge, and E. Søndergård, "Self-sustained etch masking: a new concept to initiate the formation of nanopatterns during ion erosion," *Journal of Applied Physics* **106** (2009) no. 9, 094308.

[29] I. J. Hodgkinson and Q. H. Wu, *BIREFRINGENT THIN FILMS AND POLARIZING ELEMENTS*. World Scientific, 1997.

[30] A. Sihvola, *Electromagnetic mixing formulas and applications*. IEE ELECTROMAGNETIC WAVES SERIES 47, 1999.

[31] P. Hauge, "Conventions and formulas for using the Mueller-Stokes calculus in ellipsometry,"*Surface Science* **96** (June, 1980) 81–107.

[32] E. Collett, *Polarized light. Fundamentals and applications*. Marcel Dekker, Inc., New York.

[33] M. Schubert, "Theory and Application of Generalized Ellipsometry," in *Handbook of Ellipsometry*, Tompkins, H. G. and Irene, E. A., ed. 2005.

[34] G. E. Jellison and F. A. Modine, "Two-modulator generalized ellipsometry: theory," *Appl. Opt.* **36** (Nov, 1997) 8190–8198.

[35] S.-Y. Lu and R. A. Chipman, "Interpretation of mueller matrices based on polar decomposition," *J. Opt. Soc. Am. A* **13** (1996) no. 5, 1106–1113.

[36] S. R. Cloude and E. Pottier, "The concept of polarisation entropy in optical scattering," *Optical Engineering* **34** (1995) 1599–1610.

[37] D. W. Berreman, "Optics in stratified and anisotropic media: 4x4-matrix formulation," *J. Opt. Soc. Am.* **62** (1972) no. 4, 502–510.

[38] H. Wöhler, G. Haas, M. Fritsch, and D. A. Mlynski, "Faster 4×4 matrix method for uniaxial inhomogeneous media," *J. Opt. Soc. Am. A* **5** (1988) no. 9, 1554–1557.

[39] S. Teitler and B. W. Henvis, "Refraction in stratified, anisotropic media," *J. Opt. Soc. Am.* **60** (1970) no. 6, 830–834.

[40] P. Yeh, "Optics of anisotropic layered media: A new 4×4 matrix algebra," *Surface Science* **96** (1980) no. 1-3, 41 – 53.

[41] H. Goldstein, C. P. Poole, and J. L. Safko, *Classical Mechanics*. Addison Wesley, 2001.

[42] M. Schubert, "Polarization-dependent optical parameters of arbitrarily anisotropic homogeneous layered systems," *Phys. Rev. B* **53** (Feb., 1996) 4265–4274.

[43] J. D. Jackson, *Classical Electrodynamics*. John Wiley & Sons, Inc., 1998.

[44] D. E. Aspnes, "Local-field effects and effective-medium theory: A microscopic perspective," *American Journal of Physics* **50** (1982) no. 8, 704–709.

[45] J. E. Spanier and I. P. Herman, "Use of hybrid phenomenological and statistical effective-medium theories of dielectric functions to model the infrared reflectance of porous sic films," *Phys. Rev. B* **61** (Apr., 2000) 10437–10450.

[46] U. Kreibig and M. Vollmer, *Optical Properties of Metal Clusters*. Springer, 1995.

[47] C. Granqvist and O. Hunderi, "Optical properties of ultrafine gold particles," *Physical Review B* **16** (1977) no. 8, 3513–3534.

[48] T. Yamaguchi, S. Yoshida, and A. Kinbara, "Optical effect of the substrate on the anomalous absorption of aggregated silver films," *Thin Solid Films* **21** (1974) no. 1, 173 – 187.

[49] K. Wasa and S. Hayakawa, *Handbook of sputter deposistion technology.* Noyes publications, 1992.

[50] E. Taglauer, "Surface cleaning using sputtering," *Appl. Phys. A* **51** (1990) no. 3, 238–251.

[51] F. Frost, R. Fechner, B. Ziberi, D. Flamm, and A. Schindler, "Large area smoothing of optical surfaces by low-energy ion beams," *Thin Sol. Films* **459** (2004) 100–1005.

[52] C. S. M. Navez and D. Chaperot *Compte Rendue Academie des Sciences de Paris* **254** (1962) 240.

[53] E. C. W. L. Chan, "Making waves: Kinetic processes controlling surface evolution during low energy ion sputtering," *J. Appl. Phys.* **101** (2007) 121301.

[54] U. Valbusa, C. Boragno, and F. Buatier de Mongeot, "Nanostructuring surfaces by ion sputtering," *Journal of Physics: Condensed Matter* **14** (2002) no. 35, 8153.

[55] R. Moroni, D. Sekiba, F. Buatier de Mongeot, G. Gonella, C. Boragno, L. Mattera, and U. Valbusa, "Uniaxial magnetic anisotropy in nanostructured $co/cu(001)$: From surface ripples to nanowires," *Phys. Rev. Lett.* **91** (2003) no. 16, 167207.

[56] A. Toma, D. Chiappe, D. Massabo, C. Boragno, and F. Buatier de Mongeot, "Self-organized metal nanowire arrays with tunable optical anisotropy," *Applied Physics Letters* **93** (2008) no. 16, 163104.

[57] R. M. Bradley and J. M. E. Harper, "Theory of ripple topography induced by ion bombardment," *J. Vac. Sci. Technol., A* **6** (1988) 2390.

[58] S. Le Roy, *Nanostructuration sous abrasion ionique par formation d'un masque auto-entretenu.* PhD thesis, Docteur de l'Ecole Polytechnique, Palaiseau, France, 2010.

[59] P. Sigmund, "Theory of Sputtering. I. Sputtering Yield of Amorphous and Polycrystalline Targets," *Phys. Rev.* **184** (1969) 383.

[60] S. Facsko, T. Bobek, A. Stahl, H. Kurz, and T. Dekorsy, "Dissipative continuum model for self-organized pattern formation during ion-beam erosion," *Phys. Rev. B* **69** (Apr, 2004) 153412.

[61] M. Castro, R. Cuerno, L. Vázquez, and R. Gago, "Self-organized ordering of nanostructures produced by ion-beam sputtering," *Phys. Rev. Lett.* **94** (Jan, 2005) 016102.

[62] V. B. Shenoy, W. L. Chan, and E. Chason, "Compositionally modulated ripples induced by sputtering of alloy surfaces," *Phys. Rev. Lett.* **98** (2007) no. 25, 256101.

[63] R. M. Bradley and P. D. Shipman, "Spontaneous pattern formation induced by ion bombardment of binary compounds," *Phys. Rev. Lett.* **105** (2010) no. 14, 145501.

[64] W. Yu, J. L. Sullivan, and S. O. Saied, "XPS and LEISS studies of ion bombarded GaSb, InSb and CdSe surfaces," *Surface Science* **352-354** (1996) 781 – 787.

[65] D. E. Aspnes, J. B. Theeten, and F. Hottier, "Investigation of effective-medium models of microscopic surface roughness by spectroscopic ellipsometry," *Phys. Rev. B* **20** (1979) no. 8, 3292–3302.

[66] H. Akazawa, "Real-time ellipsometric modeling and characterization of the evolution of nanometer-scale Ge islands and pits in Ge homoepitaxy," *Journal of Applied Physics* **106** (2009) no. 10, 104312.

[67] L. Armelao, D. Barreca, G. Bottaro, G. Bruno, a. Gasparotto, M. Losurdo, and E. Tondello, "RF-sputtering of gold on silica surfaces: Evolution from clusters to continuous films," *Materials Science and Engineering: C* **25** (Dec., 2005) 599–603.

[68] C. Wongmanerod, S. Zangooie, and H. Arwin, "Determination of pore size distribution and surface area of thin porous silicon layers by spectroscopic ellipsometry,".

[69] Bragg, W. L. and Pippard, A. B., "The form birefringence of macromolecules," *Acta Crystallographica* **6** (1953) no. 11-12, 865–867.

[70] K. Kaminska, A. Amassian, L. Martinu, and K. Robbie, "Growth of vacuum evaporated ultraporous silicon studied with spectroscopic ellipsometry and scanning electron microscopy," *Journal of Applied Physics* **97** (2005) no. 1, 013511.

[71] D. W. Thompson, P. G. Snyder, L. Castro, L. Yan, P. Kaipa, and J. a. Woollam, "Optical characterization of porous alumina from vacuum ultraviolet to midinfrared," *Journal of Applied Physics* **97** (2005) no. 11, 113511.

[72] A. C. Gâlca, E. S. Kooij, H. Wormeester, C. Salm, V. Leca, J. H. Rector, and B. Poelsema, "Structural and optical characterization of porous anodic aluminum oxide," *Journal of Applied Physics* **94** (2003) no. 7, 4296–4305.

[73] G. Beydaghyan, C. Buzea, Y. Cui, C. Elliott, and K. Robbie, "Ex situ ellipsometric investigation of nanocolumns inclination angle of obliquely evaporated silicon thin films," *Appl. Phys. Lett.* **87** (Oct., 2005) 153103.

[74] J. Gospodyn and J. Sit, "Characterization of dielectric columnar thin films by variable angle Mueller matrix and spectroscopic ellipsometry," *Optical Materials* **29** (2006) no. 2-3, 318–325.

[75] M. Gilliot, A. En Naciri, L. Johann, J. Stoquert, J. J. Grob, and D. Muller, "Optical anisotropy of shaped oriented cobalt nanoparticles by generalized spectroscopic ellipsometry," *Physical Review B* **76** (2007) no. 4, 1–15.

[76] D. Schmidt, B. Booso, T. Hofmann, E. Schubert, A. Sarangan, and M. Schubert, "Generalized ellipsometry for monoclinic absorbing materials: determination of optical constants of Cr columnar thin films," *Optics Letters* **34** (2009) no. 7, 992.

[77] D. Schmidt, A. C. Kjerstad, T. Hofmann, R. Skomski, E. Schubert, and M. Schubert, "Optical, structural, and magnetic properties of cobalt nanostructure thin films," *Journal of Applied Physics* **105** (2009) no. 11, 113508–+.

[78] D. Schmidt, B. Booso, T. Hofmann, E. Schubert, A. Sarangan, and M. Schubert, "Monoclinic optical constants, birefringence, and dichroism of slanted titanium nanocolumns determined by generalized ellipsometry," *Applied Physics Letters* **94** (JAN 5, 2009) 011914.

[79] M. Ranjan, T. W. H. Oates, S. Facsko, and W. Möller, "Optical properties of silver nanowire arrays with 35 nm periodicity.," *Optics letters* **35** (2010) no. 15, 2576–8.

[80] D. E. Aspnes and A. A. Studna, "Dielectric functions and optical parameters of Si, Ge, GaP, GaAs, GaSb, InP, InAs, and InSb from 1.5 to 6.0 eV," *Phys. Rev. B* **27** (1983) no. 2, 985–1009.

[81] S. Zollner, M. Garriga, J. Humlicieck, S. Goplan, and M. Cardona, "Temperature dependence of the dielectric function and the interband critical-point parameters of GaSb.pdf," *Phys. Rev. B* **43** (1991) no. 5, 4349–4360.

[82] D. Bedaux and J. Vlieger, *Optical Properties Of Surfaces*. World Scientific, 2004.

[83] H. Wormeester, E. Kooij, and B. Poelsema, "Unambiguous optical characterization of nanocolloidal gold films," *Physical Review B* **68** (2003) no. 8, 1–6.

[84] H. Wormeester, "Ellipsometric characterisation of heterogeneous 2D layers," *Thin Solid Films* **455-456** (2004) 323–334.

[85] M. Moharam, E. Grann, D. Pommet, and T. Gaylord, "Formulation for stable and efficient implementation of the rigorous coupled-wave analysis of binary gratings," *J. Opt. Soc. Am. A* **12** (1995) no. 5, 1068–1076.

[86] Y. Chang, G. Li, H. Chu, and J. Opsal, "Efficient finite-element, Green's function approach for critical-dimension metrology of three-dimensional gratings on multilayer films," *JOSA A* **23** (2006) no. 3, 638–645.

[87] S.-H. Hsu, E.-S. Liu, Y.-C. Chang, J. N. Hilfiker, Y. D. Kim, T. J. Kim, C.-J. Lin, and G.-R. Lin, "Characterization of Si nanorods by spectroscopic ellipsometry with efficient theoretical modeling," *Physica Status Solidi (a)* **205** (2008) no. 4, 876–879.

[88] H. Wormeester, F. Everts, and B. Poelsema, "Plasmon resonance shift during grazing incidence ion sputtering on Ag(001)," *Thin Solid Films* **519** (2011) no. 9, 2664–2667.

[89] D. Bergman, "The dielectric constant of a composite material - a problem in classical physics," *Physics Reports* **43** (1978) no. 9, 377–407.

[90] E. Garcia-Caurel, A. D. Martino, and B. Drévillon, "Spectroscopic Mueller polarimeter based on liquid crystal devices," *Thin Solid Films* **455-456** (2004) 120–123.

[91] A. M. Gandorfer, "Ferroelectric retarders as an alternative to piezoelastic modulators for use in solar Stokes vector polarimetry," *Optical Engineering* **38** (1999) no. 8, 1402–1408.

[92] E. Compain, S. Poirier, and B. Drevillon, "General and self-consistent method for the calibration of polarization modulators, polarimeters, and Mueller-matrix ellipsometers," *Applied Optics* **38** (1999) no. 16, 3490–3502.

[93] W. H. Press, S. A. Teukolsky, W. T. Vetterling, and B. P. Flannery, *Numerical Recipes: The Art of Scientific Computing*. Cambridge University Press, 2007.

[94] R. W. Collins and J. Koh, "Dual rotating-compensator multichannel ellipsometer: Instrument design for real-time mueller matrix spectroscopy of surfaces and films," *Journal of the Optical Society of America A: Optics and Image Science, and Vision* **16** (1999) no. 8, 1997–2006.

[95] Horiba Jobin Yvon. Http://www.horiba.com/scientific/products/ellipsometers/.

[96] B. Drévillon, "Phase modulated ellipsometry from the ultraviolet to the infrared: In situ application to the growth of semiconductors," *Progress in Crystal Growth and Characterization of Materials* **27** (1993) no. 1, 1–87.

[97] L. Halagacka, K. Postava, M. Foldyna, and J. Pistora, "Precise phase-modulation generalized ellipsometry of anisotropic samples," *physica status solidi (a)* **205** (2008) no. 4, 752–755.

[98] A. De Martino, S. Ben Hatit, and M. Foldyna, "Mueller polarimetry in the back focal plane," in *Society of Photo-Optical Instrumentation Engineers (SPIE) Conference Series*, vol. 6518 of *Society of Photo-Optical Instrumentation Engineers (SPIE) Conference Series*. 2007.

[99] B. H. Ibrahim, S. B. Hatit, and A. De Martino, "Angle resolved mueller polarimetry with a high numerical aperture and characterization of transparent biaxial samples," *Appl. Opt.* **48** (2009) no. 27, 5025–5034.

[100] S. B. Hatit, M. Foldyna, A. De Martino, and B. Drévillon, "Angle-resolved mueller polarimeter using a microscope objective," *physica status solidi (a)* **205** (2008) no. 4, 743–747.

[101] tectra GmbH. Http://www.plasma-source.de/.

[102] R. Anton, T. Wiegner, W. Naumann, M. Liebmann, C. Klein, and C. Bradley, "Design and performance of a versatile, cost-effective microwave electron cyclotron resonance plasma source for surface and thin film processing," *Review of Scientific Instruments* **71** (2000) no. 2, 1177–1180.

[103] MTI Corporation. Http://www.mtixtl.com/gasbwafer100undoped2x045mmonesidepolished.aspx.

[104] F. J. Giessibl, "Advances in atomic force microscopy," *Rev. Mod. Phys.* **75** (2003) no. 3, 949–983.

[105] P. Eaton and P. West, *Atomic force microscopy.* Oxford University Press, 2010.

[106] H. Fujiwara, J. Koh, P. Rovira, and R. Collins, "Assessment of effective-medium theories in the analysis of nucleation and microscopic surface roughness evolution for semiconductor thin films," *Physical Review B* **61** (2000) no. 16, 10832–10844.

[107] P. Petrik, L. P. Biró, M. Fried, T. Lohner, R. Berger, C. Schneider, J. Gyulai, and H. Ryssel, "Comparative study of surface roughness measured on polysilicon using spectroscopic ellipsometry and atomic force microscopy," *Thin Solid Films* **315** (1998) no. 1-2, 186 – 191.

[108] G. I. Goldstein, D. E. Newbury, P. Echlin, D. C. Joy, C. Fiori, and E. Lifshin, *Scanning electron microscopy and x-ray microanalysis.* New York: Plenum Press, 1981.

[109] G. Renaud, R. Lazzari, C. Revenant, A. Barbier, M. Noblet, O. Ulrich, F. Leroy, J. Jupille, Y. Borensztein, C. R. Henry, J.-P. Deville, F. Scheurer, J. Mane-Mane, and O. Fruchart, "Real-Time Monitoring of Growing Nanoparticles," *Science* **300** (2003) no. 5624, 1416–1419.

[110] C. Chen, M. Horn, S. Pursel, C. Ross, and R. Collins, "The ultimate in real-time ellipsometry: Multichannel mueller matrix spectroscopy," *Applied Surface Science* **253** (2006) no. 1, 38 – 46.

[111] D. Aspnes, J. Harbison, A. Studna, and L. Florez, "Reflectance-difference spectroscopy system for real-time measurements of crystal growth," *Applied Physics Letters* **52** (1988) no. 12, 957–959.

[112] J. Bremer and O. Hunderi, "RAS Studies of Laterally Nanostructured Surfaces," *physica status solidi (a)* **184** (2001) no. 1, 89–100.

[113] W. Richter, "In-situ observation of movpe epitaxial growth," *Applied Physics A: Materials Science* **75** (2002) 129–140.

[114] F. Everts, H. Wormeester, and B. Poelsema, "Optical anisotropy induced by ion bombardment of Ag(001)," *Phys. Rev. B* **78** (Oct, 2008) 155419.

Chapter 7

Papers

My contributions to the papers

For all the papers, all authors contributed in discussions and in commenting and writing the manuscripts.

Paper I
In this paper, I developed an optical model to represent the GaSb nanopillars, performed all data analysis and wrote the main parts of the paper. The samples were prepared and characterized with AFM by Sebastien Le Roy, electron microscopy images were collected by John Walmsley and Liviu Holt, the ellipsometry measurements were mainly performed by Morten Kildemo. In addition to the mentioned authors, Ingve Simonsen contributed in discussions on optical modeling and with writing the paper.

Paper II
I performed all analysis of the real-time ellipsometry data and wrote the paper. I mounted the ellipsometer on the sputtering chamber, prepared samples and performed real-time measurements in collaboration with Sebastien Le Roy and other staff at Saint–Gobain. Sebastien Le Roy performed all AFM measurements and analysis.

Paper III
I performed all the spectroscopic Mueller matrix measurements, developed an optical model for the inclined nanopillars, performed all analysis of the optical data, and wrote the paper. The samples were prepared and imaged by SEM in collaboration with Sebastien Le Roy. The angle resolved Mueller measurements was performed by Martin Foldyna.

Paper IV
I performed the analysis of the optical measurements, and wrote the corresponding parts of the paper. I performed the real-time measurements and prepared the samples together with Sebastien Le Roy. Sebastien Le Roy and Elin Søndergård wrote most of the paper.

Paper V
I performed the optical analysis, recorded SEM images and wrote the paper. I performed the real-time measurements and prepared the samples together with Sebastien Le Roy. The angle resolved Mueller measurements were performed by Martin Foldyna.

Paper VI
I contributed in discussions and planning, and wrote the introduction and theory part on polarimetry. Paul Anton Letnes performed the optimization with the genetic algorithm and wrote the corresponding part of the paper. Lars Martin S. Aas and Pål Gunnar Ellingsen contributed in discussions, planning and programming.

Characterisation of nanostructured GaSb : Comparison between large-area optical and local direct microscopic techniques

Paper I

Characterization of nanostructured GaSb: comparison between large-area optical and local direct microscopic techniques

I. S. Nerbø,[1,*] M. Kildemo,[1] S. Le Roy,[2] I. Simonsen,[1,2] E. Søndergård,[2] L. Holt,[1] and J. C. Walmsley[1]

[1]Department of Physics, Norwegian University of Science and Technology (NTNU), NO-7491 Trondheim, Norway

[2]Surface du Verre et Interfaces, Unité Mixte de Recherche CNRS/Saint-Gobain Laboratoire, UMR 125, 39 Quai Lucien Lefranc, F-93303 Aubervilliers Cedex, France

*Corresponding author: ingar.nerbo@ntnu.no

Received 28 May 2008; accepted 13 August 2008;
posted 21 August 2008 (Doc. ID 96717); published 24 September 2008

Low energy ion-beam sputtering of GaSb results in self-organized nanostructures with the potential of structuring large surface areas. Characterization of such nanostructures by optical methods is studied and compared to direct (local) microscopic methods. The samples consist of densely packed GaSb cones on bulk GaSb, approximately 30, 50, and 300 nm in height, prepared by sputtering at normal incidence. The optical properties are studied by spectroscopic ellipsometry, in the range 0.6–6.5 eV, and with Mueller matrix ellipsometry in the visible range, 1.46–2.88 eV. The optical measurements are compared to direct topography measurements obtained by scanning electron microscopy, high resolution transmission electron microscopy, and atomic force microscopy. Good agreement is achieved between the two classes of methods when the experimental optical response of the short cones (<55 nm) is inverted with respect to topological surface information, via a graded anisotropic effective medium model. The main topological parameter measured was the average cone height. Optical methods are shown to represent a valuable characterization tool of nanostructured surfaces, in particular when a large coverage area is desirable. Because of the fast and nondestructive properties of optical techniques, they may readily be adapted to *in situ* configurations.

OCIS codes: 120.2130, 160.4236, 310.6628, 260.2065.

1. Introduction

The recent advent of nanotechnology and nanoscience has made it increasingly important to be able to "see" features of a sample down to a nanometric scale. Today this is typically achieved with the aid of several well-established microscopic techniques like, atomic force microscopy (AFM), scanning electron microscopy (SEM) and transmission electron microscopy (TEM). All these techniques can achieve nanometric resolution, and are therefore attractive when one wants to image the fine details of a sample. Moreover, they can be said to be *local* in the sense that only a rather small surface area can be imaged with good resolution. They are also rather time consuming techniques, and the required equipment is costly and physically large. As a result, they are not generally suited for *in situ* characterization.

Traditionally, optical techniques have been attractive for *in situ* studies due to its measurement speed, relatively low equipment cost, noncontact properties, and ease of integration with other setups. Optical techniques also have the advantage of being able to cover a large surface area with relative ease. This is a great advantage, for instance, in monitoring applications where it is the average properties that are of interest, and not the local features at a given

0003-6935/08/285130-10$15.00/0

location at the surface. For nanometer scale structures, the applicability of optical techniques are limited by the diffraction limit [1], making imaging of such structures by visible light impossible. However, even if direct optical imaging is challenging for nanostructures, it is well-known that they can have strong polarization altering properties on the incident radiation. Hence, indirect optical techniques can, in principle, be devised for the purpose of extracting topographic information about the sample. The aim of this paper is to present such a methodology, and to compare the large area optical result to local information obtained by direct methods.

Spectroscopic ellipsometry (SE) is a celebrated polarimetric technique, much used for measuring the thickness of thin film layers and for determining the index of refraction of materials. It can also be used to characterize nanostructures. For example, generalized ellipsometry has been used to measure the inclination angle of nanorods [2]. The sensitivity of spectroscopic ellipsometry to the thickness of thin layers is remarkable and can be down to single atom layers. This is achieved by knowing the refractive indices of the materials and utilizing optical models. The aim of this study is to exploit SEs sensitivity of thin film thickness to accurately measure the height of conical shaped nanostructures. This is done by developing a suitable optical model. Information on shape and regularity can possibly also be attained. The ellipsometric spot will always average over a relatively large (surface) area, providing information on the mean properties of the structures. It is both noninvasive and fast, making it suitable as a tool for *in situ* characterization.

Nanostructured surfaces and materials open up for a new range of applications. In photonics, for example, optical properties of thin films may be mimicked by nanostructures and supply new and enhanced properties (see e.g., [2], and references therein). An example of such properties can be antireflective coatings with low reflectivity over a large spectral range and a wide range of incident angles [3].

Low energy ion sputtered GaSb is a good example of self-organized formation of densely packed cones and has been proposed as a cost-effective method for production of e.g., quantum dots [4]. The properties of such a surface may, to a large extent, be tailored by controlling sputtering conditions. The latter issue is a typical target application area of ellipsometry. In the case of a future large scale production of such surfaces, SE could possibly be used as an efficient production control tool for testing individual samples.

Here, optical models are initially constructed from observations from high resolution transmission electron microscopy (HR-TEM), field emission gun scanning electron microscopy (FEG-SEM), and AFM. The latter give a direct observation of the nanostructures, with respect to density, cone separation, cone height, number of nearest neighbors, etc. Information on the shape and crystal structure of individual cones, were obtained from HR-TEM studies of carefully prepared slices of nanostructured GaSb.

This paper is organized as follows: In Section 2 we describe the experimental details of both the direct microscopic (SEM, TEM, and AFM), and the optical (SE) studies. A brief theoretical background on ellipsometry is also given. In Section 3 we present the results of these studies. The optical properties of conical nanostructures are discussed in relation to the effective medium approximation. An optical model is presented in Subsection 3.C that enables characterization of such structures from optical measurements by fitting the model parameters to the SE measurements. Information gained from optical characterization are finally compared to the results from the direct microscopic studies.

2. Experimental Details and Theoretical Background

The samples consisted of GaSb sputtered by low energy Ar^+ ions [5]. The sputtering conditions for each sample are reported in Table 1. The substrates were crystalline GaSb (100) wafers of 500 μm thickness. All samples were sputtered at room temperature. The samples characterized in this study (samples A–D) were all sputtered at normal ion incidence. Additional samples were also prepared by sputtering at 45° ion incidence, resulting in nanocones tilted from the surface normal [6]. Characterization of such structures are left for future work. The FEG-SEM images were obtained using a Hitachi S-4300SE, and Zeiss Supra instruments. TEM analysis was performed using a JEOL 2010F. Cross section TEM samples were prepared by both ion-milling and ultramicrotomy to investigate possible preparation induced artefacts in the microstructure. Ion-milling was performed using a Gatan PIPS instrument, operating at 3.5 kV with a thinning angle of 3.5–4°. Ultramicrotomy was performed using a Reichart–Jung Ultracut E instrument. AFM measurements were done by a DI-VEECO AFM with a NanoScope IIIa controller from Digital Instruments, operated in tapping mode. Silicon tips with radius less than 10 nm were used.

The optical far field measurements were performed using a commercial photo-elastic-modulator spectroscopic ellipsometer (PMSE) in the photon energy range 0.6–6.5eV (UVISEL, Horriba Jobin Yvon), at an angle of incidence of 55°. The complete Mueller matrix was also measured using a commercial ferroelectric liquid-crystal retarder-based Mueller matrix

Table 1. Sputtering Conditions and Definition of the Samples

Sample Name	Sputter Time (min)	Mean Temperature (°C)	Applied Voltage (V)	Average Flux (mA/cm^2)
A	10	33	–400	0.098
B	10	41	–400	0.096
C	10	35	–300	0.28
D	10	47	–500	0.37

ellipsometer (MM16) in the range 1.46–2.88 eV (850–430 nm). Such measurements were made for several angles of incidence in the range from 55° to 70° and as a function of the sample rotation angle around its normal to the (mean) surface. The orientation of the sample with respect to the direction of the incoming beam was carefully recorded, and the sample was rotated manually in steps of 45(±2)°, with a total sample rotation in all cases of at least 360°.

The PMSE measurements were performed in the standard UVISEL setup, i.e., a polarizer-sample-PEM-analyzer, where the angle of the fast axis of the PEM with respect to the analyzer is fixed at 45°. Measurements were performed in the standard PMSE configurations ($\Theta_M = 0°$, $\Theta_A = 45°$) [7], determining $I_s = -m_{43}$ and $I_c = m_{33}$, where m_{43} and m_{33} are normalized Mueller matrix elements related to the unormalized Mueller matrix M by $m = M/M_{11}$. For the reflection from an isotropic planar surface, they can be defined according to

$$I_s = -m_{43} = \sin 2\Psi \sin \Delta, \tag{1}$$

$$I_c = m_{33} = \sin 2\Psi \cos \Delta, \tag{2}$$

where Ψ and Δ denote the ellispometric angles related to the ratio of the complex reflection amplitudes $r_{pp}/r_{ss} = \tan \Psi e^{i\Delta}$ [8].

Additional measurements were performed in the configuration ($\Theta_M = 45°, \Theta_A = 45°$), enabling the determination of

$$I_{c_2} = -m_{12} = \cos 2\Psi. \tag{3}$$

The quantities, I_s, I_c, and I_{c_2}, as defined in Eqs. (1)–(3) are known as the ellipsometric intensities. For block-diagonal Mueller matrices, these intensities can be used to define the degree of polarization P [9]:

$$P = \sqrt{I_s^2 + I_c^2 + I_{c_2}^2}. \tag{4}$$

A discussion on when a sample will have a block-diagonal Mueller matrix will be given in the Section 3. From the full Mueller matrix, experimentally available here in the range 1.46–2.88 eV, it is also customary to define the so-called depolarization index (consult, e.g., Ref. [10] for a more detailed discussion of depolarization measures):

$$D_P = \frac{\sum_{i,j} M_{ij}^2 - M_{11}^2}{\sqrt{3} M_{11}}, \tag{5}$$

where M_{ij} denotes the nonnormalized Mueller matrix elements [10]. P (and in most cases D_P) determine how much of the outgoing light will be totally polarized for totally-polarized incident light. Reflectance measurements were also performed by the PMSE, in which $M_{11} = (R_{ss} + R_{pp} + R_{sp} + R_{ps})/2$ was determined by using a standard Al mirror reference sample, and assuming stable intensity conditions. The reflectance spectrum was recorded from 1.5–6.5 eV in steps of 0.1 eV.

3. Results and Discussion

A. Experimental Observations—SEM, TEM, and AFM Results

In Fig. 1, FEG-SEM images of samples A and D are presented, for both normal beam incidence (left-hand images), and tilted beam incidence (right-hand images). The cones do not show a high degree of organization but, on average, have 6 neighbors. This result was found from statistical treatment of AFM measurements of the samples, but could as well have been found from SEM images. The result corresponds well with the Euler law [11], which states that the mean number of nearest neighbors for a structure created by a random process is 6. The average cone separation $\langle D \rangle$ has been estimated from the cone density, by assuming the cones are ordered on a perfect hexagonal lattice. The average heights of the cones $\langle h \rangle$ were nominally estimated from AFM, but for sample A it was estimated from HR-TEM. The average cone heights and cone separations are given in Table 2, along with the estimated standard deviation σ_h of $\langle h \rangle$.

Figure 2 depicts a HR-TEM image of selected cones from sample A prepared by ion-milling. The average cone height of A was estimated to be 55 nm, obtained by taking the average of 16 cones measured by HR-TEM. The shape was found to be conical with a somewhat rounded tip. The typical cone angle, defined as the angle between the substrate and the cone side wall, was found to be roughly $\alpha = 73°$. From the HR-TEM images in Fig. 2, it is observed that the

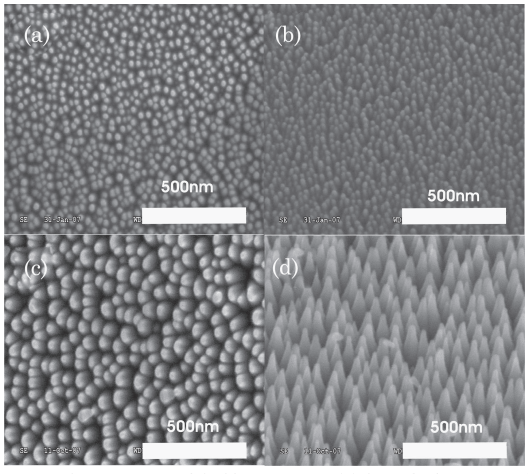

Fig. 1. SEM images of GaSb nanocones.(a) Sample A at normal beam incidence, (b) tilted sample A. Sample D is also depicted at (c) normal beam incidence and (d) tilted beam incidence.

Table 2. Results of AFM, TEM, and SEM Studies of GaSb Nanocone Samples

Sample Name	$\langle h \rangle$ (nm)	σ_h (nm)	Density (μm^2)	$\langle D \rangle^*$ (nm)	α (degree)
A	55 [b]	5.4 [b]	549 [c]	46 [c]	73 [b]
B	46.5 [c]	5.2 [c]	948 [c]	35 [c]	
C	47.6 [c]	8.85 [c]	766 [c]	39 [c]	
D	299 [d]	40 [d]	74.25[c]	125 [c]	77.2 [d]

[a] $\langle h \rangle$ is the average cone height, with standard deviation σ_h. Density is the number of cones per μm, D is the average distance between neighboring cone centers, while α is the average cone angle. The tabulated results have been found from the following:
[b] TEM studies.
[c] AFM measurements.

interior of the cones consisted of primarily crystalline material, with the same crystal orientation as the substrate. Furthermore, the cone surface appeared to be surrounded by a thin (less than 5 nm) layer of undetermined amorphous material. From the rapid oxidation of clean GaSb to an approximately 5–7nm GaSb-oxide layer, it is argued that this surrounding layer is partially oxidized.

Another slice of nanostructured GaSb (sample A) , was prepared by ultramicrotomy. This sample did not provide such a thin sector as the ion-milled samples. However, it was sufficient to confirm the structure observed in the ion-milled samples. The crystalline nature of the interior of the cones and the amorphous surrounding layer is in line with the observations by Facsko *et al.* [4].

In summary, from the TEM studies mainly three phases appear to be involved in the layer (thin film) defined by the cones. These phases are crystalline GaSb (c-GaSb), amorphous GaSb (a-GaSb), and presumed GaSb-oxide, in addition to the voids between the cones. The remaining samples were studied by AFM and by FEG-SEM, and detailed results are compiled in Table 2. It is suspected that the AFM tip is too blunt to reach the bottom between close-packed cones. Therefore, when estimating average cone height $\langle h \rangle$, the height of each cone top has been defined relative to the lowest point in an area within the maximal distance between the cones. This minimum is typically found in a place where the cones stand further apart, and the tip can reach the bottom. This may overestimate average height $\langle h \rangle$ somewhat.

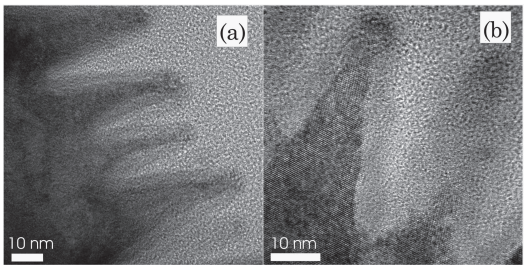

Fig. 2. High resolution TEM images of GaSb nanocones (sample A). Figure (a) shows several cones while figure (b) shows one individual cone in greater detail. The lighter part of the image is the amorphous adhesive used in the sample preparation. The crystalline cones appear darker and in (b) the atomic column spacing at the 110 GaSb zone-axis orientation is clearly visible. The approximately 5 nm layer of amorphous GaSb oxide is visible as a shadow around the cones that has slightly darker contrast than the adhesive.

B. Experimental Observations—Spectroscopic Ellipsometry

Figure 3 shows the SE measurements of $I_s = -m_{43}$, $I_c = m_{33}$ of a clean GaSb surface with approximately 7 nm of oxide. In addition it shows, as an overview, the ellipsometric measurements of samples A, B, C (short cones), and D (longer cones). All cones were formed by sputtering at normal incidence. The nanostructuration of the surface strongly modifies the polarization-dependent optical response. Another interesting feature is the reflectance of such nanostructured surfaces, which have additional practical applications. It is particularly clear from Fig. 4 that the reflectance is much reduced, compared to the clean surface, at higher photon energies. Furthermore, the antireflection properties tend to appear for lower energies as the cones get higher. This could be explained as a motheye effect from the graded index of refraction [12].

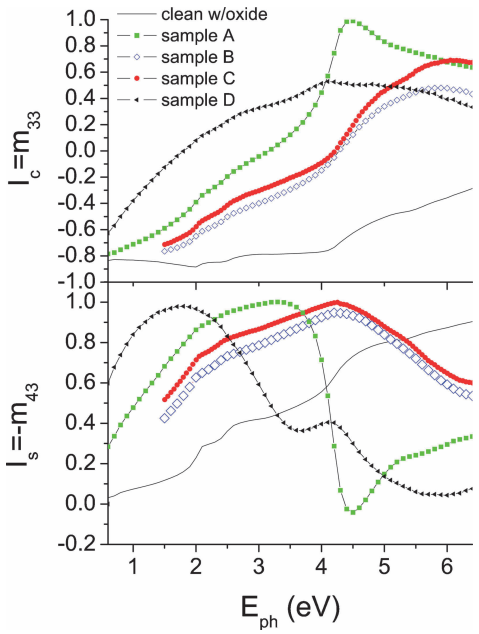

Fig. 3. (Color online) Ellipsometric intensities $I_s = -m_{43}$, $I_c = m_{33}$, of plane GaSb with 7 nm oxide, short nanostructured cones, samples A, B, and C (approximately 50 nm high cones), and sample D (approximately 300 nm cones).

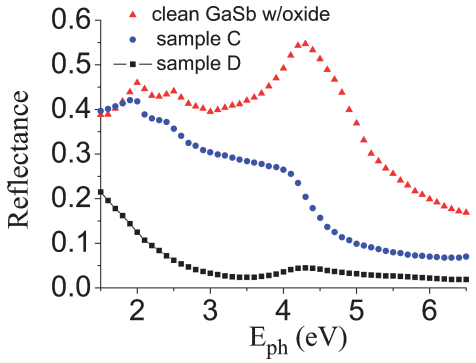

Fig. 4. (Color online) Reflectance (M_{11}) of nanostructured GaSb cones, for sample C (approximately 36 nm high cones) and D (approximately 300 nm high cones). As a reference, the reflectance of a clean GaSb surface with oxide is also included.

From FEG-SEM and HR-TEM images, it is observed that the samples consist of conical nanostructures of various sizes. For sufficiently small cones, the surface can be treated as a thin film layer of effective medium. This layer will be uniaxially anisotropic since the cones will show a different response to an electric field normal to the mean surface than to a field parallel to it. Anisotropic uniaxial materials with the optic axis in the plane of incidence will appear like an isotropic material under ellipsometric investigations ($r_{sp} = r_{ps} = 0$) [13], in the sense that reflections from such materials will be described by a diagonal Jones matrix, and by a block-diagonal Mueller–Jones matrix. This means that all the polarization altering properties of the structured surface can be described by the ellipsometric angles Ψ and Δ, derived from the ellipsometric intensities I_s and I_c.

Cones being directed normal to the surface have a symmetry axis that is normal to the mean surface, and the approximated effective media must therefore have an optic axis in the same direction, i.e., it will appear like an isotropic material and can be fully characterized by regular (standard) ellipsometry. The samples will then have full azimuth rotation symmetry (around the sample normal). If the cones are tilted from the sample normal, this will generally no longer be the case (except for the two special azimuth orientations where the tilted cones lie in the plane of incidence). The structures will then correspond to an anisotropic material with a tilted optic axis. To describe the polarizing properties of reflections from such a surface, one also needs to account for the coupling of the s and p polarization through the reflections coefficients r_{sp} and r_{ps}, in addition to r_{pp} and r_{ss}. A long range ordering, or anisotropic shapes of the individual cones, would also break the rotation symmetry and give polarization coupling. To fully characterize such a sample, one needs to perform generalized ellipsometry (see e.g., [14,15]) or Mueller matrix ellipsometry. Mueller matrix ellipsometry has a great advantage over generalized ellipsometry, since it also can deal with depolarizing samples, which is not the case for the latter. Depolarization may arise from irregularities in the structure (shape, size, and ordering) and from multiple scattering. If the cones are small enough to be treated by effective medium theory, the structures will have the same effect as layers that are homogeneous in a plane parallel to the surface, and there will be no multiple scattering. When the dimensions of the cones exceed the validity of the effective medium theory, the inhomogeneities will give rise to multiple scattering and depolarization. In this case there will be coupling between the polarization modes even though the structures are rotationally symmetric and point normal to the surface, since the structures no longer can be approximated as an effective homogeneous layer. From this observation, one may conclude whether a given sample can be modeled accurately by effective medium theory from measurements of depolarization alone.

To examine if the samples give polarization coupling, their Mueller matrices measured by MME have been analyzed. If there is no coupling, the Mueller matrix should be block diagonal. We define a measure of the degree of nonblock diagonality as

$$A = \left(\frac{m_{13}^2 + m_{14}^2 + m_{23}^2 + m_{24}^2 + m_{31}^2 + m_{32}^2 + m_{41}^2 + m_{42}^2}{m_{11}^2 + m_{12}^2 + m_{21}^2 + m_{22}^2 + m_{33}^2 + m_{34}^2 + m_{43}^2 + m_{44}^2} \right)^{1/2}, \tag{6}$$

which is 0 for block-diagonal Mueller matrices (such as reflections from isotropic surfaces), and has the value 1 for maximum nonblock-diagonal matrices (such as circular polarizers and ± 45 linear polarizers). Figure 5 shows this quantity as a function of azimuth sample rotation around the mean surface normal for various samples. Additionally, as a reference, a sample with nanostructures sputtered at 45°

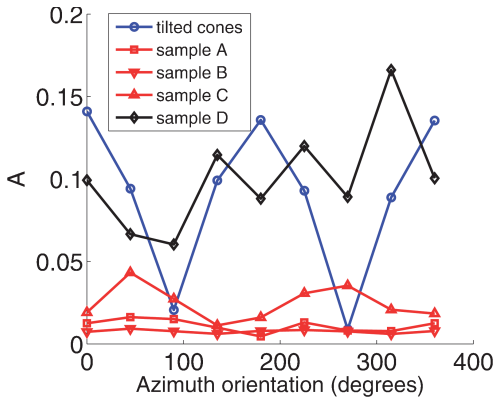

Fig. 5. (Color online) Degree of nonblock diagonality (A, as defined in Eq. (6) for various samples, as a function of azimuth sample rotation, for $E_{ph} = 2.75$ eV. The sample denoted tilted cones consisted of cones tilted 45° from the surface normal (approximately 30 nm high), while the other samples have cones pointing normal to the surface.

of incidence, with an effective layer thickness of approximately 30 nm is also shown [6,16]. This sample consists of cones tilted by approximately 45° from the mean surface normal and has as expected a Mueller matrix that is only block diagonal for azimuthal orientations where the cones lie in the plane of incidence.

Moreover, it is observed from Fig. 5, that the short cone samples have negligible polarization coupling, while the longer cones have substantial deviations from a block-diagonal Mueller matrix. This coupling could, as earlier discussed, be related to a slight tilting of the cones, a long range preferential ordering of the cones, or an anisotropic shape of the individual cones. It is speculated that a long range preferential ordering could be induced by e.g., substrate polishing features. However, for sample D, no azimuthal orientation has been observed to give a block-diagonal Mueller matrix, as should be the case for a thin film with the optic axis in the plane of incidence. This implies that these samples cannot be modeled as an anisotropic thin film layer, and that their optical properties are strongly affected by multiple scattering. Such samples cannot be fully characterized by SE, and full Mueller matrix ellipsometry is instead necessary. Samples A, B, and C only show a slight deviation from block-diagonal Mueller matrices, and these off-diagonal elements will be neglected in the following analysis and modeling. The detailed analysis and modeling of tilted cones will be treated in a separate publication [16].

From the polarization coupling at various azimuth orientations of sample D it was concluded that the polarization altering properties of this sample had contributions from multiple scattering, and that it would not be well approximated as an effective medium. From this conclusion, one would expect the sample to be depolarizing, which is confirmed by the depolarization index (D_P, defined in Eq. (5) evaluated from the MME measurements (Fig. 6). As expected, depolarization increases for increasing photon energy since the effective medium approximation gets less accurate for decreasing wavelengths. In addition, an approximation to depolarization at higher energies has been found by calculating degree of polarization P from the PMSE measurements through Eq. (4). The degree of polarization obtained in this way is a measure of how much certain polarization states are depolarized and will generally differ from the depolarization index, which (in many cases) is the average depolarization of all possible incident polarization states (see Ref. [10]). For samples with block-diagonal Mueller matrices (A, B, C), the degree of polarization can safely be used as a measure of depolarization. It is observed that the short cones have principally low depolarization throughout the measured spectral range (Fig. 6). All the samples studied in the present work show an increasing depolarization towards the UV range. Sample A has a small dip in the degree of polarization at the photon energy where $I_s = 0$ and $I_c = 1$. This effect can be explained

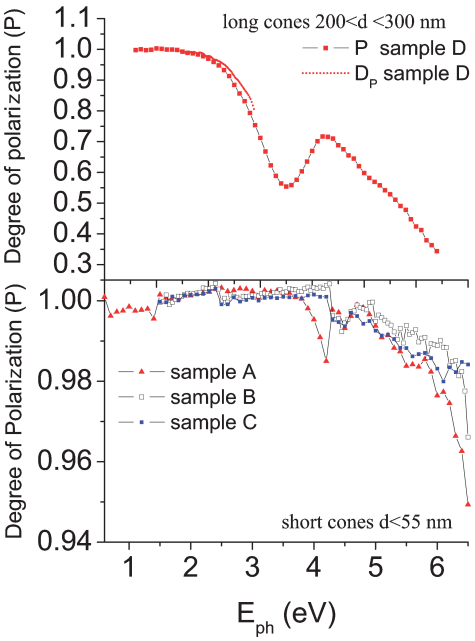

Fig. 6. (Color online) Degree of polarization P, as calculated from the PMSE measurements by Eq. (4), for the nanostructured GaSb samples. The bottom figure shows P for the short cone samples: A, B, and C, while the top figure shows P for the long cones of sample D. The depolarization index D_P, calculated from the Mueller matrix in the visible range, is also shown for the long cones in the top figure.

by a small variation in cone height (thin film thickness) [9] or cone shape. It could also be caused by quasi-monochromatic light from the monochromator. It is especially noted that the dielectric function is descending steeply at this photon energy [17], meaning that a very small wavelength distribution could give depolarization. It is noted that samples B and C show little depolarization in the main part of the spectrum. This does not imply that these samples have less variation in cone height or shape than sample A, since there is no photon energy for which $I_s = 0$ and $I_c = 1$ (see Fig. 3). All the short cones still show a small but observable increasing depolarization for decreasing wavelength. Furthermore, it is observed that degree of polarization P decreases more rapidly as a function of wavelength as the cone height increases.

C. Optical Modeling

Because of the anisotropic shape of the nanostructures, they cannot be modeled by a standard isotropic effective medium theory. The cones with no or little depolarization (short cones) have been modeled as a graded anisotropic thin film layer of effective media on a GaSb substrate. Reflection coefficients have been calculated by an implementation of the Schubert algorithm [18] for reflections from arbitrarily

anisotropic layered systems, based on Berreman 4 × 4 differential matrices [19]. As a first approximation, the cones have been modeled as a stack of cylinders with decreasing diameter. Each cylinder in the stack defines a layer with a homogeneous effective dielectric function. With a sufficient number of layers, this will be a good approximation of a graded thin film layer. Based on HR-TEM observations, we have assumed the cylinders to consist of a core of crystalline GaSb, covered by a coating consisting of a mixture of amorphous GaSb and GaSb oxide. Simpler models consisting only of crystalline GaSb and void have been tested, and were found to not sufficiently explain the measurements. Anisotropy is introduced by using the generalized Bruggeman effective medium theory [20], giving the formula

$$f_{c\text{–GaSb}}\frac{\epsilon_{c\text{–GaSb}}-\epsilon_{ii}}{\epsilon_{ii}+L_i(\epsilon_{c\text{–GaSb}}-\epsilon_{ii})}+f_{\text{coat}}\frac{\epsilon_{\text{coat}}-\epsilon_{ii}}{\epsilon_{ii}+L_i(\epsilon_{\text{coat}}-\epsilon_{ii})}+f_{\text{void}}\frac{\epsilon_{\text{void}}-\epsilon_{ii}}{\epsilon_{ii}+L_i(\epsilon_{\text{void}}-\epsilon_{ii})}=0, \tag{7}$$

where f and ϵ denote the filling factors and complex dielectric functions, respectively, with the subscript c – GaSb referring to the crystalline core, coat to the coating over layer, and void to the surrounding void. L_i denotes the depolarization factor in direction i (along a principal axis of the structure) and ϵ_{ii} is the effective dielectric function in direction i. Our principal axes will be two orthogonal axes parallel to the mean surface, x and y, and a z axis normal to the mean surface. The dielectric function of the coating, ϵ_{coat}, has been determined by letting it be a mixture of amorphous GaSb (a-GaSb) and GaSb oxide (oxide), and using the standard Bruggeman equation for spherical inclusions ($L_i = 1/3$):

$$f_{a\text{–GaSb}}\frac{\epsilon_{a\text{–GaSb}}-\epsilon_{\text{coat}}}{\epsilon_{\text{coat}}+2\epsilon_{a\text{–GaSb}}}+f_{\text{oxide}}\frac{\epsilon_{\text{oxide}}-\epsilon_{\text{coat}}}{\epsilon_{\text{coat}}+2\epsilon_{\text{oxide}}}=0. \tag{8}$$

These cylinders can thus be approximated as an effective thin film layer, which is valid when the distances between neighboring cylinders are much smaller than the wavelength of the light. The layer will be anisotropic, with depolarization factor $L_x = L_y = 0.5$ in the plane parallel to the surface, and $L_z = 0$ in the direction normal to the surface. The reflection coefficients from such an anisotropic layered system have been calculated and used to find the ellipsometric intensities I_s and I_c [8]:

$$I_s = \frac{2\,\text{Im}(r_{pp}r_{ss}^* + r_{ps}r_{sp}^*)}{|r_{ss}|^2+|r_{pp}|^2+|r_{sp}|^2+|r_{ps}|^2}, \tag{9}$$

$$I_c = \frac{2\,\text{Re}(r_{pp}r_{ss}^* + r_{ps}r_{sp}^*)}{|r_{ss}|^2+|r_{pp}|^2+|r_{sp}|^2+|r_{ps}|^2}. \tag{10}$$

The parameters of the models have been fitted to I_s and I_c by minimizing χ^2, defined as

$$\chi^2 = \frac{1}{2N-M+1}\sum_{i=1}^{N}\left[\frac{(I_{si}^{\text{mod}}-I_{si}^{\text{exp}})^2}{\sigma_{si}^2}+\frac{(I_{ci}^{\text{mod}}-I_{ci}^{\text{exp}})^2}{\sigma_{ci}^2}\right], \tag{11}$$

where N and M are the number of measurement points and the number of free parameters in the model, respectively. σ_{si} and σ_{ci} are the standard deviations of the respective measurements. Additional measurements such as any Mueller matrix element, or the reflectance, may be added to the formulae in a similar fashion.

The simplest model giving satisfactory results has been one with 5 parameters (see Fig. 7): total height h; relative (effective) diameters D_1 and D_2 of the bottom and top cylinder cores; thickness of the coating s; and amount of oxide in the coating f_{oxide}. Diameters D_1 and D_2 and thickness s are dimensionless quantities, defined as fractions of the mean nearest neighbor distance of the cones. This distance cannot be found from the optical measurements when the effective medium approximation is valid, since the effective medium only depends on volume filling factors and shape through depolarization factors L_i. This means that the model is independent of the scale in the horizontal plane for all structures sufficiently smaller than the wavelength of light. A stack of $\mathcal{N} = 100$ cylinders of equal height were used to approximate a continuous gradient, with the diameters $d(n)$ of layer n decreasing linearly from D_1 to D_2:

$$d(n) = D_1 - \frac{D_1 - D_2}{\mathcal{N}-1}n, \tag{12}$$

for $n = 0, 1, \ldots, 99$. Assuming a hexagonal ordering of the cylinders, the filling factor of crystalline GaSb and coating become

$$f_{c\text{–GaSb}}(n) = \frac{\pi}{\sqrt{12}}\text{d}^2(n), \tag{13}$$

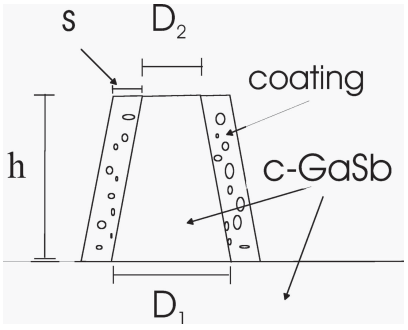

Fig. 7. Parameters used in the graded effective medium model. h is the total height, s is the thickness of the coating of amorphous material and oxide, D_1 and D_2 are the lower and upper diameters of the crystalline core.

$$f_{\text{coat}}(n) = \frac{2\pi}{\sqrt{3}}[\mathrm{d}(n)s + s^2]. \quad (14)$$

Notice that for an effective medium theory it is only the filling factors that play a role, and not the specified ordering of the cones. As long as the filling factors remain the same, effective medium theory cannot distinguish between different geometric arrangements. The distance between the centers of neighboring cones has been set to unit length. The thickness of coating is constant for all layers.

Minimization was performed using the sequential quadratic programming (SQP) algorithm of the Matlab Optimisation Toolbox 3.1.1. The dielectric functions of crystalline GaSb, amorphous GaSb, and GaSb oxide were obtained from the literature [17,21,22]. The standard deviations (noise) σ_{si} and σ_{ci} of the ellipsometric measurements I_s and I_c were estimated to be 0.01.

The modeled ellipsometric intensities are presented together with the measurements in Figs. 8 and 9, with the model parameters given in Table 3. The model gave a good fit to the optical measurements of sample A (Fig. 8), with a cone height of 54 nm and a clear grading in the inner cylinder diameters from $D_1 = 0.55$ to $D_2 = 0.36$. This is in good agreement with the previously presented SEM and TEM images (see Fig. 2). Two simpler models consisting only of crystalline GaSb and void are also shown in Fig. 8: one where the cones are modeled as cylinders, and one where they are modeled as a stack of cylinders with decreasing radius. Niether of them gave a satisfactory result.

Sample C could be well fit by a model with $D_1 \approx D_2$, meaning that it could have been modeled equally well by only one layer of coated cylinders. The cone height was found to be 36 nm. It may be that the optical measurements are not sensitive to a possible gradient in such a short structure, or that the structures have a shape resembling a cylinder.

The ellipsometric measurements of sample B greatly resemble those of sample C but the optical model could not give an equally good fit. When D_1 and D_2 are allowed to vary freely, the model converges to a seemingly unphysical case (based on the TEM, and SEM images) with $D_2 > D_1$. To avoid this problem, they have been constrained so that $D_1 > D_2$. The result is then a cylinder-like model (no grading), with a height of 32 nm. It may appear to be necessary to develop more advanced models to perfectly fit the measurements of this sample. Natural extensions could be to let the coating thickness s vary with height, letting the diameter $d(n)$ of layer n follow a nonlinear function from D_1 to D_2, or by letting the filling factors be able to deviate from values consistent with a hexagonal ordering. We do not, however, treat such advanced models here, but keep the parameters in the models to a minimum for easier interpretation and to avoid unphysical solutions. It is also plausible that the dielectric functions of the different phases mixed in the effective medium theory are somehow different, e.g., that the properties of the oxide are different.

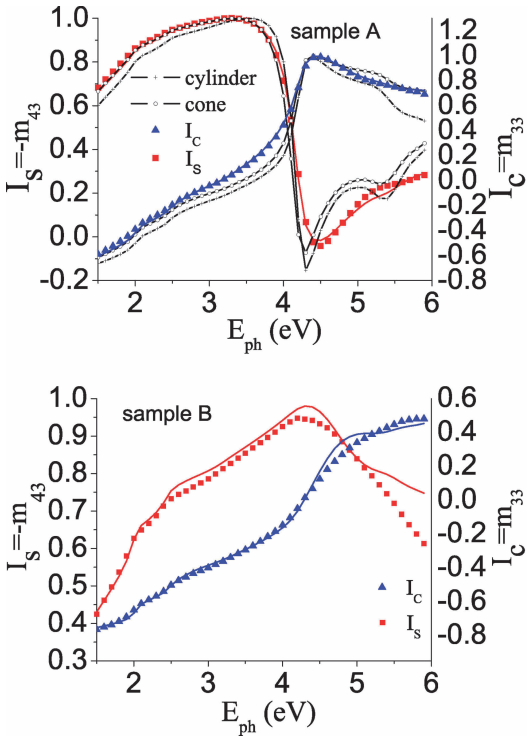

Fig. 8. (Color online) Simulated and experimental ellipsometric intensities $I_s = -m_{43}$ and $I_c = m_{33}$, for sample A (top) and sample B (bottom). The filled squares and filled triangles are the measured I_s and I_c, respectively. The solid lines are the simulated values calculated from the fitted model, with parameters defined in Fig. 7 (sample A: $\chi^2 = 2.6$, sample B: $\chi^2 = 12.4$). For sample A, simpler models with only crystalline material in the effective medium layer have also been included for comparison. The lines marked by crosses (+) are for a model made by treating the cones as cylinders ($\chi^2 = 118$), the lines marked by circles (○) are for a graded model as described in Fig. 7, but with no coating of oxide and amorphous material ($\chi^2 = 61.7$).

Table 3. Resulting Parameters from Fitting the Optical Models to the Ellipsometric Data

Sample Name	h (nm)	D_1	D_2	s	f_{oxide}	χ^2	f_{tot}
A	54	0.55	0.36	0.10	0.56	2.6	0.39
B	32	0.31	0.31	0.21	0.64	12.4	0.46
C	36	0.36	0.35	0.14	0.34	1.1	0.37
D [b]	165	0.95	0.21	0	0.0	7.4	0.34

[a] h is the total height of the model layers, D_1 and D_2 are the bottom and top diameter of the crystalline core, respectively, s is the coating thickness, and f_{oxide} is the amount of oxide in the coating. χ^2 is the square deviation of the modeled ellispometric intensities from the measured, as defined in Eq. (11). D_1, D_2, and s are defined relative to the center to center distance for two nearest neighbors.
[b] Sample D was only curve fitted below 2.5 eV (i.e., for $P > 0.9$).

According to the results from the optical characterization, sample B should consist of slightly shorter cones than sample C. This seems overall consistent with the AFM observations. It has been observed for samples A, C, and D that the nearest neighbor distance increases for increasing cone height (Table 2). From the cone density one should therefore expect sample B to have shorter cones than sample C. The average cone height $\langle h \rangle$ estimated from AFM did not show as clear a difference between the samples, but such small height differences could possibly be masked in the uncertainty in the estimation of $\langle h \rangle$.

The height of the cones of samples B and C obtained from the optical model are lower than the average heights found by AFM. It should be stressed that the heights of sample A (which coincided well with the height from the optical model) were found in a different way (by HR-TEM). As previously mentioned, the average cone height estimated from AFM measurements may be exaggerated. The model appears to be very sensitive to changes in the thickness of the effective medium layer, a perturbation in thickness of only a few nm results in a large increase of χ^2. However, different models may result in different layer thicknesses. For instance, it may seem more reasonable to let the cones be covered by a coating of thickness s also on the top. This has been tested and resulted in equally good χ^2 values as the models reported in Table 3 but with total heights 4–5 nm higher. The problem with such a model is that the thickness of the coating top layer has to be determined absolutely, not just as a ratio, s, of the nearest neighbor distance. This distance cannot be obtained from SE measurements but must be found from e.g., AFM or SEM studies. We are interested in a model that can help us characterize the nanostructures from SE measurements alone, and therefore reject this model with a coating also on the top.

The total volume filling factors for the optical models are tabulated in the last column of Table 3. For ideal cones, ordered in a hexagonal lattice, the maximal filling factor is 0.30. The model filling factors lie in the range 0.34–0.46, in good correspondence to the rounded conical structures observed from TEM, SEM, and AFM measurements (rounded cones will give a larger filling factor than cones with a sharp top). Exact estimation of filling factors from microscopy images proved to be difficult. The varying shape and size of the individual cones must be taken into account, together with the mean nearest neighbor distance. The AFM measurements should in principle be ideal for this, but because of a too blunt tip and holes in the surface, they drastically overestimate the filling factors. By estimating the shape and size of an individual cone from a TEM image, and using the mean nearest neighbor distance from AFM measurements, a rough estimation of the filling factor of sample A was found to be 0.36 ± 0.04, in reasonable agreement with the value from the optical model (0.39).

The construction of an effective medium optical model, predicts structural parameters that correspond reasonably well to the physical height of the samples, and the density/shape of the cones. Equally important, the models can by used to predict optical properties not measured. The model of sample A, calibrated by SE measurements at 55° angle of incidence, were used to successfully predict results of SE measurements at 70° angle of incidence. The models may also predict the reflectance (R_{ss}, R_{pp}, or R) of the samples (see Fig. 9). We propose that the models can be used as a tool to calculate the polarization dependent optical properties of such samples at any angle of incidence.

The large depolarizing properties of sample D indicate that it may not be modeled appropriately by effective medium theory over the full spectral range considered. The experimental observations represent an interesting case, in the sense that there are no commonly available models to appropriately fit these data. A tentative effective medium modeling between 0.6 and 2.5 eV was tested to extract

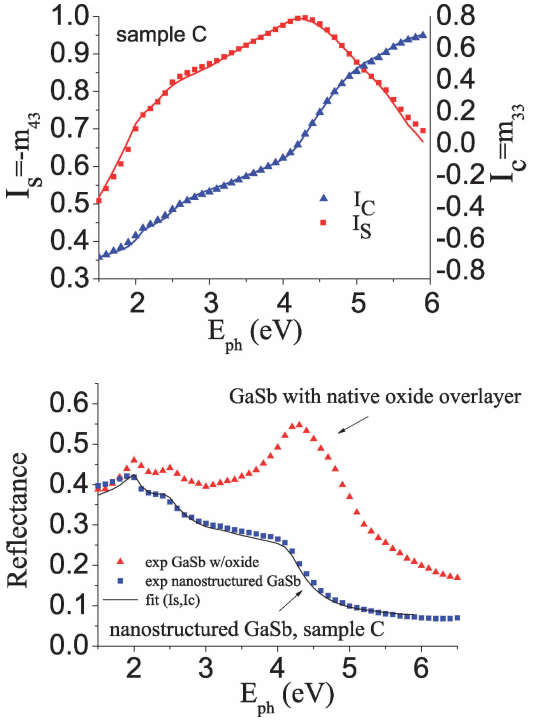

Fig. 9. (Color online) Simulated and experimental ellipsometric intensities $I_s = -m_{43}$ and $I_c = m_{33}$, for sample C (top). The filled squares and filled triangles are the measured I_s and I_c, respectively. The solid lines are the simulated values calculated from the fitted model, with parameters defined in Fig. 7 (sample C: $\chi^2 = 1.1$). The bottom figure depicts the measured reflectance $R = (|r_{ss}|^2 + |r_{pp}|^2)/2$ [filled squares for sample C, filled triangles for GaSb with native oxide layer)], and simulated reflectance, calculated from the fitted model.

approximately the cone height of sample D. It was found to be 165 nm, about half of the height found by SEM but still considerably higher than heights found for the short cones and with a clear gradient. The dielectric function data for GaSb oxide and c-GaSb in the photon energy range 0.6–1.5 eV were not available in the literature and were, therefore, extrapolated from PMSE measurements at 70° angle of incidence. The parameters of the resulting model are tabulated for completeness. Improved optical models suitable for modeling of the optical response of these samples are currently being undertaken and planned for future work.

4. Summary and Conclusions

Spectroscopic ellipsometry and Mueller matrix ellipsometry have been shown to be useful techniques for the characterization of nanostructured surfaces, such as nanocones of GaSb on GaSb. Overall, the observations from SE appear to be consistent with the results from SEM, TEM, and AFM studies. An optical model has been found to fit well to the measurements obtained for short cones (of height 55 nm and lower). This was achieved by treating the structures as a graded anisotropic thin film of effective medium. These models have been applied to obtain an approximation to the average cone height of the samples and also, to some extent, to gain information on the cone shape. They may also be used to estimate reflectance and polarization altering properties for reflections at any angle of incidence. The nanostructuration of the surface was shown to considerably reduce the reflectance. The antireflecting properties increased with cone height. Samples with long nanocones (200–300 nm) were found to be strongly depolarizing and could not be modeled as an effective medium. The full Mueller matrix must be measured to fully characterize the polarization altering properties of such samples. We have demonstrated that SE can be a fast and nondestructive way of characterizing nanocones of GaSb with the possibilities of *in situ* control under production.

The authors are grateful to M. Stchakovsky at Horiba Jobin Yvon for access to scientific instruments, and Susanne W. Hagen at NTNU for doing complementary measurements.

References

1. M. Born and E. Wolf, *Principles of Optics. Electromagnetic Theory of Propagation, Interference and Diffraction of Light*, 6th corrected ed. (Pergamon, 1980).
2. G. Beydaghyan, C. Buzea, Y. Cui, C. Elliott, and K. Robbie, "*Ex situ* ellipsometric investigation of nanocolumns inclination angle of obliquely evaporated silicon thin films," Appl. Phys. Lett. **87**, 153103 (2005).
3. Z. P. Yang, L. Ci, J. A. Bur, S. Y. Lin, and P. M. Ajayan, "Experimental observation of an extremely dark material made by a low-density nanotube array," Nano Lett. **8**, 446–451 (2008).
4. S. Facsko, T. Dekorsy, C. Koerdt, C. Trappe, H. Kurz, A. Vogt, and H. L. Hartnagel, "Formation of ordered nanoscale semiconductor dots by ion sputtering," Science **285**, 1551–1553 (1999).
5. N. Brun, A. Lelarge, S. Le Roy, E. Søndergård, and E. Barthel are preparing a manuscript to be called "Composition of nanostructured GaSb."
6. M. Kildemo, I. S. Nerbø, E. Søndergård, L. Holt, I. Simonsen, and M. Stachakovsky, "Optical response of nanostructured gasb," Phys. Stat. Sol C **5**, 1382–1385 (2008).
7. B. Drévillon, "Phase modulated ellipsometry from the ultraviolet to the infrared: *in situ* applications to the growth of semiconductors," Prog. Cryst. Growth Charact. **27**, 1–87 (1993).
8. P. Hauge, "Conventions and formulas for using the Mueller–Stokes calculus in ellipsometry," Surf. Sci. **96**, 81–107 (1980).
9. G. E. Jellison, Jr. and J. W. McCamy, "Sample depolarization effects from thin films of ZnS on GaAs as measured by spectroscopic ellipsometry," Appl. Phys. Lett. **61**, 512–514 (1992).
10. R. A. Chipman, "Depolarization index and the average degree of polarization," Appl. Opt. **44**, 2490–2495 (2005).
11. D. Weaire and N. Rivier, "Soap, cells and statistics—random patterns in two dimensions," Contemp. Phys. **25**, 59–99 (1984).
12. C. G. Bernhard, "Structural and functional adaptation in a visual system," Endeavour **26**, 79–84 (1967).
13. R. M. A. Azzam and N. M. Bashara, *Ellipsometry and Polarized Light* (North-Holland, 1987).
14. G. E. Jellison and F. A. Modine, "Two-modulator generalized ellipsometry: theory," Appl. Opt. **36**, 8190–8198 (1997).
15. A. Laskarakis, S. Logothetidis, E. Pavlopoulou, and M. Gioti, "Mueller matrix spectroscopic ellipsometry: formulation and application," Thin Solid Films **455–456**, 43–49 (2004).
16. I. S. Nerbø, M. Kildemo, S. W. Hagen, S. Leroy, and E. Søndergård, "Optical properties and characterization of tilted gasb nanocones," (to be published).
17. D. E. Aspnes and A. A. Studna, "Dielectric functions and optical parameters of Si, Ge, GaP, GaAs, GaSb, InP, InAs, and InSb from 1.5 to 6.0 ev," Phys. Rev. B **27**, 985–1009 (1983).
18. M. Schubert, "Polarization-dependent optical parameters of arbitrarily anisotropic homogeneous layered systems," Phys. Rev. B **53**, 4265–4274 (1996).
19. D. W. Berreman, "Optics in stratified and anisotropic media: 4 × 4 matrix formulation," J. Opt. Soc. Am. **62**, 502–510 (1972).
20. J. E. Spanier and I. P. Herman, "Use of hybrid phenomenological and statistical effective-medium theories of dielectric functions to model the infrared reflectance of porous sic films," Phys. Rev. B **61**, 10437–10450 (2000).
21. J. Stuke and G. Zimmerer, "Optical properties of amorphous iii-v compounds. i. Experiment," Phys. Stat. Sol. B **49**, 513–523 (1972).
22. S. Zollner, "Model dielectric functions for native oxides on compound semiconductors," Appl. Phys. Lett. **63**, 2523–2524 (1993).

Real-time in situ spectroscopic ellipsometry of GaSb nanostructures during sputtering

Paper II

Is not included due to copyright

Characterization of inclined GaSb nanopillars by Mueller matrix ellipsometry

Paper III

Is not included due to copyright

In-situ and real time study of the formation of nanopatterns on GaSb by ion abrasion

Paper IV

In-situ and real time study of the formation of nanopatterns on GaSb by ion abrasion

S. Le Roy and E. Søndergård*

Surface du Verre et Interfaces, UMR 125 CNRS/Saint-Gobain, 93303 Aubervilliers, France,

I. S. Nerbø and M. Kildemo

Physics Department, Norwegian University of Science and Technology (NTNU) NO-7491 Norway

(Dated: June 10, 2011)

Abstract

We present an extensive real time and *in situ* investigation of the formation of nanopatterns on GaSb induced by ion abrasion using Spectrometric Ellipsometry, complemented by *ex situ* Atomic Force Microscopy and Scanning Electron Microscopy. The influence of the ion beam energy, flux and incident angle on the pattern formation is discussed. All experimental conditions lead to a formation rate exhibiting two or three distinct regimes. Normalization with the flux rate makes the data fall on the same master curve. The flux appears to set the time scale for the temporal evolution of the amplitude of the patterns. The ion energy and the substrate temperature mainly determine the absolute values of the pattern amplitude. The lateral length scale of the patterns show a linear behavior with energy and a weak dependence on the flux. Furthermore, a first investigation of the formation rate for oblique ion incidence is presented. The overall behavior is similar to the one at normal ion incidence. However, the formation rate is enhanced with respect to sputtering at normal incidence beyond what can be predicted from the angular dependence of the yield. These results cannot be understood using the classical Bradley Harper theory for ion patterning. Adversely, the recently proposed Self-Sustained Etch Masking model provides a good framework allowing for a clear interpretation of most of the data. This confirms that the instability behind the pattern formation process on GaSb is linked to the thermodynamic properties of the material rather than a curvature dependent sputtering yield previously suggested.

PACS numbers: 79.20.Rf, 81.16.Rf, 64.75.St

INTRODUCTION

Under certain circumstances ion beam sputtering of flat surfaces can lead to the spontaneous formation of nanoscale patterns. This phenomena could open alternative ways to control the surface roughness of functional materials with tailored properties in the field of microfluidics, optics or self-cleaning surfaces. Since the pioneering works of Navez [1] and Bradley Harper [2] the phenomenon of ion pattering has been investigated on several materials like SiO_2 [3], Si [4–7] and Ge [8, 9] where ripple patterns were found. One exciting fundamental question is which kind of patterns ion induced erosion instabilities can render. In the last decade significant insight has been gained on the possible morphologies on monoatomic materials. Quantitative models have been proposed to describe the influence of experimental parameters like ion energy, ion incidence and substrate temperature on the characteristic features of the patterns as well as the coupling to surface kinetics like diffusion constants and barriers [10, 11].

The works of Fascko *et al* [12] and Yuba *et al* [13] revealed that ion beam sputtering can also lead to the formation of a distinct type of patterns on III-V semiconductors like GaSb. These materials form dot or pillar patterns instead of ripples and GaSb is considered to be the most prominent example. Since, there have been several attempts to explain the pattern formation on GaSb in the framework of the Bradley Harper (BH) model [14, 15] where the considered driving mechanism is the curvature dependent abrasion yield. However, the BH based models fail to describe the most distinct features of the patterns on GaSb [16]. Lately, it was demonstrated that sputtering on GaSb leads to considerable chemical inhomogeneity in the surface region and in the pattern protrusions. This phenomena spurred the alternative explanation that the dominant surface instability was induced by segregated gallium droplets masking the impacting ions [16]. This kind of surface patterning mechanism during ion abrasion was named Self-Sustained Etch Masking, referring to the materials capacity to stabilize the mask against erosion through a continuous diffusion process. The driving mechanism was suggested to be the creation of a slight excess of Ga in the surface region perturbed by the ions leading to segregation of gallium in the GaSb. Lately, a phenomenological diffuse interface model succeeded in a mathematical description of this concept and in reproducing the characteristic patterns obtained on III-V semiconductors [17].

To study the evolution of the morphology during sputtering, most authors have been doing sequential observations by successive series of abrasion and *ex situ* investigations to characterize the lateral sizes and amplitudes. The used techniques were often Atomic Force Microscopy (AFM) or Scanning Electron microscopy (SEM). It is a time consuming method which is hampered by both tip effects and the accumulation of uncertainties in the experimental conditions. Due to this there is a lack of quantitative studies on the pattern formation on GaSb and contradictory results are reported. Ziberi *et al* evidenced that the morphology is heavily dependent on the experimental conditions in Ref. [18]. Other authors [19, 20] investigated the temporal evolution of low amplitude patterns obtained at low temperature. They observed an initial growth stage, followed by a saturation and decrease to a constant roughness. Refs. [12, 20] both showed a significant coarsening of the lateral size of the patterns during abrasion. On the contrary, other authors noticed little temporal evolution in the lateral size once the pattern had formed [13, 19]. A similar result was reported in the only published *in situ* study by grazing incidence X-ray scattering (GISAXS) [21] on the evolution of the pattern wavelength.

In a recent publication, we showed that Spectroscopic Ellipsometry (SE) can be used to follow the evolution of the pattern amplitude on GaSb *in situ*, see [22]. In contradiction with previous *ex situ* studies, three growth regimes were identified and none of them showed evidence for saturation. In the present paper, we present the first extensive investigation on the formation of nanostructures on GaSb using SE measurements combined with SEM and AFM for a broad range of ion abrasion parameters. The influence of both the temperature and the ion incidence on the pattern formation is also investigated. We show that the data can be understood in the framework of the Self-Sustained Etch Masking model and that independent control of the lateral length scale and amplitude is feasible.

EXPERIMENTS

Clean crystalline (100) GaSb surfaces were exposed to a Ar^+ ion beam in a UHV vacuum chamber with $5 \cdot 10^{-8}$ mbar base pressure and a $6 \cdot 10^{-4}$ mbar working pressure. We used a commercially available plasma source (Tectra Gen2), with the ion energy ranging from 200 to 500 eV and a flux from 0.12 to 0.3 mA/cm^2.

A SE instrument (MM16, Horiba Jobin Yvon) with a charged-coupled device (CCD)

based spectrograph (spectral range 1.46–2.88 eV) was used to do *in situ* measurements during sputtering. The ellipsometer was mounted on two low-strain optical windows (Horiba Jobin Yvon) on the UHV chamber, giving optical access to the samples during sputtering. For samples sputtered with the ion incidence parallel to the substrate normal, the incident angle, θ_i, of the optical beam was 45° with respect to the normal. For samples sputtered with an oblique ion incidence of 22.5°, an optical angle of incidence $\theta_i = 67.5°$ was used. Full Mueller matrix ellipsometric data were recorded every 5th second during sputtering. Further details on the set-up can be found in the Ref. [22].

AFM measurements were done using the tapping mode of a Nanoscope IIIA instrument from Veeco. The Si cantilevers used for the observations had a radius of curvature inferior to 10 nm and a spring constant of 40 N/m (supplier NanoAndMore). Typical scan lengths were 1 to 4 μm with a resolution of 512 points per line. SEM measurements were done in a Field Emission SEM (Zeiss Ultra 55) without metallization of the surface. After mechanical cleavage, cross-section images were taken of the samples at an angle of 45°.

The samples were mounted on a heatable sample stage equipped with a thermocouple. A first series of samples, A, was produced in order to do a sequential investigation of the evolution of the pattern morphology at various energies. Samples were sputtered at the energy of 300, 400 and 500 eV during intervals of 10 to 1800 s. The flux was 0.17 mAcm^{-2} for the samples made at 300 and 400 eV. Due to the increase in the extraction efficiency of the ion gun the flux was 0.24 mAcm^{-2} for samples obtained at 500 eV. An additional sample was sputtered at the energy of 200 eV, a flux of 0.17 mAcm^{-2} and the duration of 900 s. These samples were all observed by AFM or SEM.

A second series of samples, B, concerned the *in situ* observations. Energies ranging from 200 to 500 eV and fluxes from 0.12 to 0.3 mAcm^{-2} were investigated at 0° (normal ion incidence) and 22.5°. The extraction efficiency of the ion gun vary with the ion energy and therefore the highest energy used could not be stabilized for a low flux. Consequently, the full range of energies could not be reached with a constant flux. After the *in situ* observation, AFM observations were carried out on the final samples sputtered at normal incidence. When possible the inclined structures were characterized by SEM.

In a third series, C, the substrate temperature ranged between 20-300 °C with the constant flux 0.17 mAcm^{-2}, an ion beam energy of 300 eV and normal incidence. After sputtering, the surface morphology was characterized *ex situ* by AFM and SEM.

RESULTS

After ion bean sputtering the sample surfaces were covered by a homogenous pattern of closed packed cones, as reported in [12] with the out of plane angle aligned along the ion incidence [16]. In the following, the morphology of the patterns will be characterized through the two parameters: H and L. The mean height, H, of the patterns, was either extracted from ellipsometric data or by AFM data as described in [22]. The mean distance between neighboring cones, L, is is calculated using a Voronoï tessellation on the position of the tips found by AFM imaging.

Fig. 1 shows the final morphology of sample series A at the ion beam energies of 200, 300 and 400 eV and a constant flux of 0.17 mAcm^{-2} and an exposure time of 900 s. An additional sample is showed for the energy of 500 eV with a flux of 0.24 mAcm^{-2} and the exposure time at 300 s (as longer exposure times leads to pattern amplitudes, H, too high for AFM observation). The trend is that increasing energy increases the scale of H. Fig. 2 shows the temporal evolution of L at different energies extracted from AFM data from sample series A. Clearly, L, depends on the energy and for the samples made at 300 and 400 eV a rapid saturation is observed. Samples made at 500 eV indicates the existence of an initial coarsening regime. However, even if a clear slowdown of the growth of L is observed after 200 s ion exposure, it is not possible to conclude on the existence of a saturation for these experimental conditions.

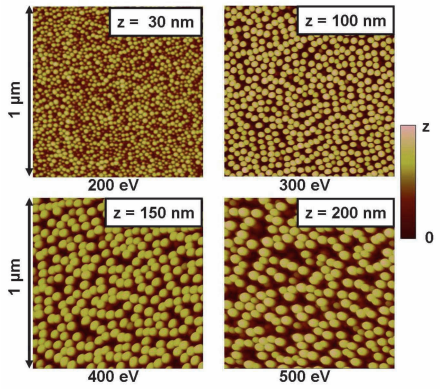

FIG. 1: Results from sample series A. AFM images of surfaces sputtered with various ion energies. The flux was 0.24 mA/cm^2 for the ion energy of 500 eV, and 0.17 mA/cm^2 for the ion energy of 400, 300 or 200 eV. The sputtering time was 900 s, except for the energy of 500 eV where it was 300 s

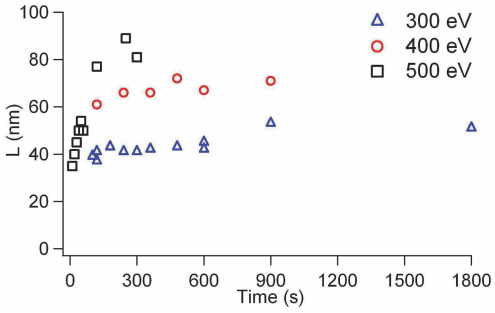

FIG. 2: Results from sample series A. Time evolution of the lateral size L for samples sputtered at 400, 300 or 200 eV. This parameter is found from *ex-situ* AFM images.

Fig. 3 shows the final morphology observed by AFM of various samples sputtered for 900 s with the ion beam energy of 400 eV and a flux of 0.15, 0.17, 0.24 or 0.3 mAcm^{-2}. The apparent influence of the flux is less pronounced than the influence of the ion energy - only a very modest increase of L and H can be identified.

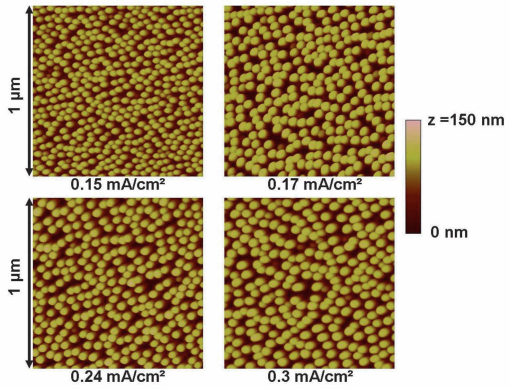

FIG. 3: Data from sample series B. AFM image of samples sputtered with a ion energy of 400 eV and various flux. Every sample is sputtered 900 s.

To access the evolution of the morphology *in situ* the optical data from sample series B was treated by a dedicated effective medium model previously introduced in refs. [22, 23]. Recently, this model was successfully extended to handle anisotropic patterns obtained by sputtering with inclined ion incidence [24]. Due to the effective medium approach the model is valid for surface profiles with a mean height, H, below 100 nm. For rougher surface profiles the model breaks down. The optical data treatment is discussed further in the Appendix.

Figs. 4 a, b and c show the time evolution of H for different energies and a flux of 0.12, 0.17 and 0.24 mAcm^{-2}, respectively. The curves show a similar shape: first, an initial decrease of the surface height is observed, then follows a rapid and approximately linear height evolution. Finally, the growth of H slows down at a pace depending on the experimental conditions. The three described regimes are indicated by the gray dotted vertical lines for the sample sputtered at 300 eV in Fig. 4a. A clear mathematical definition of the regimes is not feasible. However, the first regime ends when H starts to grow while the transition between the second and third regimes is more subtle as it corresponds to a more or less progressive change in the growth rate.

For a constant flux, the two first regimes appear to superimpose even if the duration of the second regime increase with increasing ion energy, see Fig. 4a,b and c. Clearly, the growth rate in the third regime is also influenced by a change in ion energy, as seen on Fig. 4b and c. It was not possible to observe the third regime for the highest ion energies because

the SE characterization method is limited to structures below 100 nm in height, as seen on Fig. 4c, where the second regime appears to extend beyond $H = 100$ nm.

Fig. 4d shows the final value of L found at the end of each each experiment from AFM images. It is interesting to notice a nearly linear behavior of L with increasing energy.

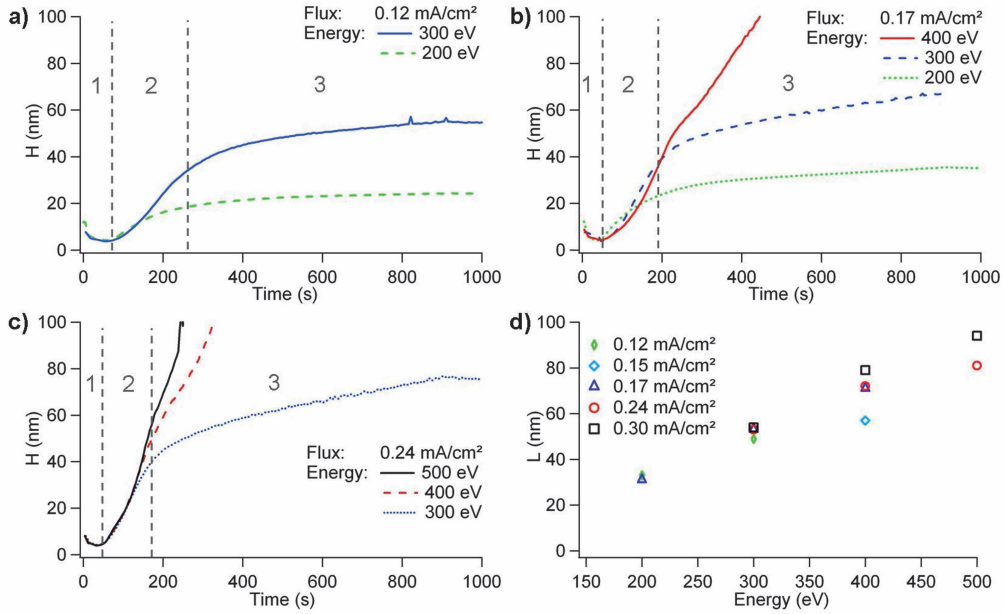

FIG. 4: *In situ* observations of the surface on samples from series B: a) b) c) Temporal evolution of the height, H, for various ion energies and a flux of respectively 0.12 mAcm^{-2}, 0.17 mAcm^{-2} and 0.24 mAcm^{-2}. The gray dotted lines indicate the three regimes for samples sputtered at 300 eV d) Evolution of L with changing energy. The different symbols corresponds to experiments at different flux.

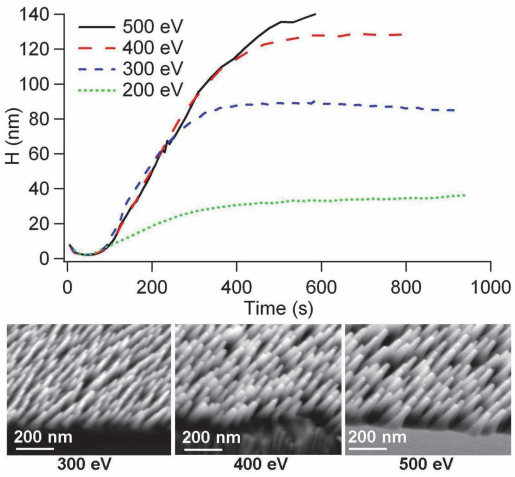

FIG. 5: Data from samples series B. Growth law with an ion incidence angle of 22.5° with constant flux (time is scaled for curve 500 eV). The SEM images show the 45° view of a cross-section of three samples prepared at 300 eV (left), 400 eV (middle) and 500 eV (right)

Fig. 5 shows the time dependence of the height, H, for oblique incidence sputtering at the different ion beam energies 200, 300, 400 and 500 eV. The flux was 0.24 mAcm^{-2} for 500 eV or 0.17 mAcm^{-2} for the other energies. In this specific case, H, represents the the projected amplitude of the patterns along the sample normal. To compare the data the timescale was normalized on the curve for 500 eV by the flux ratio to the curve at 200 eV. The data is strikingly similar to the one obtained for normal incidence showing the same three distinct regimes. As in the previous case the two first regimes overlaps while the third depends on energy. Beyond $H=$ 100 nm the measurement are hampered by higher uncertainties due to the limitation in the optical model (see Appendix). However, the relative evolution of H still corresponds to a physical reality. It worth noticing that the saturation of the growth rate in the third regime is observed for all energies for inclined ion incidence. Another interesting point is that the growth rate in the second regime is much faster than the one found for normal incidence in the same experimental conditions (see Figs. 4b and Fig. 5). The increase of the growth rate goes beyond what can be predicted from the angular dependence of the Sigmund yield law [25]. Cross-section SEM images show that the cones are pointing in the direction of incidence of the ion beam. Even if quantification is difficult, the images

indicate that the lateral size is also increasing with energy.

Figs. 6a, b and c show the evolution of H for different fluxes and an energy of 200, 300 and 400 eV respectively. The flux appears to have a smaller effect on the growth rate than the ion energy. However, once again, all the curves have a similar shape showing three regimes. Fig. 6d show the variation of L with the flux. High energy series show a small tendency for L to increase with increasing flux. The inserts in Figs. 6a, b and c depict the same data but normalized with the flux rate using the lowest value of flux as a reference. The data fall on the same curve.

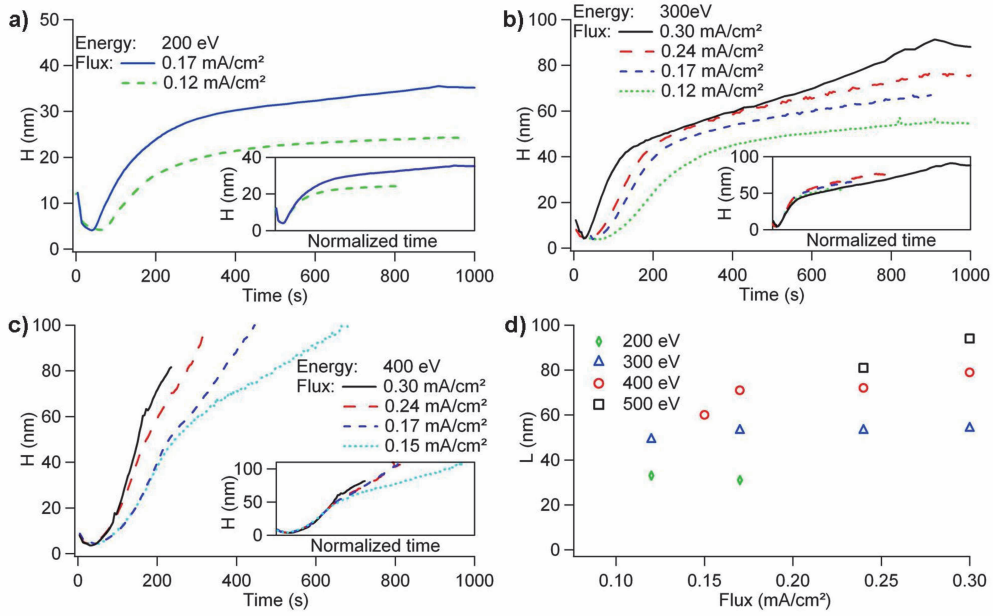

FIG. 6: Data from samples series B. Time evolution of H for various flux and ion energies. a) 200 eV b) 300 eV c) 400 eV. On the insets the timescale is normalized using the flux ratio. d) Evolution of L with the flux at energies between 200 to 500 eV, the symbols corresponds to different values of the ion energy.

The effect of the temperature on the patterning is shown on Fig. 7 with the temporal evolution of H for samples sputtered at an energy of 300 eV, a flux of 0.17 mAcm^{-2} and a temperature of 30, 150 or 300 °C respectively. Increasing the temperature increases the growth rate in the third regime. The lateral sizes L also show a significant increase from 53 nm at 30 °C, 68 nm at 150°C to 130 nm at 300°C.

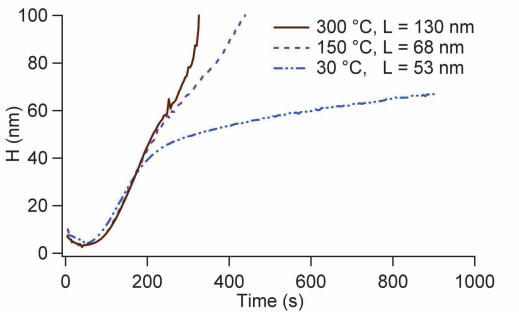

FIG. 7: Results from samples series C. Growth law with a flux of 0.17 mA/cm^{-2} and a energy of 300 eV for various temperatures

Fig. 8 a shows an AFM image of a sample sputtered at 150°C. Similarly Fig. 8 b depicts a SEM image of the surface sputtered at 300° C at the observation angle of 45°. Clearly, the surface morphology is less defined at high temperatures and differs from the geometry used in the ellipsometric model. Even if this can lead to a higher error on the value of H, it will not significantly change the data depicted in Fig. 7 as it is an indication of the evolution of the mean values of the pattern amplitudes.

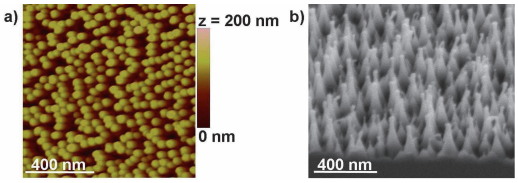

FIG. 8: Results from sample Series C. a) AFM image of samples sputtered at 150°C. b) SEM image of sample sputtered at 300°C

DISCUSSION

The existence of three formation regimes was already reported for a single set of experimental conditions in [17, 22]. However, the data depicted in Figs. 4 - 7 are the first extensive *in situ* studies of the influence of the temperature, flux and energy on the ion induced patterning process on GaSb. Clearly, we observe that the overall behavior is the same whatever the ion beam parameters and the temperature. Strikingly, even the change

of ion incidence proves to have a moderate effect on the overall formation laws, see Fig. 5. These results strongly evidence that the phenomenon behind the formation of patterns on GaSb is universal and robust. However, it is also obvious that the framework of the curvature dependent BH models [2] can not account for these results. First, an initial coarsening regime is observed for L before any significant increase of the mean height H (see Figs. 2 and 4) and Ref. [21]. The BH model predicts, as any other linear model, pattern formation at a constant wavelength. A recent nonlinear extension of the BH model introduces redepositing effects linked to the local geometry to obtain coarsening [15]. However, the coarsening arising from the nonlinear terms are predominant at late stage growth in contradiction with the present experimental results. Secondly, the temperature dependence we observe is opposite to the one predicted by any BH based model where increased diffusion leads to surface relaxation at high temperatures. Finally, the two first formation regimes show a dependence of L on energy and temperature whereas the growth rates of H remain the same. Even nonlinear versions of the BH model can not account for such a behavior.

Due to the mentioned shortcomings of the BH based models we will consider our data in the light of our recent publication suggesting that self-organized nanopatterning on III-V semiconductors can be induced by segregation and continuous masking during ion abrasion [16]. The new mechanism specifically concerns pattern formation on compounds. The main aspects of the so called Self-Sustained Etch Masking model are the following: The higher abrasion yield of one element leads to an enrichment in the surface region of the material of the other element. The tendency of the element to segregate, when in excess, spurs the nucleation of a droplet pattern at the surface. The droplets act as a shield against etching and onset the pattern formation. The continuous erosion of the unprotected material induces a flux of the excess element towards the droplets, compensating for the erosion of the mask. In the case of GaSb, gallium was shown to constitute the mask. The rapid diffusion of this element was suggested to be responsible for the erosion resistance of the mask giving rise to high aspect ratio patterns. A series of equations were proposed to describe the pattern formation stemming from this kind of surface instability reproducing the three observed formation regimes [17]. The mechanisms behind the three regimes were described as the surface enrichment in Ga and the formation of a mask, transfer of the mask into the substrate and finally a slow down of the transfer due to the progressive erosion of the mask when not fully compensated by a resupply of Ga from the substrate. In the following we show that a

large part of the experimental data can be rationalized within this framework.

During the first regime a decrease of the surface roughness is observed. This was also reported in the only other *in situ* study of the lateral length scales [26]. This can be understood as a decaping of the native oxide layer as well as the creation of a damage layer due to the ion impact. A optical model was developed to extract more information in this regime from ellipsometry. Instead of describing the surface as an graded anisotropic layer it was modeled as three isotropic layers, with the top layer being oxidized GaSb, followed a rough amorphous GaSb layer, an amorphous GaSb layer, on top of a crystalline substrate. The rough layer was modeled as an isotropic Bruggeman effective medium consisting of 50% amorphous GaSb and 50% void. The thickness of each layer was found by fitting the model to the SE measurements.

Fig. 9b depicts the evolution of the thickness of the oxide layer as well as the amorphous and rough GaSb layer for ion energies of 300, 400 and 500 eV. The oxide layer is rapidly removed while the thickness of the damage layer increases before stabilizing to a finite value depending on the ion energy. It is well known that GaSb is easily amorphised under ion abrasion [27]. The damaged layer thickness can be interpreted as the mean penetration depth of the collision cascade induced by the ion impact. The obtained values of 10 nm at 500 eV, 8 nm at 400 eV and 6 nm at 300 eV agree well with those estimated using Stopping and Range In Compounds calculations (SRIM) [28]. The initial roughness is found to decrease during a time interval close to the values obtained using the optical model developed to extract the mean cone height, described in ref. [22, 23] and the appendix.

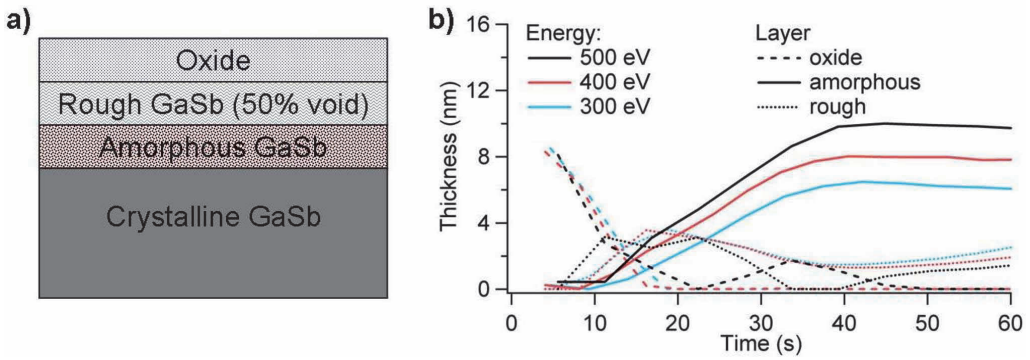

FIG. 9: a) Optical model for the first regime: The surface is described as a layer of oxidized GaSb, a layer of rough amorphous GaSb, a damage layer of amorphous GaSb followed by semi-infinite crystalline bulk GaSb. b) Time evolution of the thickness of the different layers extracted from the data on sample series B. The slanted lines corresponds to the oxide layer, the dotted lines to the rough surface layer and the continuous line to the amorphous layer. Blue, red and black colors corresponds to data obtained at 300, 400 and 500 eV, respectively.

Previous X-ray Photoemission spectroscopy showed an important enrichment of the Ga at the surface during the first regime [16]. We have not been able to observe this by SE.

The origin of the change in the surface composition is the difference of yield between Ga and Sb, and therefore the enrichment speed should be proportional to the flux. Once the composition reach a critical value, phase separation occurs and trigger the second regime. All the phenomena we considered during the first regime (*i.e* oxide removal, surface enrichment and amorphisation) are proportional to the flux. This is clearly supported by the experimental data. The initial regimes superimpose when the flux is constant independently of temperature and energy, see Figs. 4, 5 and 7. Furthermore, when the flux differs, a master curve can be obtained by normalization of the time scale by a flux ratio, see Fig. 6 inserts.

In the second regime, the dominant mechanism for the pattern growth is proposed to be shielding of the substrate by Ga droplets. In consequence, the growth rate should be equal to the difference in sputtering speed between Ga and GaSb. We observe a linear law with a slope corresponding to a yield difference between Ga and GaSb of 0.9 ± 0.1 atoms per incident Ar ion. This is the order of magnitude which can be estimated by SRIM

calculations. If a simple transfer mechanism is at stake in the second regime the growth rate should be proportional to the flux. This is what we observe when normalizing the time scale with the flux for different values of ion energy and substrate temperature. The curves for the second regimes falls onto the same master curve as shown in the inserts on Fig. 6. The duration of the regimes, however, appears to depend heavily on both temperature and ion energy. For high energies and temperatures the second regime is maintained beyond the optical observation limit, see Figs. 4 c and 7. This can be interpreted as the consequence of an increased activation of the Ga mobility leading to an efficient shielding of the Ga cap for an extended period.

The lateral length L of the pattern increases with both enhanced temperature and energy. The coarsening of L stops during the second regime, see Fig. 2. The key parameter for the formation and the coalescence of droplets is the Ga mobility. Obviously, this parameter is strongly influenced by the temperature. Furthermore, increasing ion energy enhances the energy transfer through the collision cascade leading to a higher mobility in the damage layer. However, the transfer of the pattern into the substrate will limit coarsening explaining the fast saturation of L during the second regime. The moderate impact of the flux on L can be understood by a change in the surface temperature due to thermalization.

From our data it appears that the third regime is characterized by a slowdown of the formation rate without a clear saturation whatever the experimental conditions of the flux, the temperature, the ion energy and ion incidence. Both the crossover time between the second and third regimes and the growth rate clearly depends on an interplay between energy, temperature and flux. The third regime has been proposed to be caused by the wear-out of the shielding Ga cap due to a slow down in Ga supply as H increases and the pristine GaSb substrate is further away i.e. a partial shielding regime. It results in a reduced efficiency of the sputter shield and a slower growth rate [17]. The suggested mechanism for the third regime appears to be in good agreement with the data even if a universal law can not be extracted from the present data. Obviously, higher temperatures or energies will enhance the mobility leading to faster coarsening and a more effective shielding for a longer duration. As a consequence both L and H will take larger values. Nevertheless, the details in the interplay of the different parameters will have to be addressed by numerical simulations as no clear trend emerges from the data.

Other groups have also observed the time dependence of H and they report an initial

exponential regime followed by a saturation regime and ending with a decrease [19, 29]. The previously published data was obtained using sequential AFM measurements leading to substantial uncertainties as well as limited statistics. We were never able to evidence such a behavior using either AFM or SE measurements. It is possible that the previously reported results correspond to low mobility conditions where the Self-Sustained Etch Masking mechanism only appears in the partial regime and for a short duration. It would certainly be interesting to obtain *in situ* formation rates in similar experimental conditions.

An intriguing feature reported on the patterns obtained on GaSb is the occurrence of long range hexagonal or square order [30]. In the present study, we have only considered the mean values of the amplitude and length scale of the obtained patterns. However, we did not observe a clear onset to ordering which could not be attributed either to tip effects in the AFM observations or to a reminiscence of polishing traces on the substrates. It is possible that this difference it is the consequence of the experimental conditions. In the present study were we have focused on parameter ranges leading to high amplitude patterns. Currently, it is not clear if the enhanced order observed in some studies is a consequence of the nucleation of the sputter shield or late stage coarsening effects like redeposition. A challenge for future work would definitely be to develop *in situ* characterization methods allowing to extract information on both the the amplitude of nanopatterns as well as local or long range order. This would allow to pinpoint in which regime ordering effects can appear on GaSb and to extent the models for ion sputtering induced patterning.

CONCLUSION

Thanks to a recently developed spectroscopic ellipsometry method we were able to investigate the pattern formation on GaSb under ion abrasion. We present the first systematic real-time study of the formation of patterns on GaSb for different experimental conditions like the energy, flux and temperature. This method was also adapted to follow the *in situ* formation of anisotropic tilted cones for oblique ion incidence. At present no other characterization technique has showed similar capabilities.

We evidence the same overall formation laws regardless of the experimental conditions. The amplitude and angle of the patterns may vary considerably, but the patterning process seems to fall into three characteristic regimes: the ion flux determines the timescale, while

the pattern length scale and late stage growth rate are controlled by the energy and the temperature. The lateral length scale of the patterns is mainly determined during the second regime. Important coarsening seems to take place only for high temperatures where the observed patterns are less homogenous. For oblique incidence we reveal the same fundamental behavior as for normal incidence but with a remarkable pace.

The overall behavior of GaSb cannot be rationalized in the Bradley Harper framework generally used to explain patterns formation by ion sputtering. However, a recently suggested formation model based on the ion induced segregation of gallium droplets acting as a more or less efficient sputtering shield can explain a large part of the data. The first regime can be understood as the initial erosion and damage of the surface triggering gallium droplet segregation. The second regime is the growth mode where the gallium caps act as a protection of the surface leading to a direct transfer of the pattern into the material. The third regime corresponds to a wear out of the protecting cap due to decreased supply of gallium leading to a less efficient transfer.

While the growth rate in the second regime can be understood as the yield difference between gallium and GaSb the parameters which control the third regime are less clear. The growth rate appears to be heavily dependent on species characteristics like mobility and fine details are not easy to predict. We plan to address this issue in a detailed analysis and numerical study of the model presented in Ref. [17] in future work. The combined AFM and *in situ* ellipsometry study evidences that it is possible to select a lateral scale using an adequate energy or temperature in the first formation regime. Afterwards, the height can be adjusted by tuning of the flux and the abrasion time. This observation opens for enhanced control over the patterns obtained on GaSb. Additional experimental developments are needed to establish the conditions for the genesis of long range ordering effects. It would be a considerable step towards understanding both limitations and the opportunities for ion beam patterning induced by segregation mechanisms.

APPENDIX

Optical model

The optical properties of GaSb nanopillars with a height less than 100 nm are modeled by treating the structures as an uniaxial graded effective medium, with the optic axis along the pillar axis. The pillars are approximated as a stack of cylinders with linearly decreasing diameter (50 layers). Each cylinder in the stack defines a uniaxal layer with the optic axis along the cylinder axis. In the direction of the optic axis the cylinders will have zero polarizability, and the effective dielectric function $\varepsilon_{||}$ can be found as the volume average of the dielectric functions of GaSb and void [31]:

$$\varepsilon_{||} = f_{GaSb}\varepsilon_{GaSb} + f_v\varepsilon_v. \tag{1}$$

Here f and ε denote the filling factors and complex dielectric functions, respectively. The subscript $GaSb$ refer to the crystalline core, and v to the surrounding void. Normal to the optic axis the effective dielectric function $\varepsilon_\perp$ is given by the equation

$$f_{GaSb}\frac{\varepsilon_{GaSb} - \varepsilon_\perp}{\varepsilon_\perp + \varepsilon_{GaSb}} + f_v\frac{\varepsilon_v - \varepsilon_\perp}{\varepsilon_\perp + \varepsilon_v} = 0. \tag{2}$$

These equations are derived from a generalization of a Bruggeman effective medium equation for anisotropic inclusions, with the depolarization factors L equal to 0.5 orthogonal to the cylinder axis and $L = 0$ parallel to the cylinder axis. The dielectric function GaSb was taken from [32], data from [33] was used for measurements at high temperatures. On average the GaSb pillars have 6 nearest neighbors, hence the filling factors have been calculated for a hexagonal lattice,

$$f_{GaSb}(n) = \frac{\pi}{\sqrt{12}}\, d^2(n), \tag{3}$$

where $d(n)$ is the diameter of the cylinder of layer n, which varies linearly from the bottom diameter D_1 to the top diameter D_2. The bottom and top diameters D_1 and D_2 are normalized to the nearest neighbor distance, since only the volume filling factors influence the effective medium. This means that the lateral size of the pillars can not be found from ellipsometry measurements when the effective medium approximation is valid. The lateral size have therefore been found by *ex situ* AFM or SEM imaging of the final structures only.

Pillars formed by sputtering with oblique ion incidence will point toward the incoming ions. The optic axis will then be inclined by an angle θ from the substrate normal equal

to the angle of ion incidence. This is included in the model by doing an Euler rotation of the principal effective dielectric tensor by an angle θ from the substrate normal. With the experimental set-up used in this work, *in situ* observations can only be performed at normal ion incidence, or at an ion incidence inclined by 22.5° from the substrate normal. In both cases the optic axis of the pillars will be in the ellipsometers plane of incidence, so that there will be no coupling between orthogonal polarization states ($r_{sp} = r_{ps} = 0$).

The reflection coefficients for a stack of anisotropic layers can be calculated by using Berreman's 4×4 differential matrices [34, 35]. The effective parameters can then be found from the ellipsometry measurement by minimizing a figure of merit function χ^2, given as

$$\chi^2 = \frac{1}{N \cdot J - P + 1} \sum_{i=1}^{N} \sum_{j=1}^{J} \left(\frac{m_j^{mod}(i) - m_j^{exp}(i)}{\sigma_j(i)} \right)^2 , \tag{4}$$

where N is the number of points in the spectrum, J is the number of Mueller elements used in the fit, P is the number of free parameters in the model, m_j^{mod} and m_j^{exp} are the simulated and measured Mueller elements normalized with the total reflectivity (M_{11}), and σ_j is the standard deviation of the measurement. Since the nanopillars are uniaxial with the optic axis in the plane of incidence, all the Mueller elements are not necessary. The model could be fitted to $m_{33} = \sin 2\Psi \cos \Delta$ and $m_{43} = -\sin 2\Psi \sin \Delta$ only. This means that standard spectroscopic ellipsometry would have been sufficient. However, since we measure the full Mueller matrix we can observe that the nanostructures give no polarization coupling or depolarization, which can not be described by the uniaxial effective medium model with the optic axis in the plane of incidence.

The effective medium approximation is only valid for structures that are sufficiently small compared to the wavelength of light. As the pillars reach a height of about 100 nm, the applied effective medium model starts to fail. The χ^2 error function then rapidly increase with height, and the the fitted parameters can no longer be trusted. The same applies for the lateral size, which for samples sputtered at 500 eV can cause trouble even for pillars lower than 100 nm, as the lateral size can be larger than the height. Another challenge with measuring larger pillars is that the index gradient leads to a very low reflectivity, demanding longer acquisition times. For sputtering at high energy and flux, the pillar formation can be so fast that the sample changes significantly during one measurement.

Uncertainty in model parameters

Correlated uncertainties calculated from the Hessian matrix[36, 37], defined by the second order partial derivative of χ^2 with respect to the parameters, reveal some coupling between parameters. The coupled uncertainties for a measurement error giving a $\chi^2 = 1$ (uncertainty in Mueller elements of about 0.005) are about 10% in the pillar height. The noise in the *in situ* measuremtets is however quite small. Repeated measurements of the same sample after the end of sputtering results in heigth variations at the order of 1% only. The relativly large uncertainties calculated from the Hessian matrix, or one could also say the too large values of χ^2 compared to the noise, is likly caused by systematic errors,such as instrumnt calibration, angle of incidence, window strain, model insufficiencies (error in reference dielectric functions, effective medium approximation), and so on. These kind of errors are similar for all the measurements. The effect of systematic errors have been explored by fitting the parameters to the measurements with a slightly different angle of incidence, or with a uniform shift of Δ (window strain), in both cases resulting in a uniform shift of the height, and increase of χ^2. In many cases a small change of the angle of incidence or a small shift of Δ might decrease χ^2 a bit, however, such changes have not been considered as more paramaters would introduce more parameter correlation and higher uncertainty. To control that the systematic uncertainties do not get out of hand, the results from the model fits to the ellipsomtric measurements have been closely compared with results from different characterization tools such as AFM and SEM, *ex-situ* of the final structrures.

---

* To whom correspondence should be addressed: `elin.sondergard@saint-gobain.com`

[1] M. Navez, D. Chaperot, and C. Sella, Comptes Rendus Academie des Sciences de Paris **254**, 240 (1962).

[2] R. Bradley and J. Harper, Journal of Vacuum Science and Technology A **6**, 2390 (1988).

[3] T. Mayer, E. Chason, and A. Howard, Journal of Applied Physics **76**, 1633 (1994).

[4] J. Erlebacher, M. J. Aziz, E. Chason, M. B. Sinclair, and J. A. Floro, Physical Review Letters **82**, 2330 (1999).

[5] G. Carter, V. Vishnyakov, and M. J. Nobes, Nuclear Instruments and Methods in Physics Research B **115**, 440 (1996).

[6] R. Gago, L. Vazquez, R. Cuerno, M. Varela, C. Ballesteros, and J. Albella, Applied Physical Letters **78**, 3316 (2001).

[7] T. K. Chini, M. K. Sanyal, and S. R. Bhattacharyya, Physical Review B **66**, 153404 (2002).

[8] E. Chason, T. M. Mayer, B. K. Kellerman, D. T. McIlroy, and A. J. Howard, Physical Review Letters **72**, 3040 (1994).

[9] B. Ziberi, F. Frost, and B. Rauschenbach, Applied Physical Letters **88**, 173115 (2006).

[10] M. A. Makeev, R. Cuerno, and A. Barabasi, Nuclear Instruments and Methods in Physics Research B **197**, 185 (2002).

[11] W. L. Chan and E. Chason, Journal of Applied Physics **101**, 121301 (2007).

[12] S. Facsko, T. Dekorsy, C. Koerdt, C. Trappe, H. Kurz, A. Vogt, and H. L. Hartnagel, Science **285**, 1551 (1999).

[13] Y. Yuba, S. Hazama, and K. Gamo, Nuclear Instruments and Methods in Physics Research B **206**, 648 (2003).

[14] S. Facsko, T. Bobek, A. Stahl, H. Kurz, and T. Dekorsy, Physical Review B **69**, 153412 (2004).

[15] M. Castro, R. Cuerno, L. Vázquez, and R. Gago, Physical Review Letters **94**, 016102 (2005).

[16] S. Le Roy, E. Barthel, N. Brun, A. Lelarge, and E. Søndergård, Journal of Applied Physics **106**, 094308 (2009).

[17] S. Le Roy, E. Søndergård, I.S. Nerbø, M. Kildemo, and M. Plapp, Physical Review B **81**, 161401 (2010).

[18] B. Ziberi, F. Frost, M. Tartz, H. Neumann, and B. Rauschenbach, Thin Solid Films **459**, 106 (2004).

[19] T. Bobek, S. Facsko, H. Kurz, T. Dekorsy, M. Xu, and C. Teichert, Physical Review B **68**, 085324 (2003).

[20] D. Paramanik and S. Varma, Nuclear Instruments and Methods in Physics Research B **266**, 1257 (2008).

[21] O. Plantevin, R. Gago, L. Vazquez, A. Biermanns, and T. H. Metzger, Applied Physics Letters **91**, 113105 (2007).

[22] I. S. Nerbø, S. Le Roy, M. Kildemo, and E. Søndergård, Applied Physics Letters **94**, 213105 (2009).

[23] I. S. Nerbø, M. Kildemo, S. Le Roy, I. Simonsen, E. Søndergård, L. Holt, and J. C. Walmsley, Applied Optics **47**, 5130 (1973).

[24] I. S. Nerbø, S. Le Roy, M. Foldyna, M. Kildemo, and E. Søndergård, Journal of Applied Physics **108**, 014307 (2010).

[25] P. Sigmund, Journal of Materials Science **8**, 1545 (1973).

[26] A. Keller, A. Biermanns, G. Carbone, J. Grenzer, S. Facsko, O. Plantevin, R. Gago, and T. H. Metzger, Applied Physics Letters **94**, 193103 (2009).

[27] S. Facsko, T. Bobek, H. Kurz, T. Dekorsy, S. Kyrsta, and R. Cremer, Applied Physics Letters **80**, 130 (2002).

[28] J. F. Ziegler, J. P. Biersack, and U. Littmark, *The Stopping and Range of Ions in Solids* (Pergamon Press, New York, 1985), new edition in 2009 ed.

[29] M. Xu and C. Teichert, Journal of Applied Physics **96**, 2244 (2004).

[30] F. Frost and B. Rauschenbach, Applied Physics A **77**, 1 (2003).

[31] D. E. Aspnes, *American Journal of Physics* **50** (1982) no. 8, 704–709.

[32] D. E. Aspnes and A. A. Studna, Physical Review B **27**, 985 (1983).

[33] S. Zollner, M. Garriga, J. Humlicieck, S. Goplan, and M. Cardona, Physical Review B **43**, 4349 (1991).

[34] D. W. Berreman, Journal of the Optical Society of America **62**, 502 (1972).

[35] M. Schubert, Physical Review B **53**, 4265 (1996).

[36] G.E. Jellison, Thin Solid Films **234**, 416 (1993).

[37] W. H. Press, S. A. Teukolsky, W. T. Vetterling, and B. P. Flannery, *Numerical Recipes: The Art of Scientific Computing*. Cambridge University Press, 2007.

Real-time *in situ* Mueller matrix ellipsometry of GaSb nanopillars: Observation of anisotropic local alignment

Paper V

Real-time *in situ* Mueller matrix ellipsometry of GaSb nanopillars: observation of anisotropic local alignment

Ingar Stian Nerbø,[1,*] Sebastien Le Roy,[2] Martin Foldyna,[3] Elin Søndergård,[2] and Morten Kildemo[1]

[1]*Physics Department, Norwegian University of Science and Technology (NTNU) NO-7491 Norway*
[2]*UMR 125 Unit mixte CNRS/Saint-Gobain Laboratoire Surface du Verre et Interfaces 39 Quai Lucien Lefranc, F-93303 Aubervilliers, Cedex, France*
[3]*LPICM, Ecole polytechnique, CNRS, 91128 Palaiseau, France*

*ingar.nerbo@ntnu.no

Abstract: The formation of GaSb nanopillars by low energy ion sputtering is studied in real-time by spectroscopic Mueller matrix ellipsometry, from the initial formation in the smooth substrate until nanopillars with a height of $200-300$ nm are formed. As the nanopillar height increased above 100 nm, coupling between orthogonal polarization modes was observed. *Ex situ* angle resolved Mueller polarimetry measurements revealed a 180° azimuth rotation symmetry in the off-diagonal Mueller elements, which can be explained by a biaxial material with different dielectric functions ε_x and ε_y in a plane parallel to the substrate. This polarization coupling can be caused by a tendency for local direction dependent alignment of the pillars, and such a tendency is confirmed by scanning electron microscopy. Such observations have not been made for GaSb nanopillars shorter than 100 nm, which have optical properties that can be modeled as a uniaxial effective medium.

OCIS codes: (160.4236) Nanomaterials; (240.2130) Ellipsometry and polarimetry; (310.6628) Subwavelength structures, nanostructures.

References and links

1. I. S. Nerbø, S. Le Roy, M. Kildemo, and E. Søndergård, "Real-time in situ spectroscopic ellipsometry of gasb nanostructures during sputtering," Appl. Phys. Lett. **94**, 213105 (2009).
2. S. Le Roy, E. Søndergård, I. S. Nerbø, M. Kildemo, and M. Plapp, "Diffuse-interface model for nanopatterning induced by self-sustained ion-etch masking," Phys. Rev. B **81**, 161401 (2010).
3. S. Le Roy, E. Søndergård, I. S. Nerbø, and M. Kildemo, "In-situ and real time study of the formation of nanopatterns on gasb by ion abrasion," Phys. Rev. B (2011), in submission.
4. H. G. Tompkins and E. A. Irene, *Handbook of Ellipsometry* (William Andrew Publishing and Springer-Verlag GmbH and Co., 2005).
5. N. J. Podraza, C. Chen, I. An, G. M. Ferreira, P. I. Rovira, R. Messier, and R. W. Collins, "Analysis of the optical properties and structure of sculptured thin films from spectroscopic mueller matrix ellipsometry," Thin Solid Films **455-456**, 571–575 (2004).
6. G. Beydaghyan, C. Buzea, Y. Cui, C. Elliott, and K. Robbie, "Ex situ ellipsometric investigation of nanocolumns inclination angle of obliquely evaporated silicon thin films," Appl. Phys. Lett. **87**, 153103 (2005).

#145499 - $15.00 USD Received 6 Apr 2011; revised 1 Jun 2011; accepted 3 Jun 2011; published 14 Jun 2011

7. B. Gallas, N. Guth, J. Rivory, H. Arwin, R. Magnusson, G. Guida, J. Yang, and K. Robbie, "Nanostructured chiral silver thin films: a route to metamaterials at optical frequencies," Thin Solid Films, (2010), in production.
8. D. Schmidt, B. Booso, T. Hofmann, E. Schubert, A. Sarangan, and M. Schubert, "Generalized ellipsometry for monoclinic absorbing materials: determination of optical constants of Cr columnar thin films," Opt. Lett. **34**, 992 (2009).
9. I. S. Nerbø, S. Le Roy, M. Foldyna, M. Kildemo, and E. Søndergård, "Characterization of inclined GaSb nanopillars by Mueller matrix ellipsometry," J. Appl. Phys. **108**, 014307 (2010).
10. M. Ranjan, T. W. H. Oates, S. Facsko, and W. Möller, "Optical properties of silver nanowire arrays with 35 nm periodicity," Opt. Lett. **35**, 2576–2578 (2010).
11. D. Aspnes, J. Harbison, A. Studna, and L. Florez, "Reflectance-difference spectroscopy system for real-time measurements of crystal growth," Appl. Phys. Lett. **52**, 957–959 (1988).
12. J. Bremer and O. Hunderi, "Ras studies of laterally nanostructured surfaces," Phys. Stat. Solidi A **184**, 89–100 (2001).
13. W. Richter, "In-situ observation of movpe epitaxial growth," Appl. Phys. A **75**, 129–140 (2002).
14. F. Everts, H. Wormeester, and B. Poelsema, "Optical anisotropy induced by ion bombardment of Ag(001)," Phys. Rev. B **78**, 155419 (2008).
15. C. Chen, M. Horn, S. Pursel, C. Ross, and R. Collins, "The ultimate in real-time ellipsometry: multichannel mueller matrix spectroscopy," Appl. Surface Sci. **253**, 38–46 (2006).
16. E. Collett, *Polarized Light: Fundamentals and Applications* (Marcel Dekker, Inc., 2003).
17. P. Hauge, "Conventions and formulas for using the Mueller-Stokes calculus in ellipsometry," Surface Sci. **96**, 81–107 (1980).
18. D. W. Berreman, "Optics in stratified and anisotropic media: 4x4-matrix formulation," J. Opt. Soc. Am. **62**, 502–510 (1972).
19. M. Schubert, "Polarization-dependent optical parameters of arbitrarily anisotropic homogeneous layered systems," Phys. Rev. B **53**, 4265–4274 (1996).
20. A. De Martino, S. Ben Hatit, and M. Foldyna, "Mueller polarimetry in the back focal plane," in "Society of Photo-Optical Instrumentation Engineers (SPIE) Conference Series," (2007), vol. 6518.
21. B. H. Ibrahim, S. B. Hatit, and A. De Martino, "Angle resolved mueller polarimetry with a high numerical aperture and characterization of transparent biaxial samples," Appl. Opt. **48**, 5025–5034 (2009).
22. S. B. Hatit, M. Foldyna, A. De Martino, and B. Drévillon, "Angle-resolved mueller polarimeter using a microscope objective," Phys. Stat. Solidi A **205**, 743–747 (2008).
23. I. S. Nerbø , M. Kildemo, S. Le Roy, I. Simonsen, E. Søndergård, L. Holt, and J. Walmsley, "Characterisation of nanostructured GaSb : comparison between large-area optical and local direct microscopic techniques," Appl. Opt. **47**, 5130–5139 (2008).
24. T. Yamaguchi, S. Yoshida, and A. Kinbara, "Optical effect of the substrate on the anomalous absorption of aggregated silver films," Thin Solid Films **21**, 173–187 (1974).
25. E. Fort, C. Ricolleau, and J. Sau-Pueyo, "Dichroic thin films of silver nanoparticle chain arrays on facetted alumina templates," Nano Lett. **3**, 65–67 (2003).
26. S. Camelio, D. Babonneau, D. Lantiat, L. Simonot, and F. Pailloux, "Anisotropic optical properties of silver nanoparticle arrays on rippled dielectric surfaces produced by low-energy ion erosion," Phys. Rev. B **80**, 1–10 (2009).
27. C. Granqvist and O. Hunderi, "Optical properties of ultrafine gold particles," Phys. Rev. B **16**, 3513–3534 (1977).
28. S. Le Roy, E. Barthel, N. Brun, A. Lelarge, and E. Søndergård, "Self-sustained etch masking: a new concept to initiate the formation of nanopatterns during ion erosion," J. Appl. Phys. **106**, 094308 (2009).
29. J. E. Spanier and I. P. Herman, "Use of hybrid phenomenological and statistical effective-medium theories of dielectric functions to model the infrared reflectance of porous sic films," Phys. Rev. B **61**, 10437–10450 (2000).

1. Introduction

Spectroscopic ellipsometry (SE) has proved to be an efficient tool for real-time observation of the formation of nanostructured surfaces, *e.g.* the height evolution of GaSb nanopillars has been monitored during ion sputtering [1]. Real-time *in situ* measurements allow to follow the formation in time, and to find how the formation rate depends on experimental parameters, leading to a deeper understanding of the formation mechanisms of such structures [2, 3]. Such studies are not feasible with traditional *ex situ* microscopic characterization methods for nanoscale structures, such as atomic force microscopy (AFM) or scanning electron microscopy (SEM), due to time-demand and uncertainty of process parameters.

Ellipsometry is based on measuring the relative change of phase and amplitude between two orthogonal field components of reflected light. For reflections from an anisotropic material,

#145499 - $15.00 USD Received 6 Apr 2011; revised 1 Jun 2011; accepted 3 Jun 2011; published 14 Jun 2011

there will in general be coupling between orthogonal field components. To fully characterize this coupling it is necessary to do generalized ellipsometry or Mueller matrix ellipsometry [4]. GaSb nanopillars prepared by sputtering with normal ion incidence, with a height less than 100 nm, have earlier been reported not to result in coupling between orthogonal polarization components, and to be modelled as a uniaxial effective material with the optic axis normal to the substrate [1]. How polarized light is affected by a reflection from such a surface can be completely characterized by standard ellipsometry. However, for larger nanopillars, the effective medium approximation is expected to fail as the size of the structure becomes comparable to the wavelength of light, and the uniaxial model will no longer be able to represent the optical properties of the pillars. In this study we report real-time *in situ* spectroscopic Mueller matrix measurements of GaSb during ion sputtering: from the initial formation in the smooth substrate, until pillars with heights of $200-300$ nm are formed. The Mueller matrix will contain information about possible anisotropic properties of the structure, caused by an anisotropic shape or organization of the pillars.

The anisotropic optical properties of a number of different nanostructures have previously been studied *ex situ* by generalized ellipsometry or Mueller matrix ellipsometry [5–10]. Reflectance-difference(anisotropy) spectroscopy (RDS/RAS) have been widely applied for real-time studies of surface anisotropies of semiconductors [11] and nanostructured surfaces [12–14]. RAS is highly sensitive, but can only measure the anisotropic part of the optical properties. In comparison Mueller matrix ellipsometry can measure the absolute dielectric function of an anisotropic material, not only the relative difference. Real-time Mueller matrix spectroscopy was demonstrated for the first time by Chen *et al.* [15], for characterization of geometrical optics scale roughness on ZnO. The reported roughness had isotropic optical properties, but its depolarizing properties made Mueller matrix measurements necessary. To our knowledge, generalized ellipsometry or Mueller matrix ellipsometry studies of an anisotropic nanostructured surface have not been performed in real-time before.

2. Theory and optical modeling

A Mueller matrix ellipsometer measures the 4×4 real valued Mueller matrix, which can describe any linear interaction of polarized light with a sample by transforming Stokes vectors representing the polarization state of light [16]. For non-depolarizing samples, the Mueller matrix can be used to overdetermine the normalized Jones matrix, containing the complex reflection coefficients [15]. The reflection coefficients (r_{ij}, with the subscripts i and j denoting the p and s directions) can be defined as

$$\begin{bmatrix} E_p \\ E_s \end{bmatrix}^{out} = \begin{bmatrix} r_{pp} & r_{ps} \\ r_{sp} & r_{ss} \end{bmatrix} \begin{bmatrix} E_p \\ E_s \end{bmatrix}^{inc},$$

with E_p and E_s denoting the complex field components parallel and orthogonal to the plane of incidence, respectively. The connection between the Jones and Mueller matrices for a non-depolarizing sample can be found in *e.g.* Ref. [17]. The Mueller matrix of a depolarizing sample has no equivalent Jones matrix. The reflection coefficients for a stack of homogeneous layers of optically anisotropic material can be calculated using Berreman's 4×4 differential matrix method [18, 19].

3. Experimental

A GaSb wafer (100) was sputtered for 10 minutes with 500 eV Ar^+ ions at normal incidence, with an ion flux of 0.32 mA/cm^2. *In situ* spectroscopic Mueller matrix measurements was performed every 5 seconds during sputtering, in the photon energy range of $1.5-2.8$ eV (MM16,

#145499 - $15.00 USD Received 6 Apr 2011; revised 1 Jun 2011; accepted 3 Jun 2011; published 14 Jun 2011

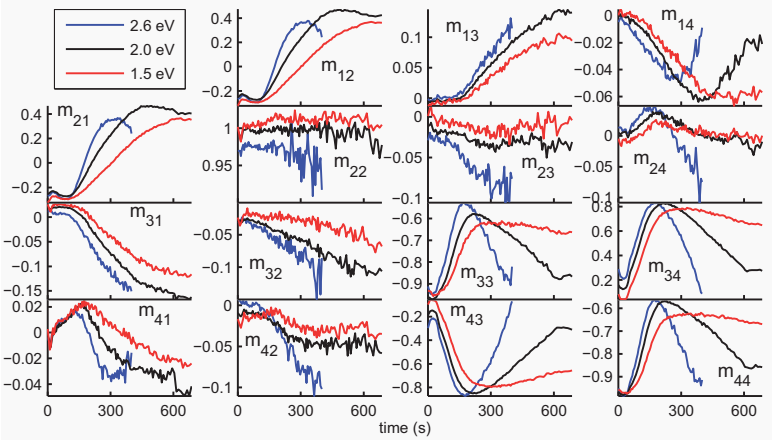

Fig. 1. Real-time Mueller matrix measurement of GaSb nanopillars, presented at three different photon energies. The 2.6 eV photon energy measurement is not presented for a sputtering time higher than 400 s, as after this time the surface becomes highly anti-reflective, and the optical signal becomes too low at high energies.

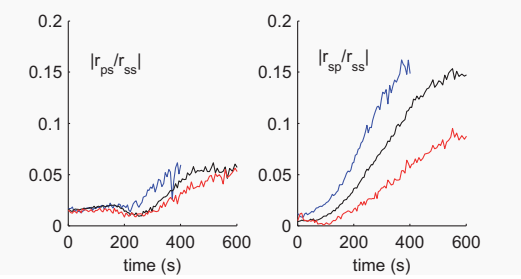

Fig. 2. Absolute values of the off-diagonal Jones elements, normalized by r_{ss}, derived from real-time Mueller matrix measurements of the formation of GaSb nanopillars, at photon energies of 2.6 eV (blue), 2.0 eV (black) and 1.5 eV (red).

Horiba Jobin Yvon), at an angle of incidence of 45°. The final nanostructured surface was studied *ex situ* by SEM. A sample prepared with identical sputtering conditions was also studied *ex situ* with a single wavelength (633 nm) angle resolved Mueller matrix polarimeter. The instrument applied a high numerical aperture (NA=0.95) microscope objective in a double pass configuration with its back focal plane imaged on a charge coupled device camera, allowing simultaneous measurements of reflected light at all azimuth angles and all angles of incidence below 62° [20–22].

4. Results and discussion

Figure 1 shows real-time *in situ* measurements of the Mueller matrix of the GaSb sample during sputtering, for three different photon energies. During the first 2 – 3 minutes there is no

#145499 - $15.00 USD Received 6 Apr 2011; revised 1 Jun 2011; accepted 3 Jun 2011; published 14 Jun 2011

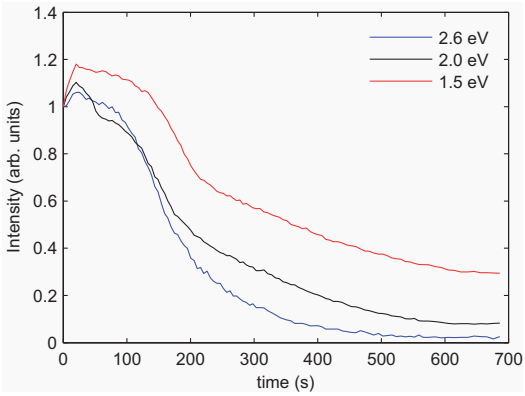

Fig. 3. Reflected intensity change from GaSb during sputtering, normalized by the reflected intensity before sputtering. The values are equal to the change in intensity refletance for unpolarized light (Mueller element M_{11}).

significant polarization coupling in the Mueller matrix, as all the four elements in the upper-right and lower-left corners are close to zero. After about 3 minutes of sputtering, polarization coupling becomes visible in the Mueller matrix and increases steadily until the end of the sputtering. To illustrate this more clearly, the absolute value of the normalized off-diagonal Jones elements, $|r_{ps}/r_{ss}|$ and $|r_{sp}/r_{ss}|$, have been derived from the Mueller matrix and are presented in Fig. 2. This polarization coupling indicate that the effective dielectric function is anisotropic in the plane parallel to the substrate, which is not consistent with a uniaxial material with the optic axis normal to the substrate. The reflected intensity change from the GaSb surface during sputtering is presented in Fig. 3. The nanopillars have a conical shape, which gives a gradient in the effective index of refraction [23], making the pillars anti-reflective. This means that the reflected light intensity decrease as the height of the pillars increase. After 400 s the curves for the 2.6 eV measurement have been cut in Figs. 1 and 2, as the noise level is too high.

The lateral anisotropy of the nanopillars could have several different causes. It was earlier reported that inclined GaSb pillars prepared by sputtering at oblique ion incidence has highly anisotropic optical properties [9], and such structures can be modeled as an effective uniaxial material with the optic axis parallel to the inclined pillar axis, resulting in polarization coupling in the Mueller matrix. A slight tilt (less than $1-2^{\circ}$) of the incident ion beam from the sample normal during the *in situ* measurements could cause the observed coupling. Another explanation could be that the pillars have an average laterally anisotropic shape, *e.g.* the pillars could have an elliptical instead of circular crossection. On the other hand, the pillars could individually have a uniaxial shape, but have an average anisotropic organization, *e.g.* a direction dependent nearest neighbor distance. Such a lateral anisotropy should result in the pillars having optical properties like a biaxial material.

To get a better understanding of the anisotropic optical properties of the sample, the final structure was studied by *ex situ* angle resolved Mueller matrix polarimetry. Fig. 4 presents a polar plot of the normalized Mueller elements m_{13} and m_{14}, where the radial coordinate represents the sine of the angle of incidence and the polar angle represents the azimuth sample orientation. These figures reveal important information about the symmetries of the structure. One can observe four lines in the polar plots where the Mueller elements are zero, correspond-

#145499 - $15.00 USD Received 6 Apr 2011; revised 1 Jun 2011; accepted 3 Jun 2011; published 14 Jun 2011

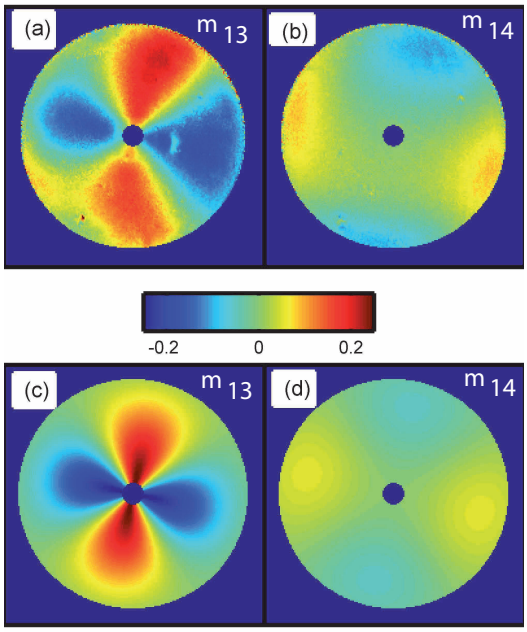

Fig. 4. Angle resolved Mueller matrix elements m_{13} (a) and m_{14} (b), and simulations of m_{13} (c) and m_{14} (d) for reflection from a biaxial effective medium. All at a wavelength of 633 nm. ($m_{13} = Re[r_{pp}r^*_{ps} + r_{sp}r^*_{ss}]/M_{11}$ and $m_{14} = Im[r_{pp}r^*_{ps} + r_{sp}r^*_{ss}]/M_{11}$).

ing to azimuth sample orientations separated by rotations of 90°, where there is no polarization coupling for all angles of incidence. The elements are also approximately symmetric for a rotation of 180°. These symmetries can be explained by the nanopillars behaving as a biaxially anisotropic material, with one of the intrinsic axes (referred to as the c-axis) normal to the substrate. The azimuth orientations resulting in no polarization coupling then correspond to the cases when one of the two other intrinsic axes lie in the plane of incidence. This symmetry implies that the polarization coupling observed in the real-time Mueller matrix measurements are mainly caused by a laterally anisotropic shape or organization. A small pillar inclination caused by slightly oblique ion incidence, would instead give only two azimuth orientations with no polarization coupling (with the pillars inclined in the plane of incidence), and a change of sign of element m_{13} and m_{14} for an azimuth rotation of 180°. A small tilt however, could still cause the slight difference between the left and right lobe of Fig. 4(a).

To study the shape and size of the final structure, SEM images of the samples were taken *ex situ* after sputtering. A crossection image of the surface is presented in Fig. 5(b), where pillars with a height of $250-300$ nm can be seen. Figure 5(c) shows an overview of the surface, where apparently randomly distributed pillars can be seen. The power spectral density (PSD) of the

#145499 - $15.00 USD Received 6 Apr 2011; revised 1 Jun 2011; accepted 3 Jun 2011; published 14 Jun 2011

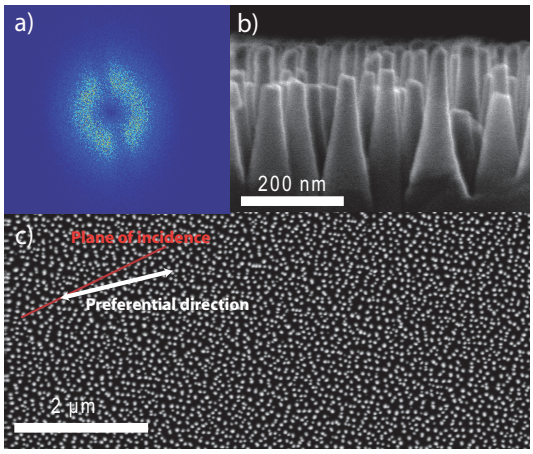

Fig. 5. (a) Power spectral density of the normal view SEM image (magnified), (b) GaSb pillars made by normal incidence sputtering, crosssection SEM image, and (c) normal view SEM image. The direction corresponding to the line in the power spectral density is denoted by the white arrow, together with the plane of incidence of the *in situ* Mueller matrix measurements.

SEM image (Fig. 5(a)) shows signs of an anisotropic organization, breaking the symmetry in the lateral plane. Randomly distributed circular structures corresponds to a donut shape in the PSD. The observed oppositely placed holes in the donut indicate a longer nearest neighbor distance in this direction (the opposite of alignment). From the SEM image one can see some tendency of local alignment of neighboring pillars along apparently random directions (lines of $4-10$ pillars are observed). The PSD indicate that local alignment is less likely in the direction corresponding to the holes in the donut shape. This direction is marked in the normal view SEM image in Fig. 5(c), and was found to be rotated by an angle of 13° from the plane of incidence of the *in situ* ellipsometry measurements.

In the first 3 minutes of sputtering, the measured Mueller matrix is approximately block-diagonal, and the height evolution of the pillars can be found by fitting the previously reported graded uniaxial effective medium model [1] to the non-zero Muller elements. In this model the pillars are treated as a stack of cylinders with decreasing diameter. Each cylinder define a layer, with an effective dielectric function found by a generalized anisotropic Bruggeman effective medium equation (see the Appendix). The heights of the GaSb nanopillars derived from this model are presented in Fig. 6, together with the χ^2 error function (calculated for an assumed experimental uncertainty of $\sigma = 0.01$ in the measured Mueller elements). After a short initial period of 30 s, the pillars start to form with a steady height increase of about 1nm a second. After 3 minutes of sputtering, the pillars have reached a height of about 120 nm, and the error function χ^2 starts to increase rapidly. This is about the same time as the polarization coupling becomes visible in the measured Mueller matrix, and the uniaxial effective medium model can no longer be applied. In addition, the reduced reflectivity of the pillars leads to a higher noise level at high energies, which also contributes to the increase in χ^2.

The observed lateral anisotropy (polarization coupling) was ascribed to the effective optical properties of the nanopillars being biaxially anisotropic, with one of the intrinsic axes normal

#145499 - $15.00 USD Received 6 Apr 2011; revised 1 Jun 2011; accepted 3 Jun 2011; published 14 Jun 2011

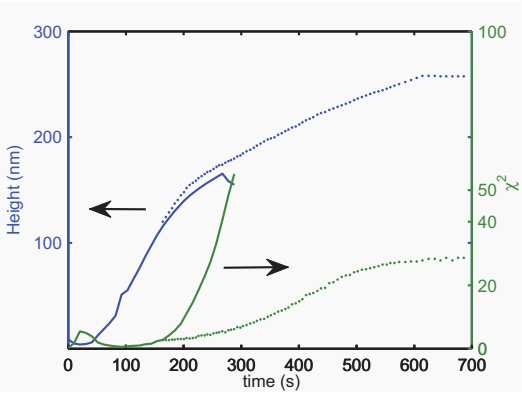

Fig. 6. Thickness of an graded anisotropic effective medium layer fitted to *in situ* Mueller matrix measurements of GaSb during sputtering, together with the error function χ^2. In the beginning a uniaxial model was applied (solid line), after 3 minutes a biaxial model (dots) was found to better represent the pillars.

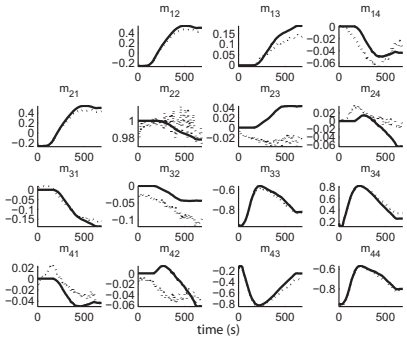

Fig. 7. Fitted Mueller matrix (solid) and experimental measurements (dots) at 2.0 eV.

#145499 - $15.00 USD Received 6 Apr 2011; revised 1 Jun 2011; accepted 3 Jun 2011; published 14 Jun 2011

to the substrate. From SEM images this was concluded to be caused an average anisotropic organization. This can not be treated by the anisotropic Bruggeman equation (Eq. (1) in the Appendix), which is independent of the spatial organization. Extended effective medium models including neighbor interactions have been discussed in the literature by *e.g.* Yamaguchi *et. al* [24], and an extended Maxwell-Garnett equation has been applied to include anisotropic neighbor interactions in metallic nanostrucures [25, 26]. Such a model needs detailed information about the local ordering of the structures, taken from *e.g.* SEM-images. This information is not available for the *in situ* measurements of the formation of the GaSb nanopillars. A possible anisotropic ordering is instead crudely approximated by letting the depolarization factors L_a and L_b represent an "effective" shape, *i.e.* an anisotropic ordering is modeled by letting the pillars have an effective elliptical crossection. The use of effective depolarization factors to model neighbor interactions was introduced by Granqvist and Hunderi [27]. Figure 4(c) and 4(d) shows simulations of angle resolved Mueller elements m_{13} and m_{14} for such a biaxial model, which fits qualitatively well with the experimental measurements. The effective depolarization factors $L_a = 0.47$, $L_b = 0.53$ and $L_c = 0$ were used along the three principal axes, with the c-axis pointing normal to the substrate. A pillar height of 290 nm and top and bottom relative diameter of $D_2 = 0.1$ and $D_1 = 1$ (filling factor calculated for dense hexagonal ordering) was used in the simulation (see Appendix).

Fits of a biaxial model to the real-time measurements of the pillar formation after 3 minutes of sputtering are presented in Fig. 7, with the resulting pillar height and χ^2 values shown in Fig. 6. From the the measurement of the final structure, an effective depolarization factor of $L_a = 0.54$ was found for one of the principal axes in the lateral plane, rotated by an angle of 12° from the plane of incidence. The other principal axis in the lateral plane was set to have $L_b = 1 - L_a$, and the the depolarization factor for the last axis along the surface normal was set to $L_c = 0$. The orientation of the *a*-axis corresponds well with the direction corresponding to the holes in the donut shaped PSD in Fig. 5(a). As one would expect, the effective depolarization factor is highest along the direction with less local alignment. For the remaining real-time measurements, the orientation of the principal axes of the effective medium was fixed to be the same as the one found for the final measurement. This is reasonable as the angle was confirmed by SEM, and as the azimuth rotation of the principal axes are expected to be coupled to the depolarization factors for fits at ellipsometry measurements at a single azimuth sample orientation. The fit was limited to the photon energy range of $1.5 - 2.0$ eV due to the increased noise level caused by the reduced reflectivity from high pillars. In Fig. 6, a great improvement of χ^2 is observed for the biaxial model compared to the uniaxial model. Still, an increase in χ^2 with time is observed also for the more complex biaxial model, which is as expected since effective medium should not be valid for structures with a size comparable to the wavelength of light. The pillar height need not be the critical parameter for failure of the effective medium model, as interference effects normal to the substrate are included in the transfer matrix calculations for the reflection coefficients. More important is the lateral size, which must be sufficiently small for the model to be valid. The evolution of this size can however not be observed from the Mueller matrix measurements. Earlier reports from *ex situ* AFM studies on GaSb sputtered with different ion energies found that the lateral size of the pillars increase with energy [3]. For pillars sputtered with an ion energy of 300 and 400 eV, the lateral size was found to saturate to a constant value early in the formation. For samples sputtered with an ion energy of 500 eV, the lateral size of the pillars was found to increase for the first 5 minutes of sputtering. This means that the lateral size is increasing in the range where the χ^2 value is increasing. The fitted height seems, however, to give a reasonable approximation to the pillar height, with a final value of 250 nm which correspond well to the pillar height of 250-300 nm as observed in the SEM image. The resulting height evolution during sputtering is also equal to the observation

#145499 - $15.00 USD Received 6 Apr 2011; revised 1 Jun 2011; accepted 3 Jun 2011; published 14 Jun 2011

of sputtering at lower energy [1], with a transition to a slower formation rate, but no saturation. This indicates that the formation mechanism reported in Ref. [2] is also valid for the formation of large pillars formed by sputtering at the higher ion energy of 500 eV.

The origin of the anisotropic ordering in the lateral dimension is not fully understood. As the formation does not depend on the crystal orientation of the substrate [28], there should not be any preferential direction for sputtering at normal ion incident. However, this symmetry could be broken by a small deviation of the ion incidence from the surface normal. Another explanation could be an initial anisotropic substrate roughness from the wafer polishing.

5. Conclusion

The formation of GaSb nanopillars by sputtering with 500 eV Ar^+ ions has been monitored in real-time by Mueller matrix ellipsometry. For the first 3 minutes the optical properties of the nanopillars were modeled by a graded uniaxial effective medium model. After 3 minutes, as the pillar height surpassed 100 nm, coupling between orthogonal polarization modes was observed from the measurements. From *ex situ* angle resolved Mueller matrix polarimetry of the final structure, this coupling was attributed to the pillars having effective biaxial optical properties, with one intrinsic axis normal to the substrate. Fourier analysis of a scanning electron microscope image of the final nanopillars, shows that the lateral anisotropy can be attributed to a direction dependent nearest neighbor distance. Each individual pillar has a uniaxial symmetry, the biaxial symmetry comes from the anisotropic organization of the pillars.

6. Appendix

It was earlier reported [1] that GaSb nanopillars with a height less than 100 nm could be modeled as a graded uniaxial effective medium, by treating the pillars as a stack of cylinders with decreasing diameter. Each cylinder in the stack constitute an effective layer with an effective dielectric tensor found by using a generalized Bruggeman effective medium equation for ellipsoidal inclusions [29]

$$f_{GaSb}\frac{\varepsilon_{GaSb}-\varepsilon_{ii}}{\varepsilon_{ii}+L_i(\varepsilon_{GaSb}-\varepsilon_{ii})}+f_v\frac{\varepsilon_v-\varepsilon_{ii}}{\varepsilon_{ii}+L_i(\varepsilon_v-\varepsilon_{ii})}=0, \tag{1}$$

where f and ε denote the filling factors and complex dielectric functions, respectively, with the subscript *GaSb* referring to the crystalline core, and v to the surrounding void. L_i denotes the depolarization factor in direction i (along a principal axis of the structure) and ε_{ii} is the effective dielectric function in direction i. For cylindrical inclusions $L_{||}=0.5$ (parallel to the mean surface) and $L_{\perp}=0$ (perpendicular to the mean surface). This gives a uniaxial anisotropic material with the optic axis normal to the mean surface, resulting in no coupling between orthogonal field components for reflected light ($r_{ps}=r_{sp}=0$). If the cylinder cross-sections are elliptical instead of circular, and all have the same orientation, the depolarization factors will be different along the minor and major axis ($L_x \neq L_y$), giving a biaxial anisotropic material, which in general lead to $r_{ps}\neq 0$ and $r_{sp}\neq 0$. The uniaxial symmetry can also be broken by an anisotropic ordering, *e.g.* by a different pillar separation along different directions. This can not be treated by Eq. (1), which is independent on spatial organization.

On average the GaSb pillars have 6 nearest neighbors [23], hence the filling factors have been calculated for a hexagonal lattice,

$$f_{GaSb}(n)=\frac{\pi}{\sqrt{12}}d^2(n),$$

where $d(n)$ is the diameter of the cylinder of layer n, which varies linearly from the bottom diameter D_1 to the top diameter D_2. The bottom and top diameters D_1 and D_2 are normalized

#145499 - $15.00 USD Received 6 Apr 2011; revised 1 Jun 2011; accepted 3 Jun 2011; published 14 Jun 2011

to the nearest neighbor distance, since only the volume filling factors influence the effective medium. This means that the lateral size of the pillars can not be found from ellipsometry measurements when the effective medium approximation is valid.

#145499 - $15.00 USD Received 6 Apr 2011; revised 1 Jun 2011; accepted 3 Jun 2011; published 14 Jun 2011

Fast and optimal broad-band Stokes/Mueller polarimeter design by the use of a genetic algorithm

Paper VI

Fast and optimal broad-band Stokes/Mueller polarimeter design by the use of a genetic algorithm

Paul Anton Letnes,* Ingar Stian Nerbø, Lars Martin Sandvik Aas, Pål Gunnar Ellingsen, and Morten Kildemo

Department of Physics, The Norwegian University of Science and Technology (NTNU), N-7491 Trondheim, Norway

**paul.anton.letnes@gmail.com*

Abstract: A fast multichannel Stokes/Mueller polarimeter with no mechanically moving parts has been designed to have close to optimal performance from 430 – 2000 nm by applying a genetic algorithm. Stokes (Mueller) polarimeters are characterized by their ability to analyze the full Stokes (Mueller) vector (matrix) of the incident light (sample). This ability is characterized by the condition number, κ, which directly influences the measurement noise in polarimetric measurements. Due to the spectral dependence of the retardance in birefringent materials, it is not trivial to design a polarimeter using dispersive components. We present here both a method to do this optimization using a genetic algorithm, as well as simulation results. Our results include fast, broad-band polarimeter designs for spectrographic use, based on 2 and 3 Ferroelectric Liquid Crystals, whose material properties are taken from measured values. The results promise to reduce the measurement noise significantly over previous designs, up to a factor of 4.5 for a Mueller polarimeter, in addition to extending the spectral range.

OCIS codes: (120.2130) Ellipsometry and polarimetery; (120.4570) Optical design of instruments; (300.0300) Spectroscopy.

References and links

1. A. M. Gandorfer, "Ferroelectric retarders as an alternative to piezoelastic modulators for use in solar Stokes vector polarimetry," Opt. Eng. **38**, 1402–1408 (1999).
2. P. Collins, R. Redfern, and B. Sheehan, "Design, construction and calibration of the Galway astronomical Stokes polarimeter (GASP)," in *AIP Conference Proceedings,* D. Phelan, O. Ryan, and A. Shearer, eds. (AIP, Edinburgh (Scotland), 2008), vol. 984, p. 241.
3. A. Alvarez-Herrero, V. Martínez-Pillet, J. del Toro Iniesta, and V. Domingo, "The IMaX polarimeter for the solar telescope SUNRISE of the NASA long duration balloon program," in *Proceedings of API'09,* E. Garcia-Caurel, ed. (EPJ Web of Conferences, 2010), vol. 5, p. 05002.
4. J. D. Howe, M. A. Miller, R. V. Blumer, T. E. Petty, M. A. Stevens, D. M. Teale, and M. H. Smith, "Polarization sensing for target acquisition and mine detection," in *Polarization Analysis, Measurement, and Remote Sensing III,* D. B. Chenault, M. J. Duggin, W. G. Egan, and D. H. Goldstein, eds., Proc. SPIE **4133**, 202–213 (2000).
5. M. H. Smith, P. D. Burke, A. Lompado, E. A. Tanner, and L. W. Hillman, "Mueller matrix imaging polarimetry in dermatology," in *Biomedical Diagnostic, Guidance, and Surgical-Assist Systems II,* T. Vo-Dinh, W. S. Grundfest, and D. A. Benaron, eds., Proc. SPIE **3911**, 210–216 (2000).
6. R. N. Weinreb, S. Shakiba, and L. Zangwill, "Scanning laser polarimetry to measure the nerve fiber layer of normal and glaucomatous eyes," Am. J. Ophthalmol. **119**, 627–636 (1995).

#134880 - $15.00 USD Received 9 Sep 2010; revised 5 Oct 2010; accepted 5 Oct 2010; published 18 Oct 2010

7. M. Foldyna, A. D. Martino, R. Ossikovski, E. Garcia-Caurel, and C. Licitra, "Characterization of grating structures by Mueller polarimetry in presence of strong depolarization due to finite spot size," Opt. Commun. **282**, 735–741 (2009).
8. I. S. Nerbø, S. Le Roy, M. Foldyna, M. Kildemo, and E. Søndergård, "Characterization of inclined GaSb nanopillars by Mueller matrix ellipsometry," J. Appl. Phys. **108**, 014307 (2010).
9. L. Jin, M. Kasahara, B. Gelloz, and K. Takizawa, "Polarization properties of scattered light from macrorough surfaces," Opt. Lett. **35**, 595–597 (2010).
10. T. A. Germer, "Polarized light scattering by microroughness and small defects in dielectric layers." J. Opt. Soc. Am. A **18**, 1279–1288 (2001).
11. T. Germer, "Measurement of roughness of two interfaces of a dielectric film by scattering ellipsometry," Phys. Rev. Lett. **85**, 349–352 (2000).
12. F. Stabo-Eeg, M. Kildemo, I. Nerbø, and M. Lindgren, "Well-conditioned multiple laser Mueller matrix ellipsometer," Opt. Eng. **47**, 073604 (2008).
13. J. S. Tyo, "Noise equalization in Stokes parameter images obtained by use of variable-retardance polarimeters," Opt. Lett. **25**, 1198–1200 (2000).
14. D. S. Sabatke, M. R. Descour, E. L. Dereniak, W. C. Sweatt, S. A. Kemme, and G. S. Phipps, "Optimization of retardance for a complete Stokes polarimeter," Opt. Lett. **25**, 802–804 (2000).
15. R. M. A. Azzam and A. De, "Optimal beam splitters for the division-of-amplitude photopolarimeter," J. Opt. Soc. Am. A **20**, 955–958 (2003).
16. R. M. A. Azzam, "Photopolarimetric measurement of the Mueller matrix by Fourier analysis of a single detected signal," Opt. Lett. **2**, 148 (1978).
17. J. M. Bueno, "Polarimetry using liquid-crystal variable retarders: theory and calibration," J. Opt. A: Pure Appl. Opt. **2**, 216–222 (2000).
18. E. Garcia-Caurel, A. D. Martino, and B. Drévillon, "Spectroscopic Mueller polarimeter based on liquid crystal devices," Thin Solid Films **455-456**, 120–123 (2004).
19. J. Ladstein, M. Kildemo, G. Svendsen, I. Nerbø, and F. Stabo-Eeg, "Characterisation of liquid crystals for broadband optimal design of Mueller matrix ellipsometers," in *Liquid Crystals and Applications in Optics,* M. Glogarova, P. Palffy-Muhoray, and M. Copic, eds. Proc. SPIE **6587**, 65870D (2007).
20. L. M. S. Aas, P. G. Ellingsen, M. Kildemo, and M. Lindgren, "Dynamic Response of a fast near infra-red Mueller matrix ellipsometer," J. Mod. Opt. **(accepted)** (2010).
21. D. Cattelan, E. Garcia-Caurel, A. De Martino, and B. Drevillon, "Device and method for taking spectroscopic polarimetric measurements in the visible and near-infrared ranges," Patent application 2937732, France (2010).
22. J. H. Holland, "Genetic algorithms," Scientific American **267**, 44–50 (1992).
23. D. Floreano and C. Mattiussi, *Bio-Inspired Artificial Intelligence: Theories, Methods, and Technologies* (The MIT Press, 2008).
24. A. Kudla, "Application of the genetic algorithms in spectroscopic ellipsometry," Thin Solid Films **455-456**, 804–808 (2004).
25. G. Cormier and R. Boudreau, "Genetic algorithm for ellipsometric data inversion of absorbing layers," J. Opt. Soc. Am. A **17**, 129–134 (2000).
26. V. R. Fernandes, C. M. S. Vicente, N. Wada, P. S. André, and R. A. S. Ferreira, "Multi-objective genetic algorithm applied to spectroscopic ellipsometry of organic-inorganic hybrid planar waveguides," Opt. Express **18**, 16580–16586 (2010).
27. F. Stabo-Eeg, M. Kildemo, E. Garcia-Caurel, and M. Lindgren, "Design and characterization of achromatic 132° retarders in CaF_2 and fused silica," J. Mod. Opt. **55**, 2203–2214 (2008).
28. W. H. Press, S. A. Teukolsky, W. T. Vetterling, and B. P. Flannery, *Numerical Recipes: The Art of Scientific Computing* (Cambridge University Press, 2007).
29. E. Compain, S. Poirier, and B. Drevillon, "General and self-consistent method for the calibration of polarization modulators, polarimeters, and Mueller-matrix ellipsometers," Appl. Opt. **38**, 3490–3502 (1999).
30. J. Ladstein, F. Stabo-Eeg, E. Garcia-Caurel, and M. Kildemo, "Fast near-infra-red spectroscopic Mueller matrix ellipsometer based on ferroelectric liquid crystal retarders," Phys. Status Solidi C **5**, 1097–1100 (2008).

1. Introduction

Polarimeters are applied in a wide range of fields, from astronomy [1–3], remote sensing [4] and medical diagnostics [5, 6] to applications in ellipsometry such as characterizing gratings [7], nanostructures [8] and rough surfaces [9–11]. As all polarimeters are based on inverting so-called system matrices, it is well known that the measurement error from independent Gaussian noise is minimized when the condition number (κ) of these system matrices is minimized [12, 13]. It has been shown that $\kappa = \sqrt{3}$ is the best condition number that can be achieved for such a system, and that this optimal condition number can be achieved by several different

#134880 - $15.00 USD Received 9 Sep 2010; revised 5 Oct 2010; accepted 5 Oct 2010; published 18 Oct 2010

approaches using various optical components (*e.g.* rotating retarders [14], division of amplitude [15, 16], and liquid-crystal variable retarders [17]). In many applications it is necessary to perform fast spectroscopic measurements (*e.g.* by using a Charge-Coupled Device (CCD) based spectrograph) [18]. In that case, the wavelength dependence of the optical elements will cause the polarimeter not to be optimally conditioned over the full range simultaneously. A system based on two Ferroelectric Liquid Crystals (FLC) has been reported to be fast and reasonably well conditioned over the visible or near infrared spectral range [18–20]. By introducing a third FLC a similar system has been proposed to have an acceptable condition number from the visible to the near infra-red ($430-1700$ nm) [21]. The design of a system having the best possible condition number over a broad spectrum is a challenging optimization problem due to the large number of parameters; many optimization algorithms are prone to return local optimums, and a direct search is too time consuming. To avoid this time-consuming exhaustive search, we decided to employ the Genetic Algorithm (GA). A GA simulates evolution on a population of individuals in order to find an optimal solution to the problem at hand. Genetic Algorithms were pioneered by Holland [22], and are discussed in detail in *e.g.* Ref. [23]. GAs have previously been applied in ellipsometry to solve the inversion problem for the thickness and dielectric function of multiple thin layers, see *e.g.* Ref. [24–26].

2. Overdetermined polarimetry

A Stokes polarimeter consists of a polarization state analyzer (PSA) capable of measuring the Stokes vector of a polarization state, see Fig. 1. The PSA is based on performing at least 4 different measurements along different projection states. A measured Stokes vector $\mathbf{S}$ can then be expressed as $\mathbf{S} = \mathbf{A}^{-1}\mathbf{b}$, where $\mathbf{A}$ is a system matrix describing the PSA and $\mathbf{b}$ is a vector containing the intensity measurements. $\mathbf{A}^{-1}$ denotes the matrix inverse of $\mathbf{A}$, which in the case of overdetermined polarimetry with more than 4 projection states will denote the Moore–Penrose *pseudoinverse*. The analyzing matrix $\mathbf{A}$ is constructed from the first rows of the Mueller matrices of the PSA for the different states. The noise in the measurements of $\mathbf{b}$ will be amplified by the condition number of $\mathbf{A}$, $\kappa_{\mathbf{A}}$, in the inversion to find $\mathbf{S}$. Therefore $\kappa_{\mathbf{A}}$ should be as small as possible, which correspond to do as independent measurements as possible (*i.e.* to use projection states that are as orthogonal as possible).

A Mueller matrix $\mathbf{M}$ describes how an interaction changes the polarization state of light, by transforming an incoming Stokes vector $\mathbf{S}_{\text{in}}$ to the outgoing Stokes vector $\mathbf{S}_{\text{out}} = \mathbf{M}\mathbf{S}_{\text{in}}$. To measure the Mueller matrix of a sample it is necessary to generate at least 4 different polarization states by a polarization state generator (PSG) and measure the outgoing Stokes vector by at least 4 measurements for each generated state. The measured intensities can then be arranged in a matrix $\mathbf{B} = \mathbf{A}\mathbf{M}\mathbf{W}$, where the system matrix $\mathbf{W}$ of the PSG contains the generated Stokes vectors as its columns. These generated Stokes vectors are found simply as the first column of the Mueller matrix of the PSG in the respective states. $\mathbf{M}$ can then be found by inversion as $\mathbf{M} = \mathbf{A}^{-1}\mathbf{B}\mathbf{W}^{-1}$. The error $\Delta\mathbf{M}$ in $\mathbf{M}$ is then bounded by the condition numbers according to [27]

$$\frac{\|\Delta\mathbf{M}\|}{\|\mathbf{M}\|} \lesssim \kappa_{\mathbf{W}}\kappa_{\mathbf{A}}\frac{\|\Delta\mathbf{B}\|}{\|\mathbf{B}\|} + \kappa_{\mathbf{A}}\frac{\|\Delta\mathbf{A}\|}{\|\mathbf{A}\|} + \kappa_{\mathbf{W}}\frac{\|\Delta\mathbf{W}\|}{\|\mathbf{W}\|}. \tag{1}$$

The condition number is given as $\kappa_{\mathbf{A}} = \|\mathbf{A}\|\|\mathbf{A}^{-1}\|$, which for the the 2-norm can be calculated from the ratio of the largest to the smallest singular value [28]. $\Delta\mathbf{A}$ and $\Delta\mathbf{W}$ are calibration errors, which increase with κ when calibration methods using matrix inversion are applied. The PSG can be constructed from the same optical elements as the PSA, placed in the reverse order, which would give $\kappa_{\mathbf{A}} = \kappa_{\mathbf{W}} \equiv \kappa$. As the error in Mueller matrix measurements is proportional

#134880 - $15.00 USD Received 9 Sep 2010; revised 5 Oct 2010; accepted 5 Oct 2010; published 18 Oct 2010

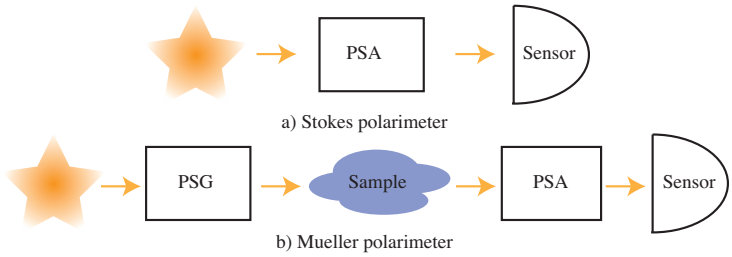

Fig. 1. (a) A Stokes polarimeter measures the polarization state of an arbitrary light source using a Polarization State Analyzer (PSA). (b) A Mueller polarimeter measures how the polarization state of light, generated by with a Polarization State Generator (PSG), is changed by a sample.

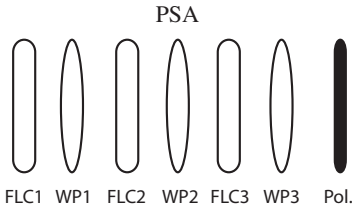

Fig. 2. Sketch of a PSA consisting of 3 FLC's, 3 waveplates (WP), each with a retardance δ and an orientation θ relative to the transmission axis of a polarizer.

to κ^2, it is very important to keep this value as low as possible.

If 4 optimal states can be achieved (giving $\kappa = \sqrt{3}$), no advantage is found by doing a larger number of measurements with different states, compared to repeated measurements with the 4 optimal states [14]. If, however, these optimal states can not be produced ($\kappa > \sqrt{3}$), the condition number, and hence the error, can be reduced by performing more than 4 measurements. For a FLC based polarimeter this can be done by using 3 FLCs followed by a polarizer as PSA, with up to 3 waveplates (WP) between the FLCs to increase the condition number (see Fig. 2). A PSG can be constructed with the same elements in the reverse order. Since each FLC can be switched between two states (this switching can be described as a rotation of the fast axis of a retarder by $+45°$), $2^3 = 8$ different states can be analyzed (generated) by the PSA (PSG). To accurately measure the Stokes vector, the system matrix **A** needs to be well known. For a Mueller polarimeter generating and analyzing 4 states in the PSG and PSA, the eigenvalue calibration method (ECM) [29] can be applied. The ECM allows the measuring of the actual produced states by the PSA and PSG (**A** and **W**), without relying on exact knowledge or modeling of the optical components. However, the ECM is based on the inversion of a product of measured intensity matrices **B** for measurements on a set of calibration samples. This product becomes singular for a system analyzing and generating more than four states. A workaround of this problem is to choose the subset of 4 out of 8 states which gives the lowest κ value, and build a **B** matrix of those states to find 4 of the 8 rows (columns) of **A** (**W**). More rows (columns) of **A** (**W**) can then be found by calibrating on a different subset of the 8 states, giving the second lowest κ value, and so on. By repeating the calibration on different subsets of states, all the 8 rows (columns) of **A** (**W**) can be found with low relative error $\|\Delta\mathbf{A}\|/\|\mathbf{A}\|$ ($\|\Delta\mathbf{W}\|/\|\mathbf{W}\|$).

#134880 - $15.00 USD Received 9 Sep 2010; revised 5 Oct 2010; accepted 5 Oct 2010; published 18 Oct 2010

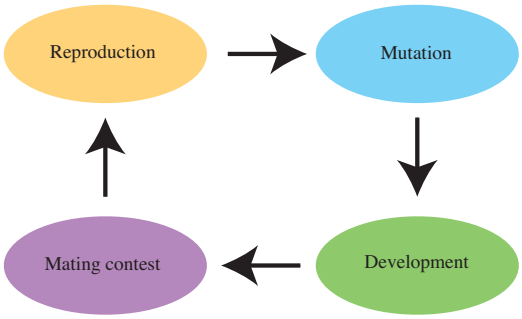

Fig. 3. The four essential processes in a genetic algorithm are shown above. Sexual reproduction is performed by multi-point genetic crossover, giving rise to the next generation of individuals. Mutation can be simulated with simple bit negation (*e.g.* $0 \rightarrow 1$ and *vice versa*). Development is the process where a genotype is interpreted into its phenotype, *i.e.* the binary genome is interpreted as a polarimeter design. In the mating contest, one evaluates the fitness of each individual's phenotype, and let the more fit individuals reproduce with higher probability than the less fit individuals.

3. Genetic optimization

In order to optimize $\kappa(\lambda)$, one can conceivably employ a variety of optimization algorithms, from simple brute-force exhaustive search to more advanced algorithms, such as *e.g.* Levenberg–Marquardt, simulated annealing, and particle swarm optimization. Our group has previously performed optimization of a polarimeter design based on fixed components, namely, two FLCs and two waveplates. In this case, the optimization problem reduces to searching the space of 4 orientation angles. With a resolution of 1° per angle, this gives a search space consisting of $180^4 \approx 10^9$ states to evaluate; on modern computer hardware, this direct search can be performed. In order to optimize the retardances of the components as well, the total number of states increases to about $\left(10^9\right)^2 = 10^{18}$. Obviously, brute force exhaustive search is unfeasible for such large search spaces.

A GA performs optimization by simulating evolution in a population of individuals (here: simulated polarimeters). The three pillars of evolution are variation, heritability, and selection. Our initial population must have some initial genetic variation between the individuals; hence, we initialize our population by generating random individuals. Heritability means that the children have to carry on some of the traits of their parents. We simulate this by either cloning parents into children (asexual reproduction) or by performing genetic crossover (sexual reproduction) in a manner that leave children with some combination of the traits of their parents. Finally, selection is done by giving more fit individuals a larger probability of survival. For this purpose, we used the tournament selection protocol, described in Ref. [23]. For a sketch of the essential processes involved in a GA, see Fig. 3.

Our GA builds directly on the description given by Holland [22], using a binary genome as the genetic representation. In this representation, a string of 0s and 1s represent the genome of the individual. To simulate mutation in our genetic algorithm, we employ logical bit negation; *i.e.* $0 \rightarrow 1$ or vice versa. Sexual reproduction is simulated by using multi-point crossover, *i.e.* simply cutting and pasting two genomes together, as described by Holland [22].

The interpretation of the genome into a phenotype (development), in this case a polarimeter design, is done in a straightforward way. For each variable in the polarimeter's configuration,

#134880 - $15.00 USD Received 9 Sep 2010; revised 5 Oct 2010; accepted 5 Oct 2010; published 18 Oct 2010

i.e. for each orientation angle and each retardance, we select m bits in the genome (typically, $m = 8$) and interpret this number as an integer in the range from 1 to 2^m. The integer is subsequently interpreted as a real number in a predefined range, *e.g.*, $\theta \in [0^\circ, 180^\circ]$. In order to avoid excessively large jumps in the search space due to mutations, we chose to implement the interpretation of bits into integers by using the Gray code, also known as the reflected binary code. The most important parameter values in our GA are shown in Table 2. Making good choices for each of these parameters is often essential in order to ensure good convergence.

After determining the phenotype, we must assign to each simulated polarimeter individual a fitness function (also known as the objective function). In order to do this, we first calculate $\kappa(\lambda)$. As discussed, $\kappa^{-1}(\lambda)$ maximally takes on the value $1/\sqrt{3}$. Hence, we define an error function, e, as

$$e = \frac{1}{N_\lambda} \sum_{n=1}^{N_\lambda} \left(\kappa^{-1}(\lambda_n) - 1/\sqrt{3} \right)^4. \tag{2}$$

In Eq. (2), $\lambda_n = \lambda_{\min} + (n-1)\Delta\lambda$, with $n = 1, 2, \ldots, N_\lambda$ and $\Delta\lambda = 5$ nm. $\lambda_{\min}$ and N_λ are determined by the wavelength range we are interested in. The choice of taking the difference between $\kappa^{-1}(\lambda)$ and the optimal value to power 4 is done in order to "punish" peaks in the condition number more severely. As GAs conventionally seek to maximize the fitness function, we define an individual's fitness as

$$f = \frac{1}{e}. \tag{3}$$

This definition is convenient because f takes on real and positive values where higher values represents more optimal polarimeter designs.

4. Results

For the case of a polarimeter based on 3 FLCs and 3 WPs, we have minimized $\kappa(\lambda)$ by varying the orientation angle, θ, and the retardance, δ, of all the elements. This yields a 12-dimensional search space, *i.e.*, 6 retardances and 6 orientation angles. θ is the angle between the fast axis of the retarder (WP or FLC) and the transmission axis of the polarizer (see Fig. 2), taken to be in the range $\theta \in [0^\circ, 180^\circ]$. The retardance, δ, is modeled using a modified Sellmeier equation,

$$\delta \approx 2\pi L \left[\frac{A_{UV}}{(\lambda^2 - \lambda_{UV}^2)^{1/2}} - \frac{A_{IR}}{(\lambda_{IR}^2 - \lambda^2)^{1/2}} \right], \tag{4}$$

where A_{UV}, A_{IR}, λ_{UV}, and λ_{IR} are experimentally determined parameters for an FLC ($\lambda/2$@510 nm, Displaytech Inc.) and a Quartz zero order waveplate ($\lambda/4$@465 nm) taken directly from Refs. [19] (for the FLCs, $A_{IR} = 0$). L is a normalized thickness, with $L = 1$ corresponding to a retardance of $\lambda/2$@510 nm for the FLCs and $\lambda/4$@465 nm for the waveplates. Each L and θ are represented by 8 bits each in the genome. We use experimental values to ensure that our design is based on as realistic components as possible.

The 3-FLC polarimeter design scoring the highest fitness function is shown in Table 1. The wavelength range for which we optimized the polarimeter was from 430 to 2000 nm. To visualize the performance of this design, we show a plot of $\kappa^{-1}(\lambda)$ in Fig. 4. The inverse condition number, κ^{-1}, is larger than 0.5 over most parts of the spectrum, which is close to the optimal inverse condition number ($\kappa^{-1} = 1/\sqrt{3} = 0.577$). This is a great improvement compared to the earlier reported 3-FLC design [21], which oscillates around $\kappa^{-1} \approx 0.33$. The new design promise a decrease in noise amplification by up to a factor of 2.1 for a Stokes polarimeter, and up to factor of 4.5 for a Mueller polarimeter. In addition the upper spectral limit is extended

#134880 - $15.00 USD Received 9 Sep 2010; revised 5 Oct 2010; accepted 5 Oct 2010; published 18 Oct 2010

Table 1. Orientation angles, θ, and normalized thicknesses L, of the components of the best 3-FLC polarimeter. (WP = (fixed) waveplate)

Component	θ[°]	L
FLC1	56.5	2.44
WP1	172.9	1.10
FLC2	143.3	1.20
WP2	127.1	1.66
FLC3	169.4	1.42
WP3	110.1	4.40

from 1700 nm to 2000 nm. Shorter wavelengths than 430 nm were not considered as the FLC material will be degraded by exposure to UV light. Previous designs often suffer from $\kappa^{-1}(\lambda)$ oscillating as a function of wavelength, whereas our solution is more uniform over the wavelength range we are interested in. This uniformity in $\kappa(\lambda)$ will, according to Eq. (1), give a more uniform noise distribution over the spectrum.

To give some idea of how fast the GA converges, a plot of f [see Eq. (3)] as a function of the generation number is shown in Fig. 5. The mean population fitness (μ) and standard deviation (σ) is also shown. As so often happens with genetic algorithms, we see that the maximal and average fitness increases dramatically in the first few generations. Following this fast initial progress, evolution slows down considerably, before it finally converges after 600 generations. The parameters used in our GA to obtain these results are shown in Table 2.

A design using fewer components, in particular 2 FLCs and 2 waveplates, does have advantages. These advantages include increased transmission of light, as well as reduced cost and complexity with respect to building and maintaining the instrument. In addition some applications have weight and volume restrictions [3]. For these reasons, we have performed genetic optimization of the 2-FLC design. In Fig. 6, we show the performance of two polarimeter designs for the wavelength ranges $430-1100$ nm (compatible with an Si detector) and $800-1700$ nm. Both of these polarimeter designs show condition numbers which are considerably better

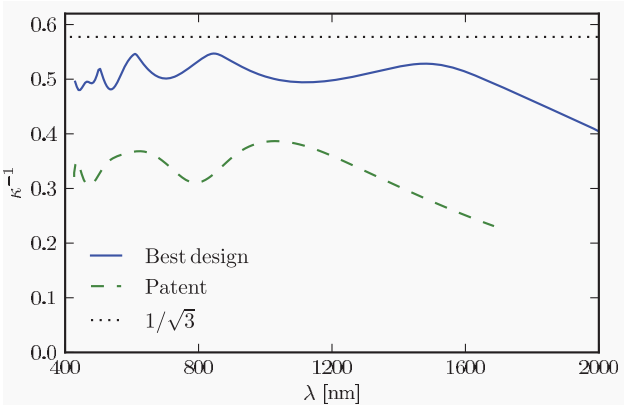

Fig. 4. Inverse condition number for the best GA-generated 3-FLC design. For comparison, we show the inverse condition number of the patented 3-FLC design [21].

#134880 - $15.00 USD Received 9 Sep 2010; revised 5 Oct 2010; accepted 5 Oct 2010; published 18 Oct 2010

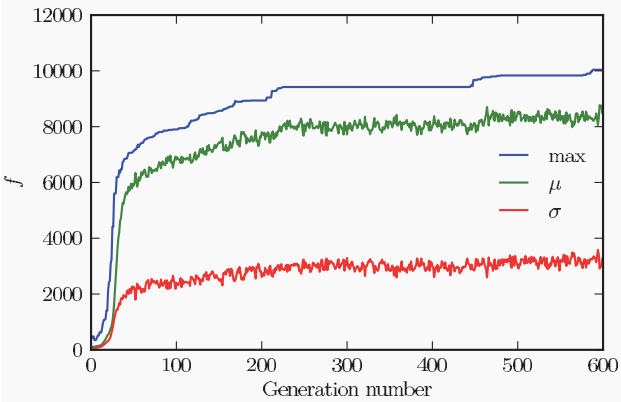

Fig. 5. Convergence of fitness as a function of generation number. μ and σ refer to the average and standard deviation of the population's fitness, respectively. The best result from this simulation is the one shown in Fig. 4.

Table 2. Genetic Algorithm parameters. The "crossover rate" is the probability for two parents to undergo sexual reproduction (the alternative being asexual reproduction). The parameter "crossover points" refer to the number of points where we cut the genome during crossover (sexual reproduction). "Mutation rate" is the probability for any given individual to undergo one or several bit flip mutations in one generation

Parameter	Value
Crossover rate	0.7
Crossover points	2
Mutation rate	0.2
Population size	500

Table 3. Orientation angle, θ, and normalized thickness, L, of the 2-FLC polarimeters shown in Fig. 6

	Visible design		NIR design	
Component	θ[°]	L	θ[°]	L
FLC 1	90.4	1.17	177.9	2.60
WP 1	3.5	3.58	112.9	2.94
FLC 2	92.5	1.02	74.8	1.75
WP 2	19.8	3.52	163.1	4.71

than previously reported designs. The numerical parameters of the two designs based on 2 FLCs are shown in Table 3.

Our optimization algorithm can, with little effort, be applied to a wider range of polarimeter design. Any optical component can be included into our GA; for example, one can include fixed waveplates of different materials, prisms, mirrors, and other types of liquid crystal devices. The material of each component could also be a variable, which could help alleviate the dispersion problem. The only requirement is that the retardance of the component in question must be

#134880 - $15.00 USD Received 9 Sep 2010; revised 5 Oct 2010; accepted 5 Oct 2010; published 18 Oct 2010

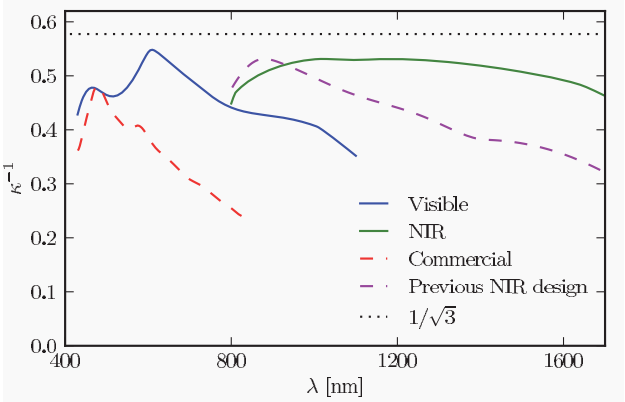

Fig. 6. Condition number for two designs using 2 FLC retarders and 2 waveplates. By optimizing $\kappa(\lambda)$ over a narrower part of the spectrum, we can design good polarimeters with fewer components. The polarimeter designs labeled "Visible" and "IR" show our two designs, optimized for 430 nm $< \lambda <$ 1100 nm and 800 nm $< \lambda <$ 1700 nm, respectively. For comparison with our "NIR" design, we show the previous simulated design from Ref. [30]. The curve labeled "Commercial" shows the measured condition number of a commercial instrument (MM16, Horiba, 2006) based on the same (FLC) technology.

possible to either model theoretically or measure experimentally. It is possible to optimize a polarimeter for a different wavelength range, simply by changing program inputs. Focusing on a wavelength range which is as narrow as possible typically results in higher condition numbers than reported here. Evaluating different technologies, materials and components for polarimetry should thus be relatively straightforward. The task is not computationally formidable: we have used ordinary desktop computers in all our calculations.

5. Conclusion

In conclusion, we have used genetic algorithms to optimize the design of a fast multichannel spectroscopic Stokes/Mueller polarimeter, using fast switching ferroelectric liquid crystals. We have presented three polarimeter designs which promise significant improvement with respect to previous work in terms of noise reduction and spectral range. Our approach requires relatively little computational effort. One can easily generate new designs if one should wish to use other components and materials, or if one wishes to focus on a different part of the optical spectrum. We hope that our designs will make polarimetry in general, and ellipsometry in particular, a less noisy and more efficient measurement technique.

Acknowledgements

The authors would like to thank professor Keith Downing at the Department of Computer and Information Science at NTNU for helpful discussions regarding genetic algorithms and their implementation.

#134880 - $15.00 USD Received 9 Sep 2010; revised 5 Oct 2010; accepted 5 Oct 2010; published 18 Oct 2010